Inês Maria Trindade Crespo

Licenciatura em Ciências da Engenharia Mecânica

Damage Propagation in Composite Materials Meso-Mechanical Models

Dissertação para obtenção do Grau de Mestre em
Engenharia Mecânica

Orientador: Professor Doutor João Mário Burguete Botelho Cardoso, Professor Auxiliar da Faculdade de Ciências e Tecnologia da Universidade Nova de Lisboa

Co-orientador: Doutor Pedro Miguel de Almeida Talaia, Engenheiro de I&D, CEiiA

Júri:

Presidente: Prof. Doutor Pedro Samuel Gonçalves Coelho
Arguente: Prof. Doutora Marta Isabel Pimenta Verdete da Silva Carvalho
Vogais: Prof. Doutor João Mário Burguete Botelho Cardoso
Doutor Bernardo Rodrigues de Sousa Ribeiro

FACULDADE DE
CIÊNCIAS E TECNOLOGIA
UNIVERSIDADE NOVA DE LISBOA

Setembro 2015

Damage Propagation in Composite Materials
Meso-Mechanical Models

“Copyright” Inês Maria Trindade Crespo, FCT/UNL e UNL

A Faculdade de Ciências e Tecnologias da Universidade Nova de Lisboa e a Universidade Nova de Lisboa têm o direito, perpéctuo e sem limites geográficos, de arquivar e publicar esta dissertação atrevés de exemplares impressos reproduzidos em papel ou de forma digital, ou por qualquer outro meio conhecido ou que venha a ser inventado, e de a divulgar através de repositórios ciêntificos e de admitir a sua cópia e distribuição com objectivos educacionais e de investigação, não comerciais, desde que seja dado crédito ao outor e editor.

Ao meu pai e à minha mãe

Acknowledgment

To Dr. João Burguete Cardoso, the supervisor of this dissertation, for all the availability that he always had to receive me, for all he taught me, for his patient and for making available all resources needed for this dissertation. Even in the most difficult time he never stopped encouraging and helping me.

To all FCT-UNL Professors from the Mechanical and Industrial Engineering department, which contributed to the success of my academic career. They were the most important part of my graduation and I am very grateful to them.

To CEiiA and his collaborators, that received me and integrated me in their work ambient. They helped me whenever I needed, and advised me well.

To my Family, that always believe in my capacities. Especially my mother, who has always been by my side and always did her best to ever missed me anything.

To my friends, who accompanied me in my academic life and, whenever they could, tried to make me forget this dissertation by instants.

Abstract

Composite materials have a complex behavior, which is difficult to predict under different types of loads.

In the course of this dissertation a methodology was developed to predict failure and damage propagation of composite material specimens. This methodology uses finite element numerical models created with Ansys and Matlab softwares.

The methodology is able to perform an incremental-iterative analysis, which increases, gradually, the load applied to the specimen. Several structural failure phenomena are considered, such as fiber and/or matrix failure, delamination or shear plasticity. Failure criteria based on element stresses were implemented and a procedure to reduce the stiffness of the failed elements was prepared.

The material used in this dissertation consist of a spread tow carbon fabric with a 0°/90° arrangement and the main numerical model analyzed is a 26-plies specimen under compression loads. Numerical results were compared with the results of specimens tested experimentally, whose mechanical properties are unknown, knowing only the geometry of the specimen.

The material properties of the numerical model were adjusted in the course of this dissertation, in order to find the lowest difference between the numerical and experimental results with an error lower than 5% (it was performed the numerical model identification based on the experimental results).

Keywords: meso-mechanical scale, delamination, cohesive elements, contacts, damage propagation, failure criteria.

Resumo

Os materiais compósitos têm um comportamento bastante complexo, que é difícil de prever sob diferentes tipos de cargas.

No decorrer desta dissertação foi desenvolvida uma metodologia capaz de simular a ocorrência de falhas e a propagação de dano em provetes construídos com materiais compósitos. Esta metodologia utiliza modelos numéricos de elementos finitos, à escala meso-mecânica, criados através dos programas Ansys e Matlab.

A metodologia inclui a realização de uma análise incremental-iterativa, que aumenta, gradualmente, a carga aplicada no provete. Vários mecanismos de colapso foram incluidos, como a ocorrência de falha das fibras e/ou da matriz, delaminação ou plasticidade devida ao corte. Foram implementados critérios de falha baseados nas tensões dos elementos atraves de um procedimento para reduzir a rigidez dos elementos onde a falha ocorre.

O material usado neste trabalho consiste num tecido ultrafino de carbono com fibras orientadas a 0° e 90° e o modelo numérico analisado foi um provete de 26 camadas de tecido submetido à compressão. Os resultados numéricos foram comparados com os resultados dos provetes ensaiados experimentalmente, cujas propriedades mecânicas são desconhecidas, conhecendo-se apenas a geometria do provete.

As propriedades do material do modelo foram ajustadas no decorrer da dissertação, por forma a encontrar a menor diferença possível entre os resultados numéricos e experimentais com um erro inferior a 5% (foi realizada a identificação do modelo numérico face aos resultados experimentais).

Palavras-Chave: escala meso-mecânica, delaminação, elementos coesivos, contactos, propagação do dano, critério de falha.

Table of Contents

Acknowledgment .... **v**

Abstract .... **vii**

Resumo .... **ix**

Table of Contents .... **xi**

List of Figures .... **xiii**

List of Tables .... **xvii**

List of Symbols .... **xix**

1. Introduction **1**

- 1.1. Motivation 2
- 1.2. Objectives 2

2. Theoretical framework **5**

- 2.1. Composite Materials 5
  - 2.1.1. Matrix 6
  - 2.1.2. Fiber (reinforcement) 6
  - 2.1.3. Textile composites 7
  - 2.1.4. Spread Tow Carbon Fabric 8
- 2.2. Damage in composite material 9
  - 2.2.1. Fracture mechanism 10
  - 2.2.2. Laminated damage mode 12
    - 2.2.2.1. Longitudinal tensile fracture 14
    - 2.2.2.2. Longitudinal Compressive fracture 14
    - 2.2.2.3. Transverse fracture (with $\alpha = 0$) 16
    - 2.2.2.4. Transverse fracture (with $\alpha \neq 0$) 16
  - 2.2.3. Failure criteria for plies 16
    - 2.2.3.1. Maximum stress 16
    - 2.2.3.2. Maximum strain 17
    - 2.2.3.3. Tsai-Wu 17
    - 2.2.3.4. Tsai-Hill 19

2.2.3.5. Hashin-Rotem 19
2.2.3.6. Puck 20
2.2.3.7. LaRC03/04 21
2.3. Characterization of multi-scale models 27
2.3.1. Micro-scale models 29
2.3.1. Meso-scale models 29
2.3.1.1. Introduction to damage description in the meso-scale 30
2.3.2. Macro-scale models 32

3. Ply numerical model 33
3.1. Spread Tow Carbon fabric ply: initial model description 33
3.2. Mesh Convergence 34
3.3. Details of this first model 39
3.3.1. Shear and transverse compression plasticity 39
3.3.2. Delamination 41
3.4. Combined failure criterion 47
3.5. Incremental-iterative analysis 48
3.6. Results 51

4. Numerical model of a specimen 57
4.1. Boundary conditions 58
4.2. Incremental iterative analysis 63
4.3. Results 67
4.3.1. Parameters adjustment 71
4.3.1.1. Results 72
4.4. Experimental results 76
4.4.1. Shear Plasticity 79
4.5. Comparison of Results 80

5. Conclusion 83
5.1. Complied objectives 85
5.2. Future Works 85

References 87

List of Figures

Figure 2.1 - Composite materials classification [5] 6

Figure 2.2 - Different reinforcement types [7] 7

Figure 2.3 - Different weave patterns of textile fabrics [9] 8

Figure 2.4 - An example of spread-tow carbon fabric [12] 8

Figure 2.5 - “Schematic of tow-spreading process with the help of air flow” [11] 9

Figure 2.6 - Representative cross-section of: a) plain weave with spread tows; b) plane weave with regular tows 9

Figure 2.7 - Failure propagation modes[17] 11

Figure 2.8 - "Fracture surfaces and corresponding internal variables" [18] 12

Figure 2.9 - "Fracture surfaces and corresponding internal variables"[17] 13

Figure 2.10 - In-plane failure modes 14

Figure 2.11 - "(a) Fiber micro buckling between an elastic matrix in shear mode (up) and in tension mode (down); (b) kink band geometry; (c) real kink band" [18] 15

Figure 2.12 - Inter/fiber fracture modes [25] 20

Figure 2.13 - “Multi-scale damage and failure in fiber reinforced composites” [33] 28

Figure 2.14 - Different geometries for: (a) micro-scale, (b) meso-scale and (c) macro-scale [35] 29

Figure 2.15 - “Hypothesis of A) strain equivalence, B) stress equivalence and C) energy equivalence between the damage physical space and undamaged effective space”[18],[17] 31

Figure 3.1 - Simplified geometry of the - spread tow carbon fabric ply 33

Figure 3.2 - Representative elements (a) - Brick 8 nodes and (b) Brick 20 nodes [40] 35

Figure 3.3 - Simplified geometry for the mesh convergence 36

Figure 3.4 - Tension-number of elements for point A 37

Figure 3.5 - Tension-number of elements for point B 37

Figure 3.6 - Tension-number of elements for point C1 38

Figure 3.7 - Tension-number of elements for point C2 38

Figure 3.8 - Computational cost-number of elements 39

Figure 3.9 - Quasi-static and dynamic axial stress-strain responses from off-axis and transverse compression tests (for IM/8552 laminates) [21] 41

Figure 3.10 - “Schematic of interface elements” [45] 42

Figure 3.11 - “Normal contact stress and contact gap curve for bilinear cohesive zone material” [45],[18] 43
Figure 3.12 - Boundary conditions used to test the cohesive elements implemented without contacts........ 44
Figure 3.13 - Final results of the delamination test (with cohesive elements without contacts). 44
Figure 3.14 - Results of the delamination test with contact and cohesive elements for substep: (a) 6, (b) 22 and (c) 25........ 46
Figure 3.15 - Comparison between Tsai-Wu a maximum stress failure criteria........ 48
Figure 3.16 - Incremental-iterative analysis for one ply under tensile loads (units of the initial parameters in m)........ 50
Figure 3.17 - Boundary conditions applied to the ply model........ 52
Figure 3.18 - Equivalent Von-Mises Stress Analysis at step 1 52
Figure 3.19 - Equivalent Von-Mises Stress Analysis at step 2 53
Figure 3.20 - Equivalent Von-Mises Stress Analysis at step 3 53
Figure 3.21 - Equivalent Von-Mises Stress Analysis at step 14 53
Figure 3.22 - Equivalent Von-Mises Stress Analysis at step 15 54
Figure 3.23 - Stress-Strain results of the simulation of the ply model under tension loads........ 54
Figure 3.24 - Spread tow carbon fabric specimen after a tension test........ 55
Figure 4.1 - Geometry of the compressive specimen........ 58
Figure 4.2 - Results of the first compression test........ 59
Figure 4.3 - Results of the compression test with the cohesive properties changed and the boundary conditions (1) 60
Figure 4.4 - Results of the compression test with the cohesive properties changed and the boundary conditions (2) 61
Figure 4.5 - Results of the compression test with the cohesive properties changed and the boundary conditions (3) 62
Figure 4.6 - Numerical model and real specimen 63
Figure 4.7 - Incremental-iterative analysis for 26-plies compression specimen........ 64
Figure 4.8 - Equivalent Von-Mises Stress Analysis of a 26-plies compression specimen at step 4 67
Figure 4.9 - Equivalent Von-Mises Stress Analysis of a 26-plies compression specimen at step 16........ 68
Figure 4.10 - Equivalent Von-Mises Stress Analysis of a 26-plies compression specimen at step 17........ 68
Figure 4.11 - Equivalent Von-Mises Stress Analysis of a 26-plies compression specimen at step 18........ 68

Figure 4.12 - Equivalent Von-Mises Stress Analysis of a 26-plies compression specimen at step 19 ... 69
Figure 4.13 - Equivalent Von-Mises Stress Analysis of a 26-plies compression specimen at step 20 ... 69
Figure 4.14 - Equivalent Von-Mises Stress Analysis of a 26-plies compression specimen at step 21 ... 69
Figure 4.15 - Stress-Strain results of the simulation of a 26-plies compression specimen ... 70
Figure 4.16 - Equivalent Von-Mises Stress Analysis of a 26-plies compression specimen at step 5 (with adjusted parameters) ... 72
Figure 4.17 - Equivalent Von-Mises Stress Analysis of a 26-plies compression specimen at step 19 (with adjusted parameters) ... 72
Figure 4.18 - Equivalent Von-Mises Stress Analysis of a 26-plies compression specimen at step 20 (with adjusted parameters) ... 73
Figure 4.19 - Equivalent Von-Mises Stress Analysis of a 26-plies compression specimen at step 21 (with adjusted parameters) ... 73
Figure 4.20 - Equivalent Von-Mises Stress Analysis of a 26-plies compression specimen at step 22 (with adjusted parameters) ... 73
Figure 4.21 - Equivalent Von-Mises Stress Analysis of a 26-plies compression specimen at step 23 (with adjusted parameters) ... 74
Figure 4.22 - Equivalent Von-Mises Stress Analysis of a 26-plies compression specimen at step 24 (with adjusted parameters) ... 74
Figure 4.23 - Stress-Strain results of the simulation of a 26-plies compression specimen (with adjusted parameters) ... 75
Figure 4.24 - Schematic test set up of the experimental compression tests ... 77
Figure 4.25 - (a) Schematic position of the virtual extensometers; (b) Digital image correlation: strain measurements [52] ... 77
Figure 4.26 - Stress-strain curves of 4 different specimens with 26 plies and a 0º/90º arrangement, tested in compression ... 78
Figure 4.27 - Stress-strain curves resulting from the compression test of the specimens with (a) a 0º/90º arrangement, (b) 15º/-75º arrangement, (c) 30º/-60º arrangement and (d) 45º/-45º arrangement ... 79
Figure 4.28 - Comparison between the stress-strain results of the experimental specimens (in black) and the numerical specimen with the adjusted parameters (in red) ... 81
Figure 4.29 - Final appearance of the numerical model and an experimental specimen with a 0/90 arrangement ... 81

List of Tables

Table 3.1 - Spread tow carbon fabric ply dimensions 34
Table 3.2 - Elastic properties of IM7/8552 unidirectional laminates 34
Table 3.3 - Location of the evaluated points 36
Table 3.4 - Yield stresses of Hex-ply IM7/8552 unidirectional laminates 40
Table 3.5 - Cohesive material properties for IM7-8552 [38], [47] 43
Table 3.6 - Cohesive material properties, with critical energies density, for IM7-8552 [38], [48], [49]. 45
Table 3.7 - Unidirectional constants of the uniaxial tests used in the simulation of one ply under tension loads[17] 51
Table 4.1 - Dimensions of the compressive specimen 58
Table 4.2 - Elastic properties of IM7/8552 unidirectional laminates, for compression loads [38]. 59
Table 4.3 - Interlaminar cohesive properties changed 59
Table 4.4 - Boundary conditions (1) applied to the numerical model 60
Table 4.5 - Boundary conditions (2) applied to the numerical model 61
Table 4.6 - Boundary conditions 3) applied to the numerical model 62
Table 4.7 - Initial parameters of the 0º/90º spread tow carbon fabric compressive specimen 66
Table 4.8 - Unidirectional constants of the uniaxial tests used in the simulation of 26-plies specimen under compression loads. 66
Table 4.9 - Composite material mechanical properties used 67
Table 4.10 - Unidirectional constants of the uniaxial tests used in the simulation of 26-plies specimen under compression loads updated (XC and YC) 71
Table 4.11 - Composite material mechanical properties adjusted ($E11\ and\ E22 = E33$) 72

List of Symbols

σ	Stress
ε	Strain
E	Young modulus
v_{ij}	Poisson coefficient
G_{ij}	Shear modulus of elasticity for plane ij
G_I	Energy release rate for mode I
G_{II}	Energy release rate for mode II
G_{III}	Energy release rate for mode III
γ	Classical surface energy
U	Total potential
A	Area
K_I	Stress intensity factor
G_{IC}	Critical energy for mode I
G_{IIC}	Critical energy for mode II
G_{IIIC}	Critical energy for mode III
X_T	Failure stress under longitudinal tension
X_C	Failure stress under longitudinal compression
Y_T	Failure stress under transversal tension
Y_C	Failure stress under transversal compression
S_L	Failure stress under pure shear
α	Angle of the fracture plane, fracture angle
ε_{iT}	Maximum allowable strain in i direction under tension loads
ε_{iC}	Maximum allowable strain in i direction under compression loads
τ_{ij}	Shear strength in ij plane

f_i	Parameters used in Tsai-Wu failure criteria
F_{ij}	Parameters used in Tsai-Wu failure criteria
FI	Failure index
S_T	Transverse shear strength
$S_{L_{is}}$	In-situ longitudinal shear strength
τ_{eff}^{T}	Effective transverse shear
τ_{eff}^{L}	Effective longitudinal shear
η^L	Coefficients of influence in the longitudinal direction
η^T	Coefficients of influence in the transversal direction
$Y_{T_{is}}$	In-situ failure stress under transversal tension
Λ_{jj}^{0}	Parameters used in the LaRC03 failure criteria
φ	Fiber misalignment angle
γ_{12}^{u}	Engineering shear strain at failure
ψ	Kink plane angle
C_{mnst}^{0}	Undamaged stiffness tensor
$I_{ijklmnst}$	Identity matrix
$D_{ijklmnst}$	Tensor formed by scalar damage variables
$\tilde{\sigma}$	Effective stress
$\tilde{\varepsilon}$	Effective strain
Ψ	Free energy density
δ_n^c	Normal displacement jump at the completion of deboning;
δ_t^c	Tangential displacement jump at the completion of deboning;
L	Length
W	Width
t	Thickness
NFE	Number of failed elements
$\Delta_{x_{Max}}$	Maximum displacement applied
Δ_x	Increment value
D	Initial displacement in each iteration
a_{Max}	Maximum number of analysis
E_S	Element size

$ESTIF$	Constant value used to deactivate the elements

Chapter 1.

Introduction

Composite materials present great advantages over many metallic materials, causing them to be increasingly used in the aeronautical industry. The use of these materials has grown considerably in this industry, mostly, because of two important characteristics, which are low weight and high strength. However, to be able to take advantage of these characteristics it is necessary that the behavior of composite materials is well known so they can be used correctly.

The main goal of this dissertation is to study and predict the behavior of composite materials specimens (failure initiation and damage propagation) under certain loads, by developing an interface program methodology between MatLab and Ansys softwares (to perform the incremental-iterative analysis, which increase the applied loads on the numerical model at the same time as the stress results are evaluated). With this program, the numerical model of a ply model is first analyzed and subsequently, a 26-plies specimen under compression loads is studied.

The ply model is considered in Chapter 3 and its main purpose is to test de main features implemented in the program. In this chapter, a mesh convergence study is performed in order to evaluate the right element type and size to be used in subsequent numerical models. Also, cohesive and contact elements are implemented. Cohesive elements are used to simulate the delamination observed in the specimens tested experimentally and contacts are defined between different plies to avoid interpenetration (volume interference). Finally, it is proposed a combined failure criterion combining Maximum Stress and Tsai-Wu failure criteria and it is performed an incremental-iterative analysis of the ply, to find out the areas with higher stress concentrations.

In Chapter 4 the numerical model of 26-plies specimen is implemented and used to simulate the real compressive specimens tested experimentally. Here the main objectives are to properly define the boundary conditions that provide a final behavior representing as close as possible the final behavior of the experimental specimens, run the incremental-iterative analysis to evaluate the results and identify the parameters of numerical model in order to obtain better results. After the first simulation of a compression specimen, the mechanical properties of the material used in the numerical models are adjusted in order to reduce the difference between the numerical and experimental results. Finally, a comparison between numerical and experimental results is made.

The goal of this work consists in finding the material properties that provide similar results (with an error less than 5%) between experimental and numerical results, in order to validate the models presented here.

1.1. Motivation

The subject of this dissertation arises after performing experimental tests in composite materials specimens subjected to tension and compression loads.

Before the experimental work, the behavior of the material was completely unknown and so there were no expectations regarding these results. After the experimental work, some doubts emerged concerning failure initiation and damage propagation. In order to study comprehensively the collapse behavior, it was proposed to implement a numerical model able to simulate these events that were observed in the specimens experimentally tested and obtain similar results.

This numerical models must be able to predict the failure initiation and the damage propagation, which are difficult to observe during the experimental tests, since everything happens fast.

Usually the knowledge of the composite materials behavior is acquired by the use of expensive and long-lasting experimental tests. The numerical simulation is capable to acquire the majority of this knowledge about the behavior of the composite material in a more economically way. Besides being less expensive than the experimental tests, virtual simulations have the ability to provide a better understanding of physical processes involved in the material behavior, since they provide much more information about the state of the system than the experimental test. Once the models are validated, the behavior of the material can be simulated, in the case of loads or boundary conditions change. Other advantages include the possibility to perform design optimization from the detailed knowledge of the material behavior.

Meso-scale models are so important, once they provide a set of effective material parameters needed in macro-scale models implementation.

1.2. Objectives

The main objectives planned for this dissertation are presented bellow and each of them should be fulfilled in an objective and clearly way.

In Chapter 5, is indicated, exactly, the pages where these objectives/goals were complied.

- Implement cohesive and contact elements, in order to simulate delamination accurately;
- Develop a methodology able to model the specimens tested and simulate the experimental tests;
- Perform at least one analysis of a 26-plies compression specimen and provide the stress-strain curve results of this analysis;
- Validate numerical models, with an error less than 5% between numerical and experimental results;

Chapter 2.

Theoretical framework

2.1.Composite Materials

According to Music and Witdroth [1], composite materials can be defined as a combination of, at least, two different materials with complementary properties. Each one of them has a function, one acts as a matrix, which maintains the material cohesive, while the second acts like a reinforcement, which provides resistance to the composite material.

Unlike some metal alloys, where different materials can be combined at the microscale and the components cannot be distinguished by the naked eye (it is an homogeneous material), the constituents of the composite materials remain separate and are easily distinguishable by the naked eye and this fact makes the composite materials heterogeneous materials [2].

The function of the matrix [3] is to hold the reinforcement in an orderly pattern and transfer the loads between the fibers that constitute the reinforcement, while the reinforcement gives the composite materials its desired properties

However, the global properties of these materials depends, not only, on the material properties of the components (matrix and reinforcement), but also, on the interface between them and the methods used in its production [1], [3]. It is expected that the composite material that results from a combination of two constituents has a balance of structural properties that is superior to either constituent material alone [4].

The main advantage of the composite materials is that, if well designed, they usually present the best qualities of their constituents and often some qualities that neither the constituents materials have [2]. Some of the properties that can be improved by producing a composite material are strength, stiffness, corrosion resistance, wear resistance, weight, fatigue life, temperature-dependent behavior, thermal insulation, thermal conductivity or acoustical isolation [2].

Figure 2.1 represents, schematically, the different types of composite materials that can be made.

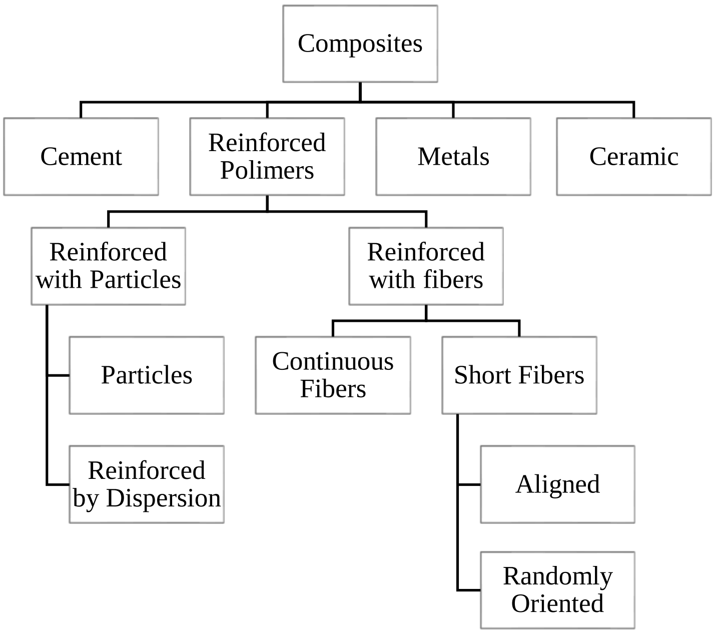
Composites
Cement
Reinforced Polimers
Metals
Ceramic
Reinforced with Particles
Reinforced with fibers
Particles
Reinforced by Dispersion
Continuous Fibers
Short Fibers
Aligned
Randomly Oriented

Figure 2.1 - Composite materials classification [5]

2.1.1. Matrix

The matrix of a composite material must ensure the connection of the reinforcements due to its cohesive and adhesive characteristics. When fibers are used as reinforcement, it protects them from the environment, from damage during manufacturing and operation and transfer the loads to and between the fibers [4].

Typically, the reinforcements are stronger and stiffer than the matrix. As a continuous phase, the matrix controls the transverse properties, interlaminar strength and elevated-temperature strength of the composite material. However it allows the strength of the fibers to be used in their full potential by providing effective load transfer from external loads to the fibers [4]. Additionally, the matrix provide an inelastic response in order to reduce de stress concentrations. So, the internal stresses are redistribute from the broken fibers [4].

The constituent material of the matrix, can be polymer, metal or ceramic, but the most widely used for aeronautical industry is polymer. Within the polymeric materials, the most common are epoxy resin and polyester. In this dissertation, the matrix that constitutes the composite material is an epoxy resin.

2.1.2. Fiber (reinforcement)

The main function of a reinforcement is to provide superior levels of strength and stiffness to the composite materials [4].

Composite materials can contain the fibers in three different ways: particulate, continuous and discontinuous fibers, which are presented in the Figure 2.2. In the composite material with continuous fibers, the fibers provide all the strength and stiffness to the composite.

Music and Widroth [1] explain that, when using short fibers and particulates, the matrix must transfer the loads between the reinforcement more frequently, which results in a composite with low properties when compared to the composites with continuous fibers.

Graphite and carbon fibers are the most generally used advanced fibers, and graphite/epoxy or carbon/epoxy composite materials are now used commonly in aerospace structures [6]. It should be noted that the reinforcement of the composite material studied in this dissertation is composed by carbon fibers.

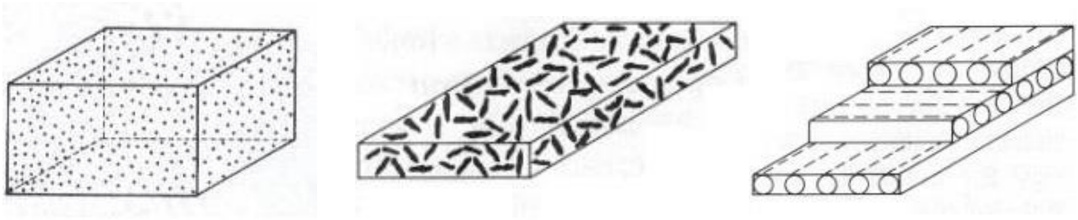

Particles

Short fibers

Continuous fibers

Figure 2.2 - Different reinforcement types [7]

2.1.3. Textile composites

Textile composites are widely used in advanced structures in aeronautical, automotive and marine industries. It happens because they have good mechanical properties and attractive reinforcing materials with low fabrication cost and easy handling [8].

Since the material properties are anisotropic and inhomogeneous in nature, the parameters controlling the mechanical properties are numerous, such as fiber architecture, fiber properties or matrix properties [8].

Typically, textile composites are divided in three categories: woven fabrics, knitted fabrics and braided fabric [1]. However, the focus of interest in this dissertation will be the woven fabrics, once these are the most used textile composites in aeronautical industry [1], [8].

Within the textile composites, it can be found the in-plain weaves (2D), where each warp yarn passes alternately over and under each weft yarn, making the fabric produced symmetric [1].

The Figure 2.3 shows some examples of 2D woven patterns.

Some parameters, such as the weave architecture, yarn's dimension and spacing or yarn’s fiber volume fraction can affect the mechanical properties of the material.

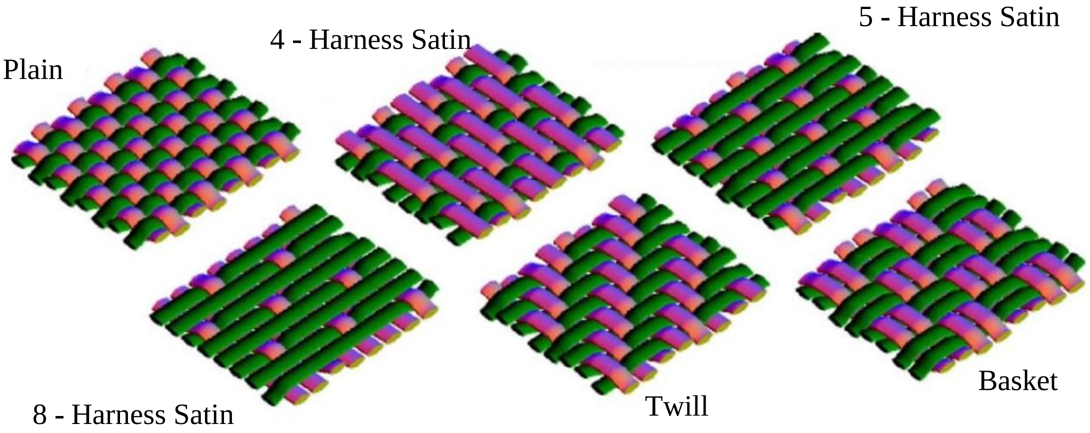

Figure 2.3 - Different weave patterns of textile fabrics [9]

2.1.4. Spread Tow Carbon Fabric

The material used in this dissertation is a spread tow carbon fabric, presented in the Figure 2.4.

This material presents many differences from the conventional carbon fabrics, with regular tows. To produce this material a conventional carbon fiber tow is thinned by increasing the width of the tow from 5 mm to approximately 25 mm, thus, reducing the weight per unit area by approximately 500% [10].

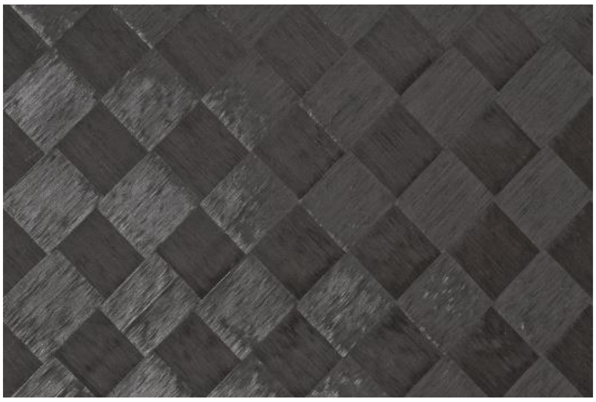

Figure 2.4 - An example of spread-tow carbon fabric [12]

The tow-spreading technology was developed by Industrial Technology Center in Fukui Prefecture. The operating mode of the tow-spreading technology consists of passing a tow though a spreading machine that is equipped with an air duct and a vacuum that sucks the air downward through the air duct, this process is shown diagrammatically in the Figure 2.5 [11]. By the use of this technology it can be produced unidirectional plies or woven fabric plies [10].

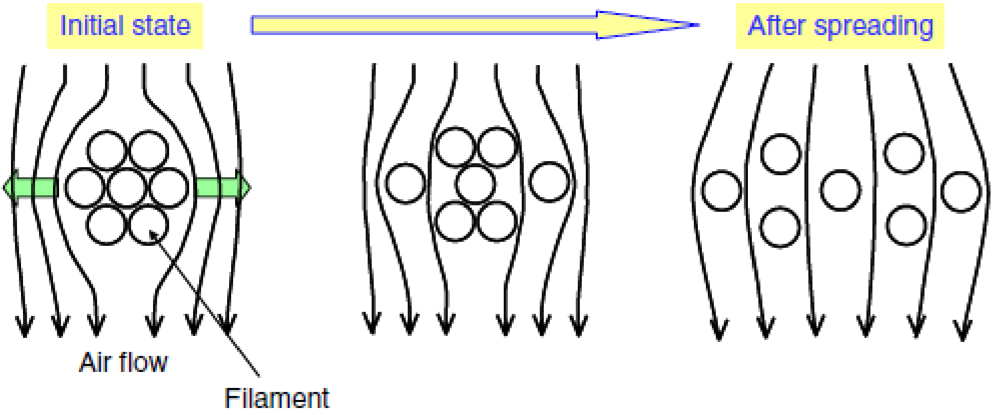

Figure 2.5 - "Schematic of tow-spreading process with the help of air flow" [11]

The use of spread-tows results in a very thin plies with optimal in-plane and out-of-plane properties. As Hassan et. al. [10] referred, the ply thickness has a great importance in controlling composite material mechanical properties: "the thinner the ply the better the properties" [10].

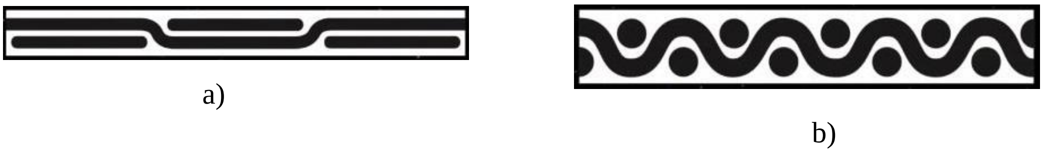

Figure 2.6 - Representative cross-section of: a) plain weave with spread tows; b) plane weave with regular tows

2.2.Damage in composite material

Composites are complex engineered materials that often behave differently than common isotropic materials [12]. There are many types of damage in composite materials and the initial state of the materials is difficult, if not impossible, to characterize [2] Moreover, it is much more difficult to formulate a boundary-value problem to describe crack propagation in composite materials than in metals.

Polymer composites, which are generally used for manufacturing the aircraft components, due to their complex internal structure lead to different types of damage at many stages of their operational life. Defects that can emerge during the fabrication process of the composite materials are, for example, delamination, voids, particulates inclusion, resin-rich or resin starved, while during the aircraft operation damage are caused, mainly, by service loads and impacts.[13],[14].

These damage can decrease the residual strength and durability of the structure leading to the failure (and then the fracture) of the material [13].

It should be noted the difference between damage and failure of the material. Both terms are ambiguous and it is important to understand the difference between them. As Oluwole. L said [15]: “damage leads to failure and failure leads to fracture”. When the material is damaged, due to problems during the fabrication process (voids, particles inclusion, resin rich, etc…) or impacts during its operation, it does not means that the material failed in service. Damage is a physical discontinuity in the material that can impair its normal functioning, which does not mean, necessarily, that the material is unusable. On the other hand, when the material fails, it cannot be used in service once it has lost its integrity. Finally when the fracture of the material happens, it means it was broken into two or more parts.

2.2.1. Fracture mechanism

Fracture mechanism has evolved from the original work of Grifith [16]. Grifith recognized that defects (or damage) could lead to failure in materials, so he decided to propose and solve the idealized problem of a single crack in an infinite two-dimensional, isotropic, elastic medium under transverse load [16]. The solution obtained from the energy balance principle is given by:

$$\sigma = \sqrt{\frac{2E\gamma}{\pi a}} \tag{1}$$

where σ, is the far-field stress that cause the crack to open and grow unstable under plane stress conditions, a is the half crack length and γ represents the classical surface energy due to the breakage of bonds in the generation of new crack surface.

Later, Irwin (in 1950) generalized the form of equation (1) by introducing the macroscopic energy release rate, G, as an independent property [16]. Thus, for the same central crack problem:

$$\sigma = \sqrt{\frac{EG}{\pi a}} \tag{2}$$

where,

$$G = \frac{\partial U}{\partial A} \tag{3}$$

being U, the total potential and A the crack area.

Further, Irwin greatly expanded the utility and applicability of the method by introducing the stress intensity factor, K_I, with [16]

$$\sigma_{ij} = \frac{K_I}{\sqrt{2\pi r}} f_{ij}(\theta) \tag{4}$$

This is the form of stress field near the linear elastic square root singularity and K_I (stress intensity factor) is given by

$$K_I = \sqrt{\pi a}\sigma \tag{5}$$

Then, in more general problems,

$$K_I = \alpha\sqrt{\pi a}\sigma \tag{6}$$

for mode I crack opening conditions. Similar forms follow for the mode II and mode III (the two shear modes) [16].

Fracture mechanics considers that a failure can grow in three different modes, mode I, mode II and mode III. The first mode is the opening mode, the second mode is the in-plane shear mode and the third is the out-of-plane shear mode [17], these three different modes are represented in the Figure 2.7.

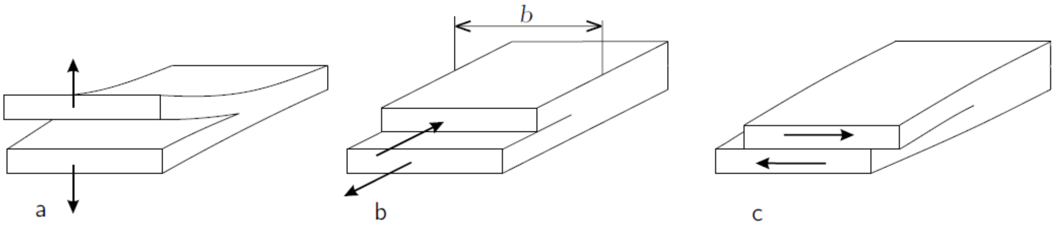

Figure 2.7 - Failure propagation modes[17]

Each of these three different modes has its critical energy G_{Ic}, G_{IIc} and G_{IIIc}, which will be used, later on this dissertation, to characterize the interface material, in order to simulate delamination between the plies. When damage propagates by combination of two distinct modes, it is called a mix mode [17].

2.2.2. Laminated damage mode

Consider composite material made of large unidirectional fibers (carbon or glass fiber, for example) embedded in polymer matrix (epoxy, for example). When a ply, without any notch, is tested, under various loading in the plane, the material fails in a manner and under certain tensions. The union of all the points, where the material suffers failure for the different stress states, generate a stress surface known as a failure criterion. In the interior of this surface are all the stress states that the material is capable to support without losing structural integrity. There are different failure modes in composite materials, which is a set of mechanisms of degradation that lead to the fracture of the material [17].

In Figure 2.8, where a unidirectional ply with the fiber oriented in the direction 1 is shown, is presented the different fracture surfaces under certain load states. The experimental observations lead to the conclusion that for an unidirectional ply under plane stress conditions there are, at least, four failure modes clearly identifiable. Figure 2.8 shows the fracture planes originated by each type of failure.

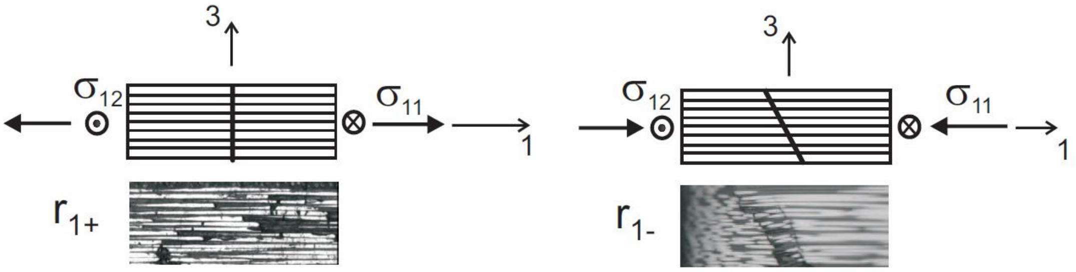

a) Longitudinal tensile fracture

b) Longitudinal compressive fracture

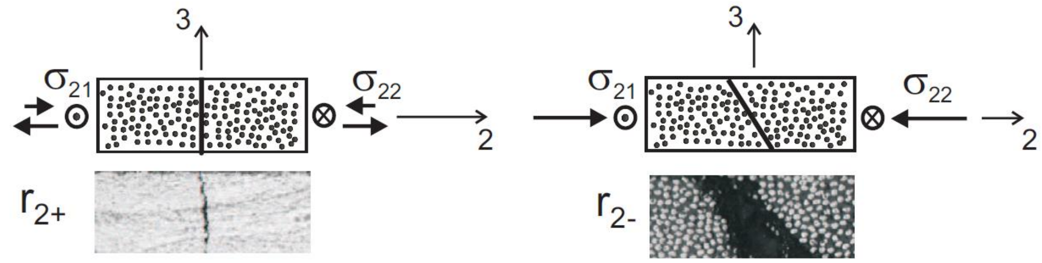

c) Transverse fracture with α=0°

d) Transverse fracture with α=53°

Figure 2.8 - "Fracture surfaces and corresponding internal variables" [18]

It is acceptable to consider the constitutive laws well approximated by a linear elastic behavior until failure, except when is applied transverse compression loads ($\sigma_{22} < 0$) or pure shear loads (σ_{12}). In these cases the material exhibits a pronounced nonlinearity before failure. [17], [18].

In Figure 2.9, it is represented the stress states that activated the respective failure modes, $F_{\alpha=0}$, $F_{\alpha\neq0}$, F_{FT} and F_{KB} in the $(\sigma_{11}-\sigma_{22})$, $(\sigma_{11}-\sigma_{12})$ and $(\sigma_{22}-\sigma_{12})$. $F_{\alpha=0}$ and $F_{\alpha\neq0}$ are the transverse failure modes or matrix failure while F_{FT} and F_{KB} are longitudinal failure modes or fiber failure.

However, due to the geometry of the material, there are 5 uniaxial tests (represented in the Figure 2.10) that are possible to perform in order to fully characterize the mechanical behavior of carbon fiber reinforced plastic: traction and compression in the direction of fibers ($\sigma_{11} > 0$ and $\sigma_{11} < 0$, respectively), traction and compression in the transverse direction of fibers ($\sigma_{22} > 0$ and $\sigma_{22} < 0$) and the pure shear test σ_{12} [17]. Each of these failure stresses is represented by X_T, X_C, Y_T, Y_C and S_L, respectively. These constants are used by the failure criteria, to define when the material fails under the action of external loads.

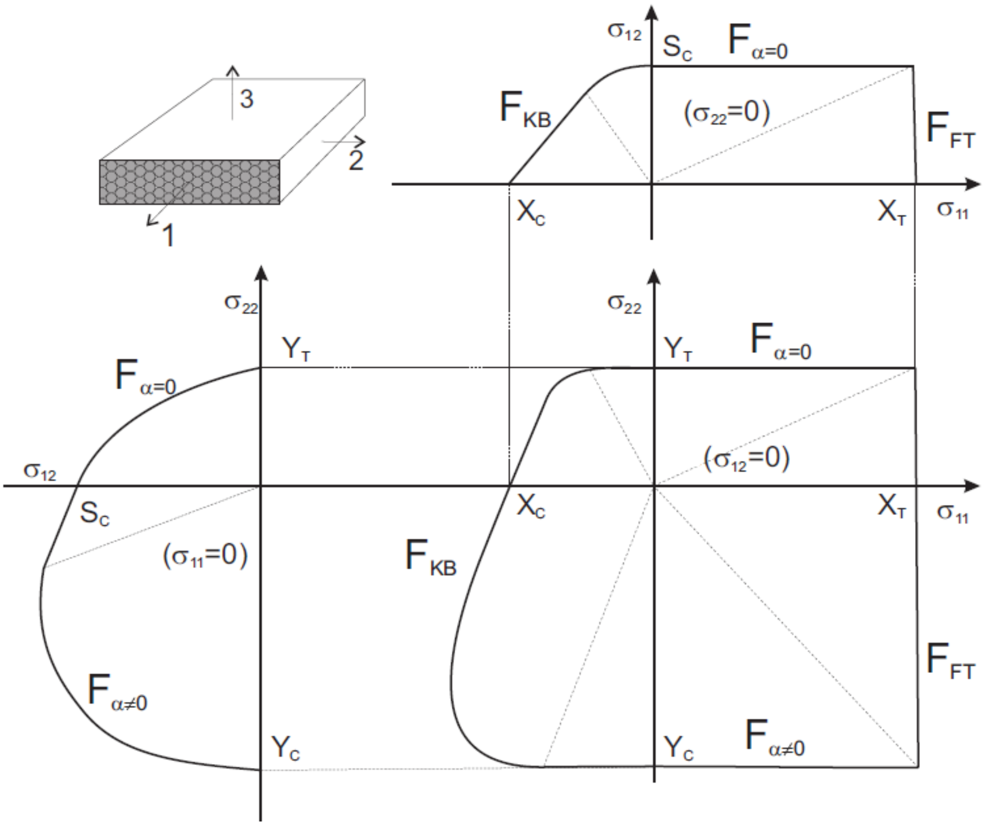

Figure 2.9 - "Fracture surfaces and corresponding internal variables"[17]

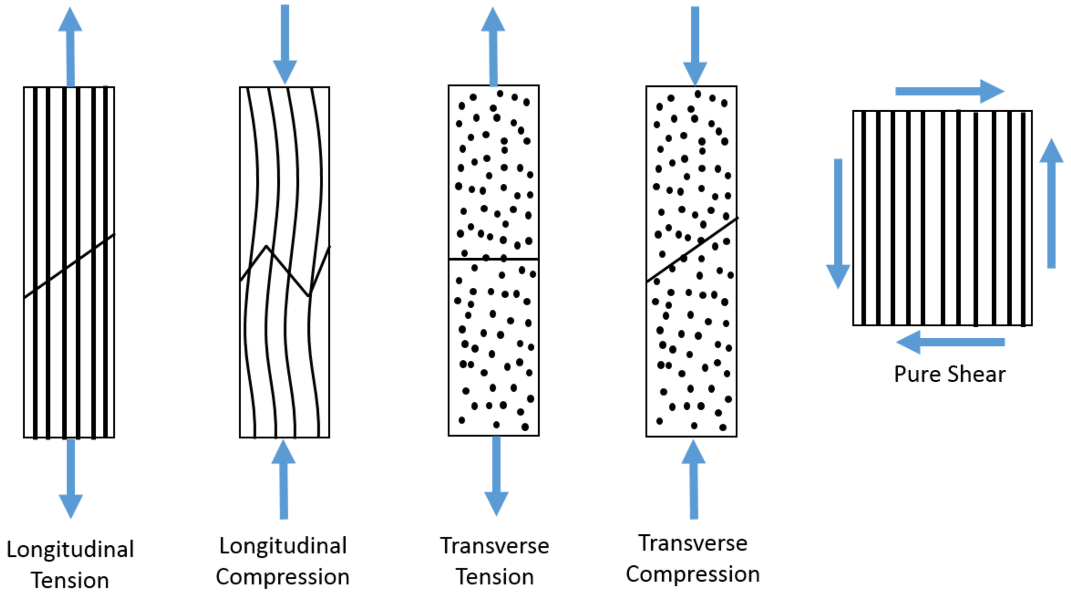

Figure 2.10 - In-plane failure modes

2.2.2.1. Longitudinal tensile fracture

This is the simplest failure mode to identify, once that in the composite reinforced with fibers the loads are transferred by these ones and, when it fails, the loads have to be redistribute by the rest of the structure areas, which can lead to structural fracture [17], [18].

Composite materials with a high fiber fraction or in which matrix ultimate deformation is higher than in fibers leads to longitudinal fracture which begins in the fibers, in regions with defects. With the occurrence of the fracture of some fibers, the loads in the neighboring increase. These loads need to be transferred by shear, between the interface and the matrix, which cause matrix cracking and fiber pull-out. The higher the loads on the fibers, the greater will be the damage in the material, which lead to structural collapse [18]. So, it can be concluded that this type of failure occurs in both fiber and matrix.

2.2.2.2. Longitudinal compressive fracture

When loads are applied in fiber direction, the laminate trend to fail by generation of *kink band*. This is the most common and most complex failure mode in this type of loading. Although this is not the only type of failure, the laminate can also fail by *microbuckling* [18].

In the *microbuckling* model, the compression failure is assumed to be triggered by the instability that occurs localized in the fibers [19]. This instability happens due to the critical loads Euler's problem which determine the moment where a bar subjected to longitudinal compression lose its equilibrium or becomes unstable before a disturbance [17].

Some researches were conducted about the time independent compression failure and the first theoretical analyses made by Rosen [20] about *microbuckling* as a phenomenon of elastic instability. But, the results were above the critical stresses needed to occur *microbuckling* [20]. Consequently, some analysis were made with the aim of improve Rosen’s model. Argon (in 1972) and Bundiansky and Fleck (in 1993) included the yield effect in the matrix, fibers misalignment and fibers extensibility [20].

In the case of carbon fibers, several researchers observed the trend of the fibers to fail in shear mode instead of failing by bending from *microbuckling*. This produce a slant failure surface and consequently dislocation slip[18].

A kink band corresponds to the last state of damage under longitudinal compression. However there is a certain controversy about the generation of a kink band. The question is: It is a failure mechanism or it is the last stage of *microbuckling*? [17].

According to Sun and Tsai [19], it is assumed that in the kink band model, the compressive failure starts with the instability or excessive rotation of a misalignment fiber. This makes the fiber and matrix transfer high stresses, causing damage, separation of the components and matrix fracture [17].

Sun and Tsai [19], after comparing microbuckling and kink band models, concluded that in the microbuckling model it is assumed failure results from an instability located on fibers supported by elastic-plastic matrix. On the other hand, in kink band model failure is triggered by “yielding of plastic shear deformation of composites”.

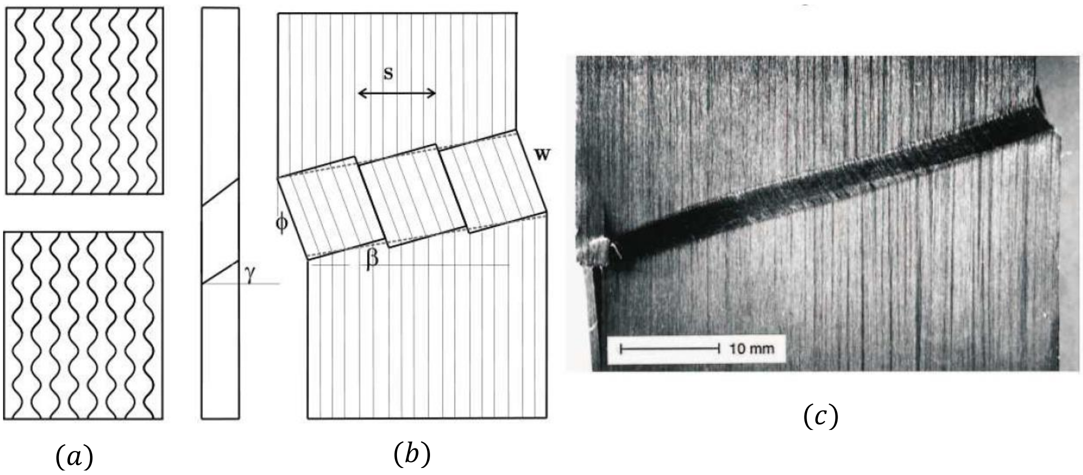

Figure 2.11 - "(a) Fiber micro buckling between an elastic matrix in shear mode (up) and in tension mode (down); (b) kink band geometry; (c) real kink band" [18]

2.2.2.3. Transverse fracture (with $\alpha = 0$)

When the load is applied under transversal tension or in-plain shear, the failure progression occurs transversely to the laminate [17], [18].

These types of failures are developed essentially by transversal tension and in-plane shear. However, under high shear stress and with a moderate value of transversal compression, failures with the same orientation can be developed (with $\alpha = 0$) [17].

It should be noted that α represent the fracture angle that is measured from normal to the top face and the fracture plane [21].

2.2.2.4. Transverse fracture (with $\alpha \neq 0$)

As Bessa referred [18], the behavior of the composite under transverse compression is very interesting, once there is a non-linearity in the stress-strain curve, which means that the composite materials plasticizes. Under transversal compression loads it is observed experimentally that the fracture angle varies with compression's strength intensity and shear.

In fact, increasing the transversal compression loads, the fracture plain angle increases [17], [18]. Koerber [21] investigate the strain rate characterization of a unidirectional ply in transverse compression and in-plain shear using digital image correlation. Concluding that the behavior of a lamina subjected to shear loads is highly nonlinear.

2.2.3. Failure criteria for plies

Failure criteria for plies determines, by the use of the failure stresses provided from the 5 uniaxial tests (X_T, X_C, Y_T, Y_C and S_L), where lie the points that defines the failure of the ply through a set of functions. So, the failure criteria are used to predict the stress values for which the material fails under the action of external loads.

In this section some of the most used failure criteria in the prediction of composite materials failure will be presented, such as: maximum stress, maximum strain, Tsai-Wu, Tsai-Hill, Hashin-Rotem, puck or LaRC03/LaRC04.

2.2.3.1. Maximum stress

The maximum stress failure criterion [22] states that failure occurs when the maximum principal stress exceeds a specific value. In this case, the maximum stress criterion can be expressed as:

$$\begin{gathered} X_C < \sigma_{11} < X_T \\ Y_C < \sigma_{22} < Y_T \\ Z_C < \sigma_{33} < Z_T \\ |\tau_{23}| < Q \\ |\tau_{13}| < R \\ |\tau_{12}| < S \end{gathered} \tag{7}$$

where X_T, Y_T and Z_T are the tensile material normal strength in X, Y and Z directions, X_C, Y_C and Z_C are the compressive material normal strength and Q, R and S are the shear material strength. The failure appears when one or more equations in (7) are not satisfied.

2.2.3.2. Maximum strain

Similar to the maximum stress failure criterion, the maximum strain can be expressed as [22]:

$$\begin{gathered} \varepsilon_{1C} < \varepsilon_{11} < \varepsilon_{1T} \\ \varepsilon_{2C} < \varepsilon_{22} < \varepsilon_{2T} \\ \varepsilon_{3C} < \varepsilon_{33} < \varepsilon_{3T} \\ |\gamma_{23}| < Q_\varepsilon \\ |\gamma_{13}| < R_\varepsilon \\ |\gamma_{12}| < S_\varepsilon \end{gathered} \tag{8}$$

where ε_{1T}, $\varepsilon_{2T}$and ε_{3T} are the tensile material normal failure strains, ε_{1C}, ε_{2C} and ε_{3C} are the compressive material normal failure strains and Q_ε, R_ε and S_ε are the material shear failure. Violation of any of equations (8) indicates the material failure.

2.2.3.3. Tsai-Wu

Tsai-Wu failure criterion is a quadratic and interactive stress-based criterion that identifies failure. This criterion is defined based on the tensile failure that occurs due to the five possible uniaxial testes, which are longitudinal tension and compression, transversal tension and compression and shear.[18], [17], [22], [23].

This failure criterion considers that directions 1, 2, 3 are not the principal directions, as maximum stress failures criterion do.

However, Tsai-Wu criterion does not distinguish between distinct modes of failure that are present in composite material [24].

This criterion can be expressed by a symmetric second order tensor:

$$f(x) = \begin{bmatrix} f_1 \\ f_2 \\ f_3 \\ 0 \\ 0 \\ 0 \end{bmatrix}^T \begin{bmatrix} \sigma_{11} \\ \sigma_{22} \\ \sigma_{33} \\ \sigma_{23} \\ \sigma_{13} \\ \sigma_{12} \end{bmatrix} + \begin{bmatrix} \sigma_{11} \\ \sigma_{22} \\ \sigma_{33} \\ \sigma_{23} \\ \sigma_{13} \\ \sigma_{12} \end{bmatrix}^T \begin{bmatrix} F_{11} & F_{12} & F_{13} & 0 & 0 & 0 \\ F_{12} & F_{22} & F_{23} & 0 & 0 & 0 \\ F_{13} & F_{23} & F_{33} & 0 & 0 & 0 \\ 0 & 0 & 0 & F_{44} & 0 & 0 \\ 0 & 0 & 0 & 0 & F_{55} & 0 \\ 0 & 0 & 0 & 0 & 0 & F_{66} \end{bmatrix} \begin{bmatrix} \sigma_{11} \\ \sigma_{22} \\ \sigma_{33} \\ \sigma_{23} \\ \sigma_{13} \\ \sigma_{12} \end{bmatrix} < 1 \tag{9}$$

It is assumed that the material is transversally isotopic, which means that $f_2 = f_3$, $F_{12} = F_{13}$, $F_{22} = F_{33}$, $F_{55} = F_{66}$ and $F_{44} = \frac{F_{22}-F_{23}}{2}$ [17].

The parameters f and F in (9) are obtained from the failure stresses by the following expressions:

$$f_1 = \frac{1}{X_T} - \frac{1}{X_C} \tag{10}$$

$$f_2 = \frac{1}{Y_T} - \frac{1}{Y_C} \tag{11}$$

$$F_{11} = \frac{1}{X_T X_c} \tag{12}$$

$$F_{22} = \frac{1}{Y_T Y_C} \tag{13}$$

$$F_{66} = \frac{1}{S_L^2} \tag{14}$$

$$F_{12} = -\frac{0.5}{X_T^2} \; or \; F_{12} = -\frac{0.5}{\sqrt{X_T X_C Y_T Y_C}} \tag{15}$$

F_{23} is not considered in in-plain problems so, in this case, it is assumed $F_{23} = 0$.

2.2.3.4. Tsai-Hill

Tsai-Hill failure criterion is an adaptation of the Von-Mises criterion [25], [26]. As Tsai-Wu failure criterion, Tsai-Hill failure criterion is not associated with failure modes and it also considers that the 1, 2, 3 directions are not aligned with the principal directions.

Since the composites are transversally isotropic, this criterion reduces to:

$$\left(\frac{\sigma_{11}}{X^2}\right)^2 + \left(\frac{\sigma_{22}}{Y}\right)^2 - \frac{\sigma_1\sigma_2}{X^2} + \left(\frac{\sigma_{12}}{S_L}\right)^2 < 1 \tag{16}$$

here, $X = X_T$ when σ_{11} is positive and when it is negative, $X = X_C$. The same happens in the second direction, if $\sigma_{22} > 0$ then $Y = Y_T$, but if $\sigma_{22} < 0$ then $Y = Y_C$.

2.2.3.5. Hashin-Rotem

Hashin created the need for failure criterion that are based on failure mechanism [27]. He developed two different failure criterion, one of them was related to fiber failure and the other one was related to matrix failure [27].

In 1978 [28], [17], [29], [25], Hashin and Rotem developed a failure criterion for unidirectional laminates submitted to cyclic loads, distinguishing tensile loads from compressive loads. This criterion regards that failure of the material happens when the following equations are not satisfied:

$$\begin{aligned}
&\sigma_{11} < X_T && \text{if } \sigma_{11} > 0 \\
&-\sigma_{11} < X_C && \text{if } \sigma_{11} < 0 \\
&\left(\frac{\sigma_{22}}{Y_T}\right)^2 + \left(\frac{\sigma_{12}}{S_L}\right)^2 < 1 && \text{if } \sigma_{22} > 0 \\
&\left(\frac{\sigma_{22}}{Y_C}\right)^2 + \left(\frac{\sigma_{12}}{S_L}\right)^2 < 1 && \text{if } \sigma_{22} < 0
\end{aligned} \tag{17}$$

Later, Hashin introduced the failure criterion for fibrous composites under a three dimensional stress state.[25], [29]

So, Hashin criterion can be described as:

$$
\begin{aligned}
&\left(\frac{\sigma_{11}}{X_T}\right)^2 + \frac{\sigma_{12}^2 + \sigma_{13}^2}{S_L^2} < 1, && if\ \sigma_{11} > 0 \\
&-\sigma_{11} < X_C, && if\ \sigma_{11} < 0 \\
&\left(\frac{\sigma_2 + \sigma_3}{Y_T}\right)^2 + \frac{\sigma_{23}^2 - \sigma_2\sigma_3}{S_T^2} + \frac{\sigma_{12}^2 + \sigma_{13}^2}{S_L^2} < 1, && if\ (\sigma_2 + \sigma_3) > 0 \\
&\left[\left(\frac{Y_C}{2S_T}\right)^2 - 1\right]\frac{\sigma_2 + \sigma_3}{Y_C} + \left(\frac{\sigma_2 + \sigma_3}{2S_T}\right)^2 + \frac{\sigma_{23}^2 - \sigma_2\sigma_3}{S_T^2} + \frac{\sigma_{12}^2 + \sigma_{13}^2}{S_L^2} < 1, && if\ (\sigma_2 + \sigma_3) < 0
\end{aligned}
\tag{18}
$$

where S_T, represents the shear in 23 plain. The approximation describes the basic failure mechanisms but it is not capable to describe the kink band formulation [17], [24]

2.2.3.6. Puck

The principal difference between puck criterion and Hashin [17], [25], criterion is that, in this one, three modes matrix cracking are considered, differing in the angle between the fracture plane on the lamina and the type of load which causes the fracture, as seen in Figure 2.12.

Puck’s criterion [30], identifies the fiber failure and inter fiber failure in a unidirectional composite. He separates, not only the inter fiber failure in three physical modes, but also the fiber failure in two different modes (tensile fiber failure and compressive fiber failure).

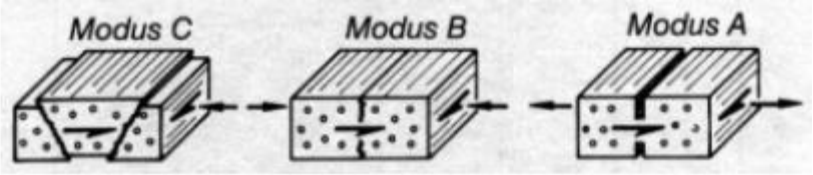

Figure 2.12 - Inter/fiber fracture modes [25]

2.2.3.7. LaRC03/04

Similarly to what happens in Puck's criterion, LaRC03 and LaRC04 [17] criteria consider the different processes in each failure mechanism.

In these criteria it is taking into account that the transverse strength varies in function of the elastic characteristics of the laminate [17].

The principal difference between LaRC03 [27] and LaRC04 failure criterion [31] is that LaRC03 failure criterion just takes into account the in-plane tensions, while LaRC04 allows taking into account the three-dimensional stress-states. [17]

2.2.3.7.1. LaRC03 Failure criteria

LaRC03 [27] failure criterion can predict matrix and fiber failure accurately, without the parameters provided by the curve-fitting and it consists of 6 expressions.

The following equations that will be presented in this section can be seen, with full demonstration, in Davila's article [27]

LaRC03 criterion for matrix failure under transverse compression ($\boldsymbol{\sigma_{22} < 0}$)

The failure index for matrix compression is given by the following expression [27]:

LaRC03#1

$$FI_M = \left(\frac{\tau_{eff}^T}{S_T}\right)^2 + \left(\frac{\tau_{eff}^L}{S_{L_{is}}}\right)^2 \leq 1 \qquad (19)$$

S_T and $S_{L_{is}}$ are the transverse (23 plane) and longitudinal (12 plane) shear strength. And the "*is*" subscript means that the "in situ longitudinal shear strength rather than the strength of a unidirectional laminate should be used" [27]. In situ effects, here, means that the longitudinal shear strength varies with the elastic properties of the laminate.

The expressions needed to complete the equation (19) are the following:

$$\tau_{eff}^T = \langle |\tau^T| + \eta^T \sigma_n \rangle \qquad (20)$$

$$\tau_{eff}^L = \langle |\tau^L| + \eta^L \sigma_n \rangle \qquad (21)$$

where $\tan^{-1}(\eta)$, in the literature, represents the angle of the internal friction and it is assumed to be a material constant [27].

$$\begin{aligned}\sigma_n &= \sigma_{22}\cos^2\alpha \\ \tau^T &= -\sigma_{22}\sin\alpha\cos\alpha \\ \tau^L &= \tau_{12}\cos\alpha\end{aligned} \tag{22}$$

and α is the angle of the fracture plane and varies between 0° and 90°.

The coefficients of influence (η^L and η^T) can be obtained from the case of unidirectional transverse compression, where $\sigma_{22} < 0$ and $\tau_{12} = 0$. For more details of this demonstration, see Davila's article [27].

$$\eta^T = -\frac{1}{\tan 2\alpha_0} \tag{23}$$

$$\eta^L = -\frac{S_L\cos 2\alpha_0}{Y_C\cos^2\alpha_0} \tag{24}$$

where α_0 represents the fracture angle that maximizes the effective transverse shear (τ^T_{eff}).

LaRC03 criterion for matrix failure: under transverse tension ($\boldsymbol{\sigma_{22} > 0}$)

The failure index for matrix tension is given by the following expression [27]:

LaRC03#2

$$FI_M = (1-g)\left(\frac{\sigma_{22}}{Y_{T_{is}}}\right) + g\left(\frac{\sigma_{22}}{Y_{T_{is}}}\right)^2 + \left(\frac{\tau_{12}}{S_{L_{is}}}\right)^2 \leq 1 \tag{25}$$

where g (material constant) is given by:

$$g = \frac{G_{Ic}}{G_{IIc}} = \frac{\Lambda^0_{22}}{\Lambda^0_{44}}\left(\frac{Y_{T_{is}}}{S_{L_{is}}}\right)^2 \tag{26}$$

and the parameters Λ^0_{jj} are calculated as:

$$\begin{aligned}\Lambda^0_{22} &= 2\left(\frac{1}{E_2} - \frac{\nu^2_{12}}{E_1}\right) \\ \Lambda^0_{44} &= \frac{1}{G_{12}}\end{aligned} \tag{27}$$

LaRC03 criterion for fiber failure: under longitudinal tension ($\boldsymbol{\sigma_{11} > 0}$)

The failure index for fiber tensile failure is given by the following expression [27]:

LaRC03#3 $$FI_F = \frac{\varepsilon_{11}}{\varepsilon_{1T}} \tag{28}$$

As it can be seen by equation (28), the LaRC03 criterion for fiber tension failure is based on the maximum allowable strain criterion, where the young's moduli and the fiber volume fraction don't interfere [27].

LaRC03 criterion for fiber failure: under longitudinal compression ($\boldsymbol{\sigma_{11} > 0}$)

The fiber compression failure by the formation of a kink band is predicted using the stresses presented in the following equation (29) and the failure criterion for the matrix tension (**LaRC03#5**) or matrix compression (**LaRC03#4)** [27].

$$\begin{aligned}
\sigma_{11}^{m} &= \cos^2\varphi\,\sigma_{11} + \sin^2\varphi\,\sigma_{22} + 2\sin\varphi\cos\varphi\,|\tau_{12}| \\
\sigma_{22}^{m} &= \sin^2\varphi\,\sigma_{11} + \cos^2\varphi\,\sigma_{22} - 2\sin\varphi\cos\varphi\,|\tau_{12}| \\
\tau_{12}^{m} &= -\sin\varphi\cos\varphi\,\sigma_{11} + \sin\varphi\cos\varphi\,\sigma_{22} + (\cos^2\varphi - \sin^2\varphi)|\tau\_12\,|
\end{aligned} \tag{29}$$

So, the criterion for fiber kinking with matrix compression failure criterion is given by:

LaRC03#4 $$FI_F = \left\langle \frac{|\tau_{12}^{m}| + \eta^{L}\sigma_{22}^{m}}{S_{L_{is}}} \right\rangle \leq 1 \tag{30}$$

The criterion for fiber kinking with matrix tension failure criterion is giver by:

LaRC03#5 $$FI_F = (1-g)\left(\frac{\sigma_{22}^{m}}{Y_{T_{is}}}\right) + g\left(\frac{\sigma_{22}^{m}}{Y_{T_{is}}}\right)^2 + \left(\frac{\tau_{12}^{m}}{S_{L_{is}}}\right)^2 \leq 1 \tag{31}$$

LaRC03 criterion for matrix damage in biaxial compression

LaRC03#6 $$FI_M = \left(\frac{\tau_{eff}^{mT}}{S_T}\right)^2 + \left(\frac{\tau_{eff}^{mL}}{S_{L_{is}}}\right)^2 \leq 1 \tag{32}$$

where the effective shear stresses, τ_{eff}^{mT} and τ_{eff}^{mL} are defined by:

$$\begin{aligned}\tau_{eff}^{mT} &= \langle -\sigma_{22}^{m} \cos\alpha \,(\sin\alpha - \eta^{T} \cos\alpha) \rangle \\ \tau_{eff}^{mL} &= \langle \cos\alpha (|\tau_{12}^{m}| + \eta^{L} \sigma_{22}^{m} \cos\alpha) \rangle \end{aligned} \tag{33}$$

2.2.3.7.2. LaRC04 Failure criterion

LaRC04 failure criterion [31]consists of six expressions that are used for design proposes. This criterion is based on physical models for each failure mode, as it was said, and it takes into consideration the non-linear matrix shear behavior.

In this criterion, the required unidirectional material properties are E_{11}, E_{22}, G_{12}, v_{12}, X_T, X_C, Y_T, Y_C, S_L, G_{Ic}, G_{IIc}, η^L and α_0. These last two properties are optional.

LaRC04 criterion for matrix failure: under transverse tension ($\boldsymbol{\sigma_{22} > 0}$)

The failure index for matrix tension depends on the ply stresses and in-situ strengths [31]

LaRC04#1

$$FI_M = (1-g)\frac{\sigma_{22}}{Y_{T_{is}}} + g\left(\frac{\sigma_{22}}{Y_{T_{is}}}\right)^2 + \frac{\Lambda_{23}^0 \tau_{23}^2 + \chi(\gamma_{12})}{\chi(\gamma_{12|is}^u)} \leq 1 \tag{34}$$

where, the in-situ strength values for the thick embedded plies are [31]:

$$\begin{aligned} Y_{T_{is}} &= 1.12\sqrt{2}T_T \\ \gamma_{12|is}^u &= \chi^{-1}[2\chi(\gamma_{12}^u)] \end{aligned} \tag{35}$$

and the in-situ strengths for the thin embedded plies are [31]:

$$Y_{T_{is}} = \sqrt{\frac{8G_{Ic}}{\pi t \Lambda_{22}^0}} \tag{36}$$

$$\Lambda_{22}^0 = 2\left(\frac{1}{E_{22}} - \frac{v_{21}^2}{E_{11}}\right) \tag{37}$$

$$\gamma_{12|is}^u = \chi^{-1}\left(\frac{8G_{IIc}}{\pi t}\right) \tag{38}$$

g is obtained form the fracture mechanics test data [31]:

$$g = \frac{G_{Ic}}{G_{IIc}} \tag{39}$$

LaRC04 criterion for matrix failure: under transverse compression ($\boldsymbol{\sigma_{22} < 0}$)

The LaRC04 failure index for matrix compression is given by the following equation [31]:

LaRC04#2

$$FI_M = \left(\frac{\tau^T}{S_T - \eta^T \sigma_n}\right)^2 + \left(\frac{\tau^L}{S_{L_{is}} - \eta^L \sigma_n}\right)^2 \leq 1 \tag{40}$$

The fracture angle for pure transverse compression can be considered equal to $\alpha_0 = 53°$ if an experimental value does not exist, so the transversal coefficient of influence η^T can be obtained with [31]:

$$\tan(2\alpha_0) = -\frac{1}{\eta^T} \tag{41}$$

where the transverse strength is [31]:

$$S_T = Y_C \cos\alpha_0 \left(\sin\alpha_0 + \frac{\cos\alpha_0}{\tan 2\alpha_0}\right) \tag{42}$$

and

$$\frac{\eta^L}{S_{L_{is}}} = \frac{\eta^T}{S_T} \tag{43}$$

The expression (41) is used in the absence of experimental data to obtain the longitudinal coefficient of influence (η^L).

The stresses in the potential fracture planes are expresses by [31]:

$$\begin{aligned} \sigma_n &= \frac{\sigma_{22} + \sigma_{33}}{2} + \frac{(\sigma_{22} - \sigma_{33})}{2} \cos 2\alpha + \tau_{23} \sin 2\alpha \\ \tau^T &= \frac{\sigma_{22} + \sigma_{33}}{2} - \frac{\sigma_{22} - \sigma_{33}}{2} \sin 2\alpha + \tau_{23} \cos 2\alpha \\ \tau^L &= \tau_{12} \cos\alpha + \tau_{31} \sin\alpha \end{aligned} \tag{44}$$

LaRC04 criterion for tensile fiber failure ($\boldsymbol{\sigma_{11} > 0}$)

The LaRC04 failure index for tensile fiber failure is expressed as [31]:

LaRC04#3 $$FI_F = \frac{\sigma_{11}}{X_T} \leq 1 \tag{45}$$

This criterion is a non-interacting maximum allowable stress criterion [31].

LaRC04 criterion for compressive fiber failure ($\boldsymbol{\sigma_{11} < 0}$)

Fiber compression failure is a complex field, where, depending on the material, different compressive failure modes can occur [31]. These failure modes are micro buckling, kinking and fiber failure.

For the failure mode with the kink band formation, ($\sigma_{2^m2^m} < 0$) it is predicted the following criterion:

LaRC04#4 $$FI_F = \left(\frac{|\tau_{1^m2^m}|}{S_{L_{is}} - \eta^L \sigma_{2^m2^m}}\right) \leq 1 \tag{46}$$

For matrix failure under biaxial compression the criterion is predicted as [31]:

LaRC04#5 $$FI_M = \left(\frac{\tau^{TM}}{S_T - \eta^T \sigma_n^m}\right)^2 + \left(\frac{\tau^{Lm}}{S_L - \eta^L \sigma_n^m}\right)^2 \leq 1 \tag{47}$$

where,

$$\begin{aligned}
\sigma_n^m &= \frac{\sigma_{2^m2^m} + \sigma_{3^\psi3^\psi}}{2} + \frac{\sigma_{2^m2^m} - \sigma_{3^\psi3^\psi}}{2}\cos 2\alpha + \tau_{2^m3^\psi}\sin 2\alpha \\
\tau^{Tm} &= -\frac{\sigma_{2^m2^m} - \sigma_{3^\psi3^\psi}}{2}\sin 2\alpha + \tau_{2^m3^\psi}\cos 2\alpha \\
\tau^{Lm} &= \tau_{1^m2^m}\cos\alpha + \tau_{3^\psi1^m}\sin\alpha
\end{aligned} \tag{48}$$

The criterion for matrix tensile failure under longitudinal compressive ($\sigma_{2^m2^m} \geq 0$) is given by [31]:

LaRC04#6 $$FI_{M/F} = (1-g)\frac{\sigma_{2^m2^m}}{Y_{T_{is}}} + g\left(\frac{\sigma_{2^m2^m}}{Y_{T_{is}}}\right)^2 + \frac{\Lambda_{23}^0 \tau_{2^m3^\psi}^2 + \chi(\gamma_{1^m2^m})}{\chi(\gamma_{12|is}^u)} \leq 1 \tag{49}$$

The expressions for fiber kinking failure are set out below. The plane where the kinking takes place is [31]:

$$\tan 2\psi = \frac{2\tau_{23}}{\sigma_{22} - \sigma_{33}} \tag{50}$$

And the stresses rotated to that plane are [31]:

$$\begin{aligned}
&\sigma_{2^{\psi}2^{\psi}} = \frac{\sigma_{22} + \sigma_{33}}{2} + \frac{\sigma_{22} - \sigma_{33}}{2}\cos(2\psi) + \tau_{23}\sin(2\psi)\\
&\sigma_{3^{\psi}3^{\psi}} = \sigma_{22} + \sigma_{33} - \sigma_{2^{\psi}2^{\psi}}\\
&\tau_{12^{\psi}} = \tau_{12}\cos(\psi) + \tau_{31}\sin(\psi)\\
&\tau_{2^{\psi}3^{\psi}} = 0\\
&\tau_{3^{\psi}1} = \tau_{31}\cos(\psi) - \tau_{12}\sin(\psi)
\end{aligned} \tag{51}$$

After knowing the orientation of the misalignment frame, the stresses can be rotated to it using [31]:

$$\begin{aligned}
&\sigma_{1^{m}1^{m}} = \frac{\sigma_{11} + \sigma_{2^{\psi}2^{\psi}}}{2} + \frac{\sigma_{11} - \sigma_{2^{\psi}2^{\psi}}}{2}\cos(2\varphi) + \tau_{12^{\psi}}\sin(2\varphi)\\
&\sigma_{2^{m}2^{m}} = \sigma_{11} + \sigma_{2^{\psi}2^{\psi}} - \sigma_{1^{m}1^{m}}\\
&\tau_{1^{m}2^{m}} = -\frac{\sigma_{11} - \sigma_{2^{\psi}2^{\psi}}}{2}\sin(2\varphi) + \tau_{12^{\psi}}\cos(\varphi)\\
&\tau_{2^{m}3^{\psi}} = \tau_{2^{\psi}3^{\psi}}\cos(\varphi) - \tau_{3^{\psi}1}\sin(\varphi)\\
&\tau_{3^{\psi}1^{m}} = \tau_{3^{\psi}1^{\psi}}\cos(\varphi)
\end{aligned} \tag{52}$$

For more detailed information about the demonstration of the expressions used in LaRC04 failure criteriin, please see the reference of Pinho's article[31].

2.3.Characterization of multi-scale models

The multi-scale models are really important to understand complex materials, such as composite materials. The applications related to this kind of problems involve different length scales in a range from μm (micro-scale) to m (macro-scale). Using the concept of representative volume element (RVE) theoretical background is discussed in this section as well as numerical treatment of the resulting three-dimensional representative volume element [32].

These multi-scale models can yield predictive insight into the origins of damage tolerance, leading to the investigation of damage and failure under more complex loading and environmental conditions, such as stress rupture and fatigue [33].

Damage phenomena [34] in composite materials are truly complex as a result of its significant heterogeneities. So, typically, damage can be discrete, for atomistic voids lattice defects (which will be discussed in this thesis), or it can be continuous, for micromechanical and macromechanical scales.

For fiber reinforced plastics, damage relevant [33] to macroscopic failure appear at many length scales: at the smallest scale, there are defects presented on fibers that propagate and leads to fiber cracks. Deboning, sliding or matrix yielding at crack perimeter, which occurs in a bigger scale, limit the crack propagation into the matrix, however, these types of damages are very complex. Finally, loads carried by the broken fibers are redistribute to other fibers (the unbroken fibers) and matrix and subsequent damage occurs in and around the fibers according to the distribution of the defects in the fibers and the applied stress and stress redistribution. Consequently, macro-cracks will be formed and propagate leading to the composite failure.

Figure 2.13, represent the damage evolution of the fiber reinforced composites at different length scales [33].

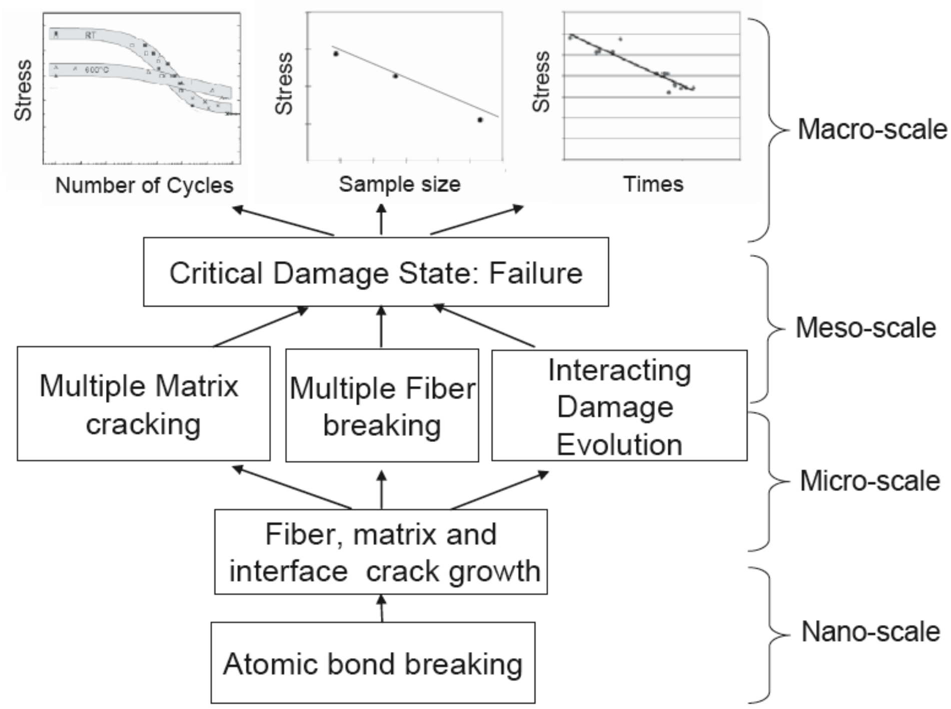
Stress
RT
600°C
Number of Cycles
Stress
Sample size
Stress
Times
Macro-scale
Critical Damage State: Failure
Meso-scale
Multiple Matrix cracking
Multiple Fiber breaking
Interacting Damage Evolution
Micro-scale
Fiber, matrix and interface crack growth
Atomic bond breaking
Nano-scale

Figure 2.13 - "Multi-scale damage and failure in fiber reinforced composites" [33]

Figure 2.14, shows different geometries between micro-scale, meso-scale and macro-scale.

Micro scale [35] geometry (Figure 2.14-(a)) consists of unidirectional fibers (carbon fibers, for example) surrounded by a thin interface layer and embedded in an epoxy matrix. In meso-scale geometry (Figure 2.14-(b)) carbon yarns in a balanced 0º/90º spread tow carbon fabric arrangement are presented and, once again, it is all embedded in epoxy matrix. Lastly, the macro-scale geometry (Figure 2.14-(c)) represents a hybrid carbo epoxy composite laminate. This laminate consists of a spread tow carbon fabric plies oriented at 0º/90º and incorporated in a multi-layered structure.

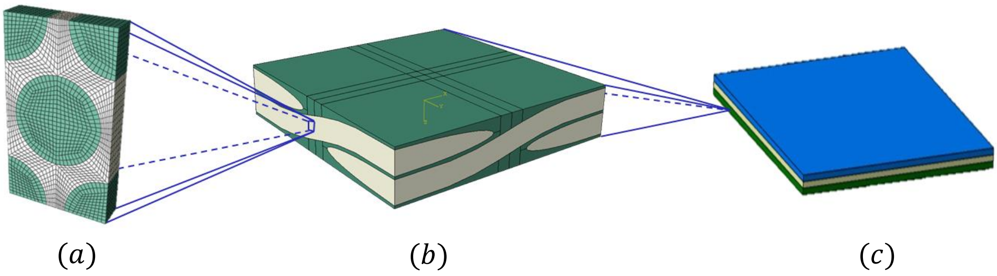

Figure 2.14 - Different geometries for: (a) micro-scale, (b) meso-scale and (c) macro-scale [35]

2.3.1. Micro-scale models

At the micro-scale geometry, fibers are embedded in matrix material to form a yarn or a tow.[35]. These models are based on a representative volume element (RVE), of the composite material, which is composed by a cylindrical fiber surrounded by a tube shape interface embedded in epoxy matrix [36].

According to Xia and Curtin [37], "*the goal of modeling at the micro mechanics scale is to compute the detailed stress distribution around broken fibers with various interfacial deformation models and extract from such studies the average stress concentrations induced in the surrounding unbroken fibers and the stress recovery along the broken fibers due to the interface shear resistance".*

This type of model, with a high special refinement must be used to study problems such as introduction of fiber break or matrix crack that induces large stress changes in the neighboring of the crack [37].

Despite the micro-scale modeling approach allows obtaining an approximate prediction of effective properties of unidirectional lamina, when expanded to more complex structures, the limitations of this model are revealed as the micro-mechanical models are unable to account for detailed fabric geometry [36], as the number of finite elements involved is excessively high.

Also, this type of models could be used as the first level of a multiscale simulation.

2.3.1. Meso-scale models

At the meso-scale level the laminate is considered homogeneous and undamaged material is considered orthotropic or transversely isotropic. These models are used to describe and predict damage and failure of composite materials [37] For that, meso-scale is the chosen scale that will be used in the numerical models developed in this thesis.

The analysis of the textile composites at this scale will lead to non-uniform stress distributions over the unit cell (which is different from the results provided by the micro-scale approaches) [36].

By implementing specific failure modes for the different constitutes, it can be obtained acceptable predictions of damage initiation and progression [36]

In 2010, Bessa [18] used meso-mechanical models for prediction of damage and final fracture of notched and unnotched composite structures. In these models he represents a laminate where a single three-dimensional continuum element is used to represent the whole thickness of the ply, and cohesive surfaces represent the interface between the plies. In sum, the three dimensional continuum elements should be able to represent the failure of the ply and the cohesive elements to simulate the delamination between the plies.

2.3.1.1. Introduction to damage description in the meso-scale

This topic describes the damage in meso-scale and it is based on Maimi's PhD thesis [17] and Bessa's master dissertation [18]

If the material model is not isotropic the number of independent damage variables that can be defined to keep the principal directions of the material unchanged is equal to the number of the elastic parameters of the material. Namely, 5 damage variables for transversely isotropic materials, 9 variables for an orthotropic material and 21 for a completely anisotropic material.

This group of scalar variables that describe damage represents crack orientation according to the materials preferential direction and it does not consider that load's direction can influence the cracks orientation. This assumption is very common for composite laminae. Numerous experimental works with this type of materials show that the cracks are generated in the fibers' transverse direction, which means matrix failure, or in the longitudinal direction (fibers' direction), in other words, fiber's failure. This means that all the possible orientations are reduced mainly to two planes.

The most general way to relate the undamaged stiffness tensor, C_{mnst}^{0}, of the material with the damage state is by the use of a eight order tensor, $(I_{ijklmnst} - D_{ijklmnst})$:

$$C_{ijkl} = \left(I_{ijklmnst} - D_{ijklmnst}\right) * C_{mnst}^{0} \tag{53}$$

where I is the identity matrix and D is the tensor formed by scalar damage variables.

However, due to the great complexity and to the impossibility of determining the parameters for the eight order tensor, these tensors are not commonly used.

To simplify the damage constitutive tensor some hypothesis are consider that can relate kinematically the damage state of the material with an effective space of the undamaged material. The stresses and strains in the effective space (of the undamaged material) follow the initial elastic law ($\tilde{\sigma} = C_0 : \tilde{\varepsilon}$). In physical space, nominal stresses and strains are obtained by defining a relation between them and the effective stresses and strains.

Figure 2.15 presents the three main principles that can be followed to define those relations:

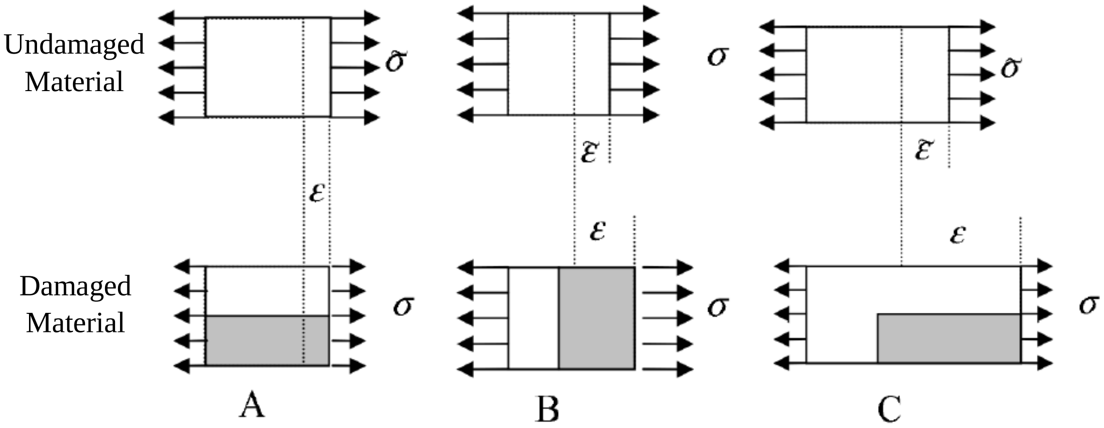
Undamaged Material
$\tilde{\sigma}$
σ
$\tilde{\sigma}$
ε
$\tilde{\varepsilon}$
$\tilde{\varepsilon}$
ε
ε
Damaged Material
σ
σ
σ
A
B
C

Figure 2.15 - "Hypothesis of A) strain equivalence, B) stress equivalence and C) energy equivalence between the damage physical space and undamaged effective space"[18],[17]

Strain equivalence principal

The effective stress applied to the undamaged material ($\tilde{\sigma}$) causes the same strains that the nominal stress applied to the damage material. This results in a relation between the nominal stress (σ) and the effective stress ($\tilde{\sigma}$):

$$\begin{aligned} \sigma &= (I - D) : \tilde{\sigma} \\ \sigma &= (I - D) : C_0 : \varepsilon \end{aligned} \tag{54}$$

Stress equivalence principle

The effective strain ($\tilde{\varepsilon}$) applied to the undamaged material causes the same stresses that the nominal strain applied to the damage material (ε). This results in a relation between the nominal strains (ε) and the effective strains ($\tilde{\varepsilon}$):

$$\begin{aligned} \tilde{\varepsilon} &= (I - D) : \varepsilon \\ \sigma &= C_0 : (I - D) : \varepsilon \end{aligned} \tag{55}$$

Energy equivalence principle

Helmholtz free energy density (Ψ) stored in the undamaged material under an effective strain is equal to the free energy density stored in the damaged material under a normal strain. At the same time, the complementary energy density stored in the undamaged material under an effective stress is equal to the complementary energy density stored in the damage material under a nominal stress.

$$\begin{aligned} \Psi &= \frac{1}{2}\tilde{\varepsilon}\colon C_0\colon \tilde{\varepsilon} \\ \bar{G} &= \frac{1}{2}\tilde{\sigma}\colon C_0^{-1}\colon \tilde{\sigma} = \frac{1}{2}\sigma\colon C_0^{-1}\colon \sigma \end{aligned} \tag{56}$$

Resulting in:

$$\sigma = (I - D)\colon C_0\colon (I - D)\varepsilon \tag{57}$$

2.3.2. Macro-scale models

The propose of this models is to analyze the response of large structures [36]. At this level, the whole structure is considered homogeneous and continuum and the behavior of the material follows an anisotropic constitutive law [33].

Some macro-scale composite materials models are available in commercial finite element codes and rely on classical laminate plate theory. These models need a set of effective material parameters that can be obtained by meso-scale models and appropriate experimental tests [36].

Macro-scale models are phenomenological based and limited to particular tests conditions and are computationally efficient in an impact simulation, but they are unable to predict the behavior of the fiber, matrix or fiber/matrix interface [36].

Chapter 3.

Ply numerical model

This chapter describes the implementation of the first numerical model used to simulate the behavior of a spread tow carbon fabric ply oriented at 0°/90° under static tension loads. In order to follow the equilibrium path until collapse, a successively increasing displacement is imposed at the ply boundary.

For this first model, a linear elastic orthotropic behavior is considered. In the interfaces between different spread tows, cohesive elements and contacts were implemented with the aim of simulating delamination that occurred during the experimental tests.

3.1. Spread Tow Carbon fabric ply: initial model description

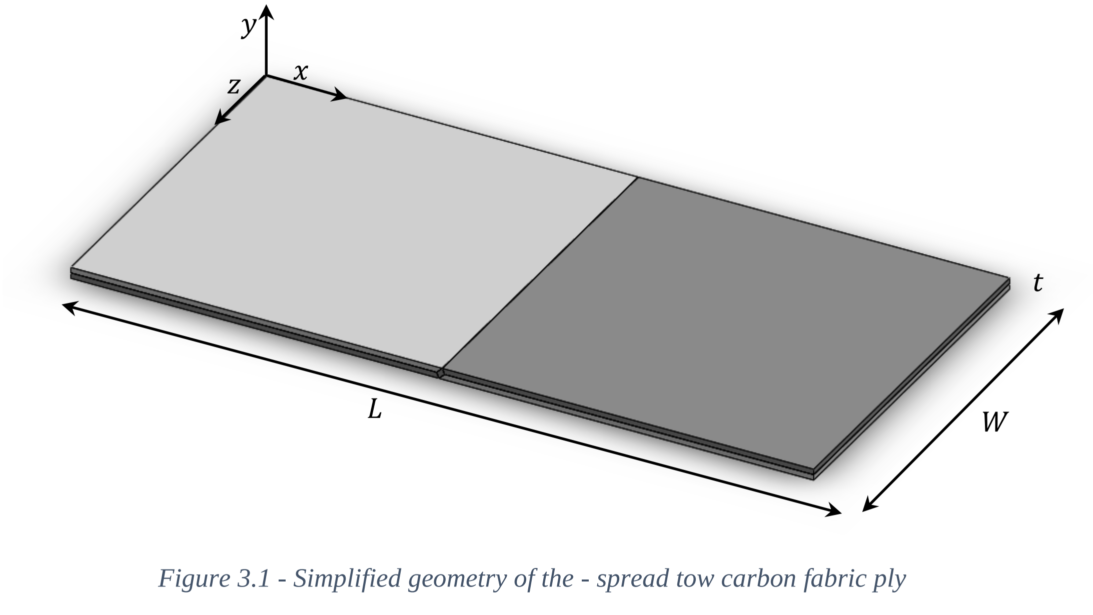

Figure 3.1 - Simplified geometry of the - spread tow carbon fabric ply

Figure 3.1 represents the spread tow carbon fabric ply geometry that is used to test the behavior of the material under an applied displacement. The main goal of this first model is to obtain the most suitable element size of the mesh and also to test the methodologies developed on a comparatively smaller model than the complete 26 plies final model, such loads are perfectly capable to fulfill this objective.

As it can be seen, the spread tow carbon fabric ply is composed by unidirectional carbon yarns in a balanced 0°/90° arrangement, where the dark gray represent the fibers oriented at 0º with the xx axis, while the light gray represent the fibers oriented at 90º. To start, it was considered that the unidirectional carbon fibers have the same mechanical properties as a Hexcel Ply IM7/8552. The dimensions of the spread tow carbon fabric ply represented in the Figure 3.1 are indicated in the Table 3.1.

Table 3.1 - Spread tow carbon fabric ply dimensions

Length, L (mm)	19.998 ± 0.001
Width, W (mm)	10.269 ± 0.021
Woven thickness, t (mm)	0.226269
Carbon fiber yarns thickness (mm)	0.113135

A linear elastic orthotropic behavior was assumed for this model, and the mechanical properties were taken from Table 3.2 [38],[39]:

After the definition of the geometry and the elastic properties, a static displacement was applied at the boundary in the xx direction, along the length of the ply, with the value of 0.2 mm, in order to find the right element size and element type that should be used, in this dissertation, to study this numerical model.

Table 3.2 - Elastic properties of IM7/8552 unidirectional laminates

E_{11} $[GPa]$	E_{22} $[GPa]$	E_{33} $[GPa]$	v_{12}	v_{23}	v_{13}	G_{12} $[MPa]$	G_{23} $[MPa]$	G_{13} $[MPa]$
164 150^{1*}	12	12	0.32^{*}	0.436^{*}	0.32^{*}	5170^{*}	3980^{*}	5170^{*}

* Values taken from Kawashita’s article [38].
1* Value for compression loads

3.2.Mesh Convergence

As mentioned, an initial model with a simplified geometry was built, containing three different volumes representing the interlaced yarns of the spread tow carbon fabric ply, a good choice regarding the element type that will be used, in the analytical model, as well as the number of elements necessary to achieve good results taking into account the computational cost.

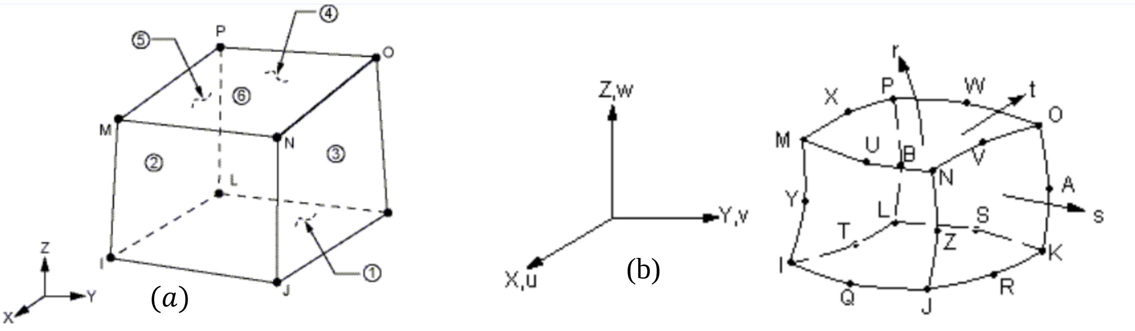

Figure 3.2 - Representative elements (a) - Brick 8 nodes and (b) Brick 20 nodes [40]

Several analysis were made with two types of elements: *Brick 8 nodes* element, SOLID185 in Ansys software, and Brick 20 nodes element, SOLID186 in Ansys software [40] (in Figure 3.2 these two types of elements are represented, allowing a better perception of the differences between them). Two analysis were made using each of these element types, a *full integration* and a *reduced integration*, which results in four different tests that were carried out for each different mesh sizes (varying the size of the element).

To solve finite element problems [41],[42], is normally necessary to use numerical integration to calculate the stiffness matrix. The functions that need to be integrated, are computed at a discrete number of points (Gaussian points) and the position of these points is calculated in order to reduce the integration errors. For each of the Gaussian points, the function is multiplied by an optimized weight and the integral is numerically computed as a weighted sum of function values times prescribed weights.

The difference between full integration and reduced integration is that when using reduced integration to solve the integral, the number of Gaussian points used is smaller than the required minimum number according to the order of the polynomial function being integrated while in full integration analyses, all the Gaussian points are used. Obviously, the accuracy of the results is related with the number of the Gaussian points used for each element, but the computational cost has to be taken into account when dealing with complex models with a great number of elements.

The different meshes used for this geometry and for the four types of analyses ranges from 18 elements (a coarse mesh), which means an element size of 5 mm, to 197760 elements with an element size of 0.078125 mm (a very refined mesh).

Figure 3.3 shows the location (in the simplified geometry) of the points where the Von Mises stress results were taken for the convergence analysis. Point A and B are in the middle of different unidirectional plies and point C1 and C2 are near to the change of cell (the location where the higher stresses are expected).

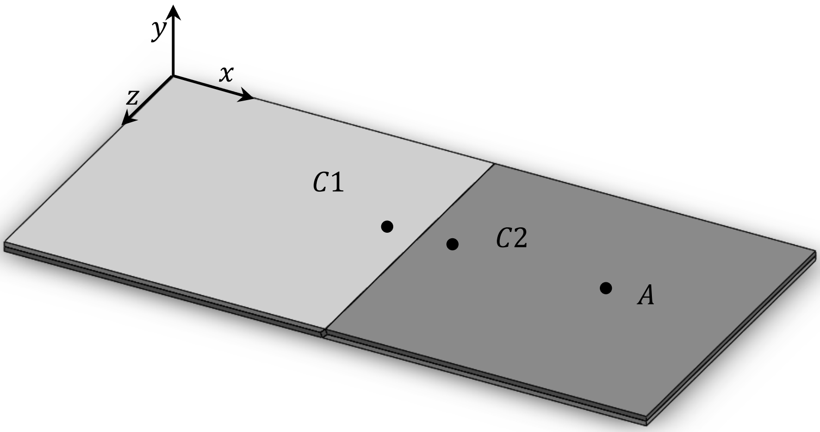

Figure 3.3 - Simplified geometry for the mesh convergence

The tests were performed applying a displacement (with a value of 0.2 mm) along the length of the ply boundary, and the results were evaluated in four different points of the geometry (see Figure 3.3). Table 3.3 presents the coordinates of the points were the results were evaluated.

Table 3.3 - Location of the evaluated points

point	$\boldsymbol{x(mm)}$	$\boldsymbol{y(mm)}$	$\boldsymbol{z(mm)}$
A	15.03	0.304	5
B	14.95	0.0	5
$C1$	8.79	0.304	5
$C2$	11.29	0.304	5

*Point B cannot be seen because it is on the hidden face of the ply.

From Figure 3.4 to Figure 3.7, the results of the analyses made are presented. In the horizontal axis is indicated the number of elements of each mesh, while principal vertical axis (the axis on the left) gives the stress values for each one of the different analyses and the secondary axis (right one) gives the time in seconds, representing the computational cost for *Brick 8 nodes* with full integration analyses.

Looking at the Figure 3.4, it is perceptible that when using *Brick 8 nodes* with full integration analyses and the *Brick 20 nodes* with reduced integration analyses, the solution converges when the number of elements reaches 4128, while using the *Brick 8 nodes* with reduced integration and the *Brick 20 nodes* with full integration, the solution needs 33024 elements to converge.

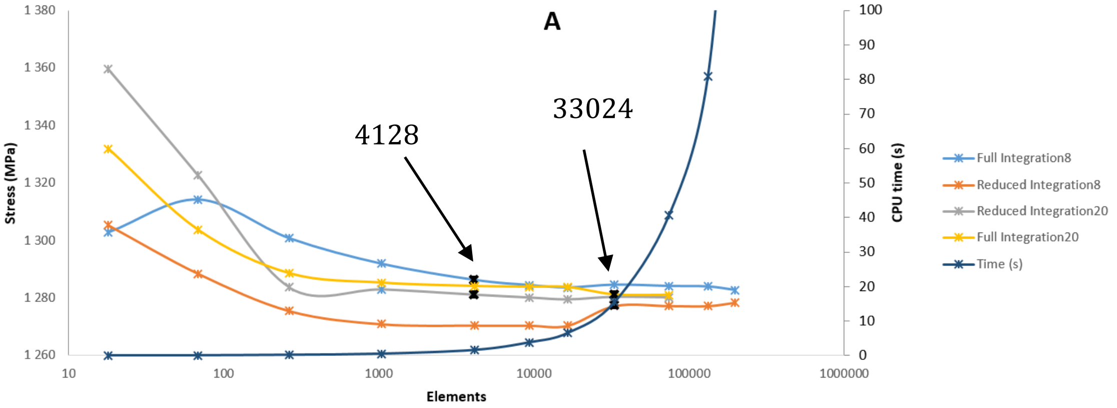

Figure 3.4 - Tension-number of elements for point A

The stress value at point B, computed with *Brick 8 nodes* with full integration converges similarly as the stress value in A. For *Brick 20 nodes* with reduced and full integration the same results converge since the 1040 elements, and just the *Brick 8 nodes* with reduced integration needs more elements to obtain a satisfactory result, which results in a too high computational cost, when compared with the computational cost of the other analysis.

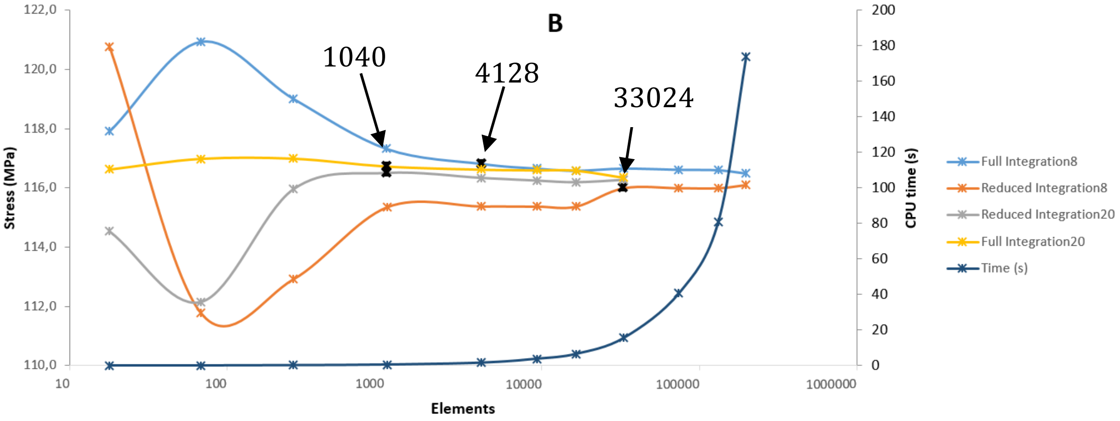

Figure 3.5 - Tension-number of elements for point B

In point C1, *Brick 20* nodes with reduced and full integration analysis converges at the same time, once again, and a satisfactory result is obtained when the number of elements reaches 4128. The analysis with *Brick 8 nodes* with full integration converges with 9264 elements, although the stress value for this point is almost the same as the stress value obtained with 4128 elements. As happens in the previous case, the *Brick 8 nodes* with reduced integration is not an option for this analysis, once the stress only converges after 33024 elements, increasing sharply the computational cost.

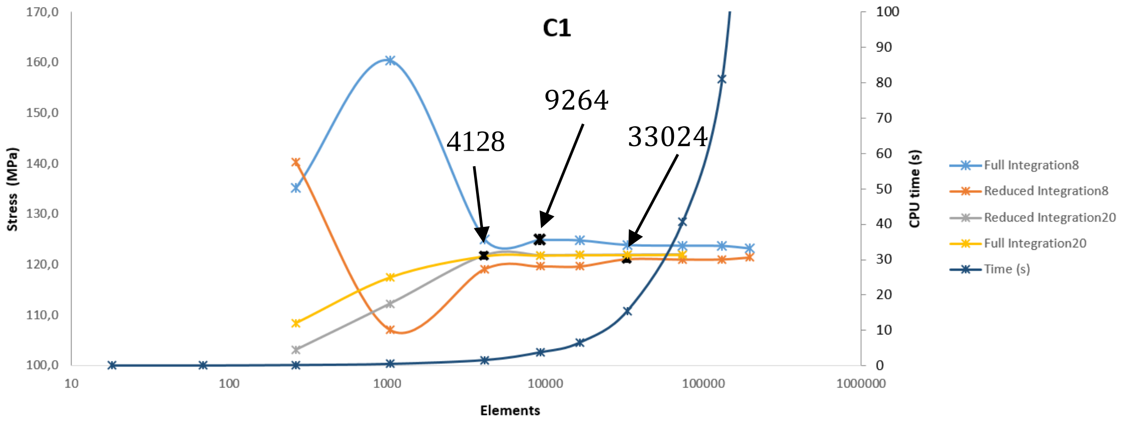

Figure 3.6 - Tension-number of elements for point C1

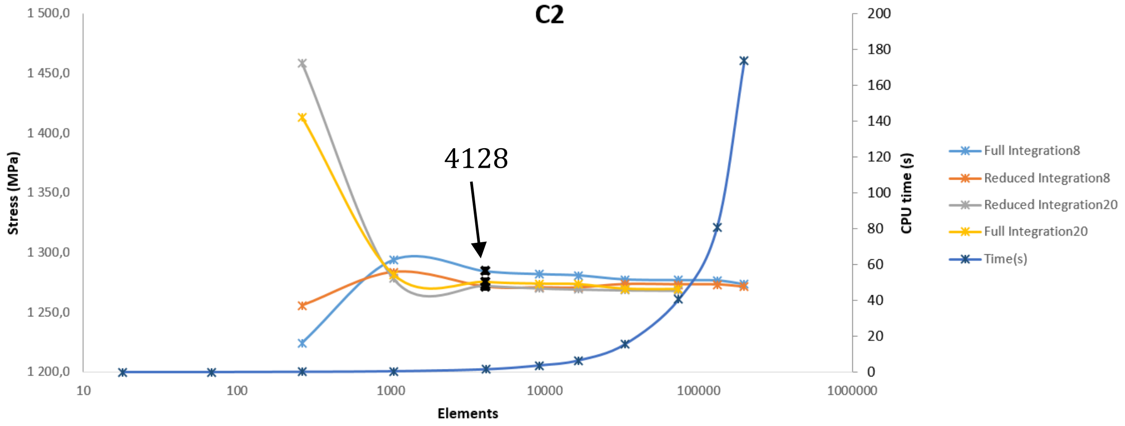

Figure 3.7 - Tension-number of elements for point C2

Finally, for the point C2, all the analysis converged and produce a very similar stresses with 4128 elements.

Evaluating all the results, it can be concluded that the *Brick 8 nodes*, with full integration, gives satisfactory results with an acceptable computational cost. This type of element produced converged results, for the four points, with meshes using 4128 elements. It can be seen that the *Brick 20 nodes*, with full integration in point B and C1, converge to the final result with less elements than the *Brick 8 nodes*, although the computational cost is about 4 times higher than the computational cost with *Brick 8 nodes*, as it can be seen the Figure 3.8.

Comparing the difference between full and reduced integration, it was observed that the computational cost does not have a significant reduction when the latter option is taken (when using the same elements number). Observing the results obtained at points A and B, the *Brick 8 nodes* with reduced integration needs much more elements to converge than the *Brick 8 nodes* with full integration, which increases significantly the computational cost. For example, at point A the *Brick 8 nodes* element with full integration converges after 4128 elements, which correspond to a computational cost of 1.622 seconds, while using the same element type with reduced integration, the analysis takes 13.41 seconds to get the same results. However, to run the analyses (*Brick 20 nodes* with reduced integration) with 4128 elements would take just 1.31 seconds. Here is quite evident the difference between full and reduced integration, once in reduced integration the analyses runs faster but the results can be less accurate.

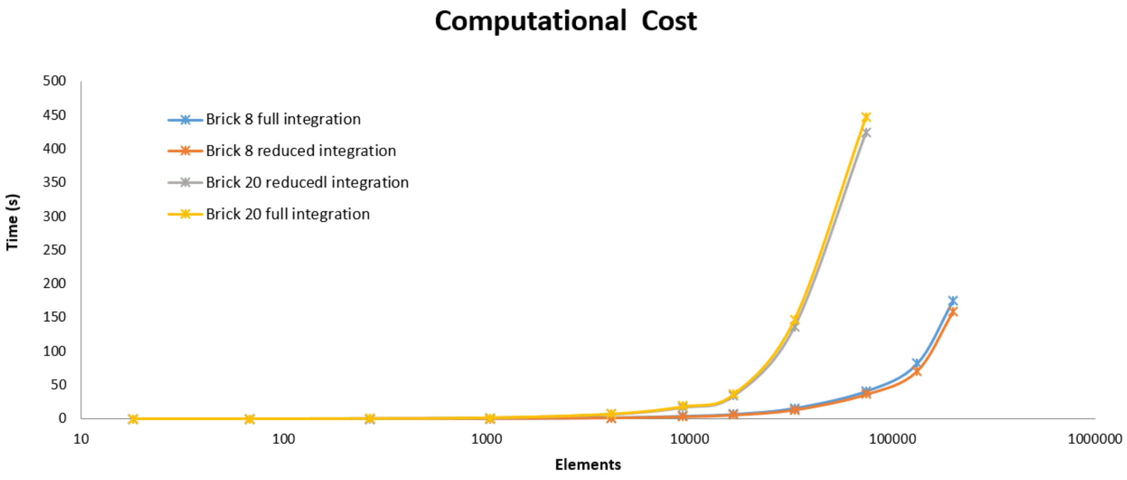

Figure 3.8 - Computational cost-number of elements

The question of the computational cost (Figure 3.8) is so important because an insignificant difference of a few seconds in the computational cost in this model with only one ply, can represent a difference of hours in the final model, which will contain 26 plies, with contacts and cohesive elements.

Since this latter model will require a considerable elements number and should be analyzed at a reasonable computational cost, the *Brick 8 nodes* element with full integration was the element type chosen. The minimum number of elements that should be used when considering the ply model is 4128, implying an element size of 0.3 mm. This is the element size that will be used for the remaining models of this dissertation.

3.3.Details of this first model

In order to complete this first ply model, the plasticity of the composite material and the delamination between different plies has to be considered.

The delamination of the material will be simulated using the cohesive elements that were implemented through the contact surfaces.

3.3.1. Shear and transverse compression plasticity

Plasticity in composite materials is a very sensitive subject, since it can be considered in meso-scale, but in macro-scale the plasticity is ignored once it is insignificant. In Chapter 2, was stated that there are five possible uniaxial tests to perform in a unidirectional lamina. The longitudinal tensile and longitudinal compression ($\pm\sigma_{11}$), transverse tensile and transverse compression ($\pm\sigma_{22}$) and pure shear (σ_{12}).

The inelastic behavior of composite material is a result of the micro-mechanical inelastic response of the constituents of the composite (matrix and fiber) [43]. Once it is assumed the material of this model has the same mechanical properties of a Hex-Ply® IM7-8552, the yield stresses in the different directions are the following [44]:

Table 3.4 - Yield stresses of Hex-ply IM7/8552 unidirectional laminates

$\sigma^y_{11_T}$ $[MPa]$	$\sigma^y_{11_C}$ $[MPa]$	$\sigma^y_{22_T}$ $[MPa]$	$\sigma^y_{22_C}$ $[MPa]$	σ^y_{12} $[MPa]$
2720	1690	64	64*	120

*Assuming that matrix presents an isotropic behavior

According to Bessa [18], from the five possible uniaxial test performed in a unidirectional lamina, only in two of them the material's behavior is non-linear: under transverse compression loads ($\sigma_{22} < 0$) or shear loads ($\sigma_{12} \neq 0$).

Koerber [21] tested IM7/8552 laminates to show the difference between dynamic and quasi-static non-linear response in of axis-compression test (with shear loads) and pure transverse compression test (with no shear loads). The results of the referred author are presented in Figure 3.9.

Observing Figure 3.9, it can be concluded that in the 90° pure transverse compression the behavior of the material is close to a linear behavior, despite this the results shows a non-linear behavior, so there is plasticity in pure transverse compression. From 75° to 45° off-axis compression, the non-linearity increases drastically as the angle of the fibers' orientation decreases. For the 45° to 15° off-axis compression, the response is close to the linear behavior. So, the behavior of a lamina subjected to shear loads is highly nonlinear, while the behavior of a lamina under transverse compressive loads is close to linear.

In this dissertation the plasticity of the material under transverse compressive loads ($\sigma_{22} < 0$) will not be consider but under shear load it will be consider. However, it should be noted that in this first model there is no plasticity, once the applied loads are tensile loads and there is no shear or transverse compression. The plasticity will not appear in the spread tow carbon fabric with 0º/90º arrangement, but it can be considered for other specimens subjected to shear loads as it will be shown in the Figure 4.26**Error! Reference source not found.** with the results of the experimental tests.

So the plasticity of the material under shear loads will be an option in the interface program developed in this dissertation.

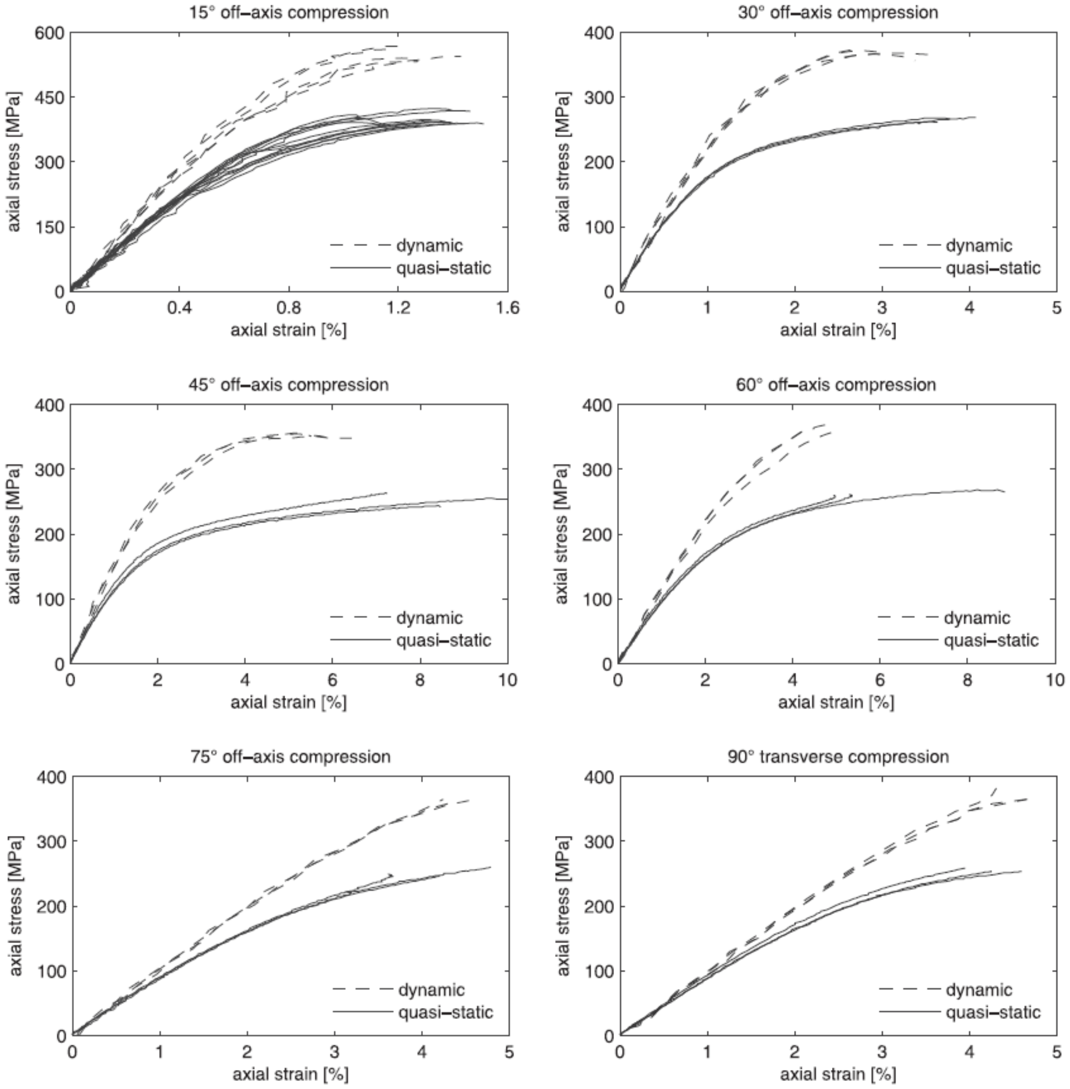

Figure 3.9 - Quasi-static and dynamic axial stress-strain responses from off-axis and transverse compression tests (for IM/8552 laminates) [21]

3.3.2. Delamination

Delamination has been considered the "Achilles heel" of laminated composite. This damage mode can be caused by impacts events, notches, manufacturing defects and stress concentrations caused by changes in structural detail [14].

Delamination generally develops because of excessive out-of-plane or interlaminar stresses being generated at the interfaces between adjacent plies. In short term, delamination can lead to a lack of support on the load bearing layers in a laminate, promoting damage growth and premature failure. In the longer term, delamination can lead to exposure of the load-bearing layers to environmental threats such as moisture or contaminant ingress [14].

This phenomenon can be simulated, numerically, using cohesive elements. These elements have the matrix properties of the composite material, in this case an epoxy matrix, and are implemented in the interface between unidirectional tows and in the interface of different plies.

For the cohesive elements (or interface elements), the interfacial separations is defined as the displacement jump, which represents the difference of the displacements of the adjacent interface surfaces [45]. Figure 3.10 presents a schematic of these cohesive elements.

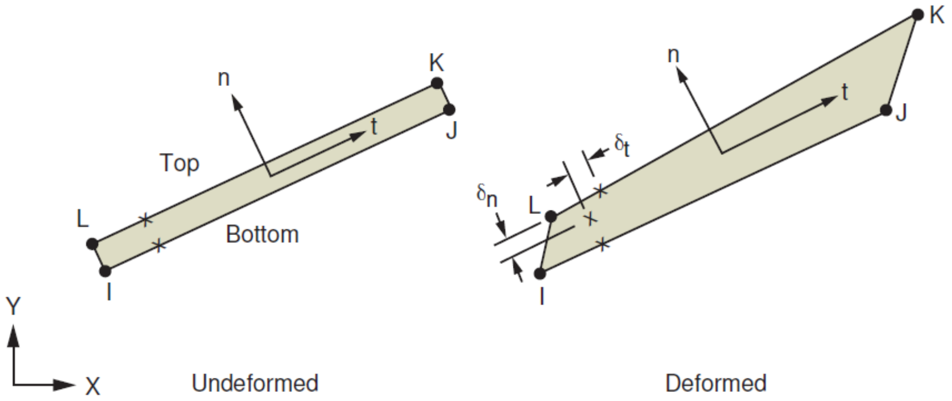

Figure 3.10 - "Schematic of interface elements" [45]

Figure 3.11 represents the bilinear behavior of the cohesive elements. It can be indentified an elastic path before the damage initiation, which intoduces a very high stifness to the interface before damage initiation [46]. The maximum normal contact stress is achieved at point A. The debonding begins at this point and it just finish at point C, when the normal contact stress reaches zero value [45]. Since the point C any further separation occurs without normal contact stress.

The area under the curve OAC represents the energy release and is called the crictical fracture energy (G_{IC}, G_{IIC} or G_{IIIC}, depending on the debonding mode) [45].

Here δ_n represents the normal contact gap (Mode I deboning), that is related with the normal critical energy fracture, G_{IC}. The behavior for tangential contact stress is similar to this one, but represents the mode II deboning, relating the tangential stress, τ, with the tangential displacement, δ_t^c.

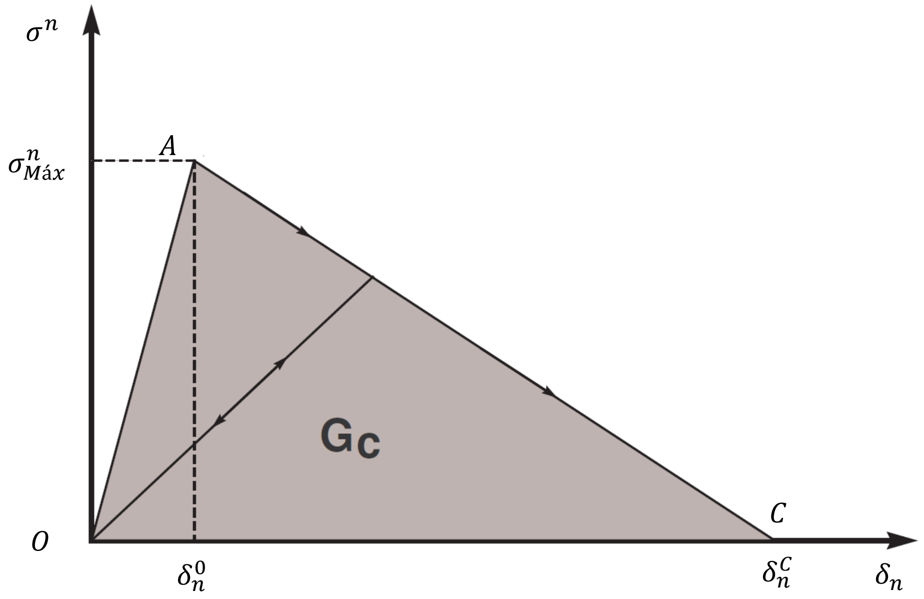

Figure 3.11 - "Normal contact stress and contact gap curve for bilinear cohesive zone material" [45],[18]

The cohesive zone material used, in this case, to simulate debonding (or delamination), with no contacts, has a bilinear material behavior used to simulate interface delamination and other fracture phenomena, which is defined by 4 material constants (regarding the fracture mode I and mode II) represented in Table 3.5.

Table 3.5 - Cohesive material properties for IM7-8552 [38], [47]

$\boldsymbol{\sigma^n_{Máx}}$ $[\boldsymbol{MPa}]$	$\boldsymbol{\delta^c_n}$ $[\boldsymbol{m}]$	$\boldsymbol{\tau_{Máx}}$ $[\boldsymbol{MPa}]$	$\boldsymbol{\delta^c_t}$ $[\boldsymbol{m}]$
60	$5.93e^{-6}$	90	$2.15e^{-5}$

* $\sigma_{Máx}$ – Maximum normal stress;

δ^c_n – Normal displacement jump at the completion of deboning;

$\tau_{Máx}$ – Maximum tangential stress;

δ^c_t – Tangential displacement jump at the completion of deboning;

The normal and tangential displacement at the completion of the deboning were obtained by the use of the following equations [47]:

$$\delta^c_n = \frac{2G_{IC}}{\sigma^n_{Máx}} \tag{58}$$

$$\delta^c_t = \frac{2G_{IIC}}{\tau_{Máx}} \tag{59}$$

With $G_{IC} = 178\ N/m$ and $G_{IIC} = 970\ N/m$. These values were provided by Jiménez work [48].

In order to test the cohesive elements a simulation was performed with a simplified geometry with two unidirectional plies, with a linear elastic orthotropic material behavior (with the mechanical properties presented in Table 3.2). To make this simulation the cohesive elements were implemented in the intermediate interface between the two unidirectional plies. Two opposite displacements were applied, in yy direction, at one of the end surfaces, while the opposite surface was completely constrained, in order to understand how the cohesive elements are working and if they can simulate the delamination with the properties defined in Table 3.5.

The boundary conditions applied to the model and the results of the simulation are presented in Figure 3.12 and Figure 3.13, respectively.

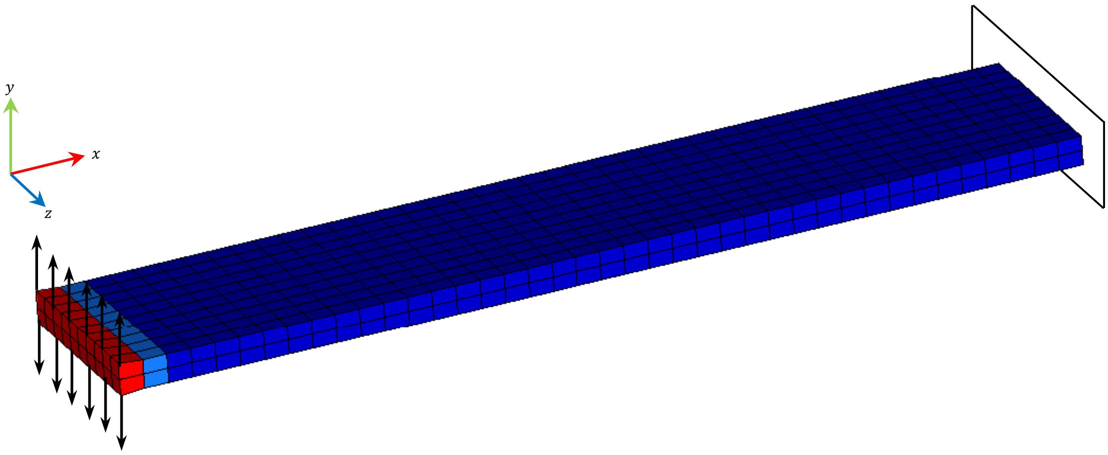

Figure 3.12 - Boundary conditions used to test the cohesive elements implemented without contacts

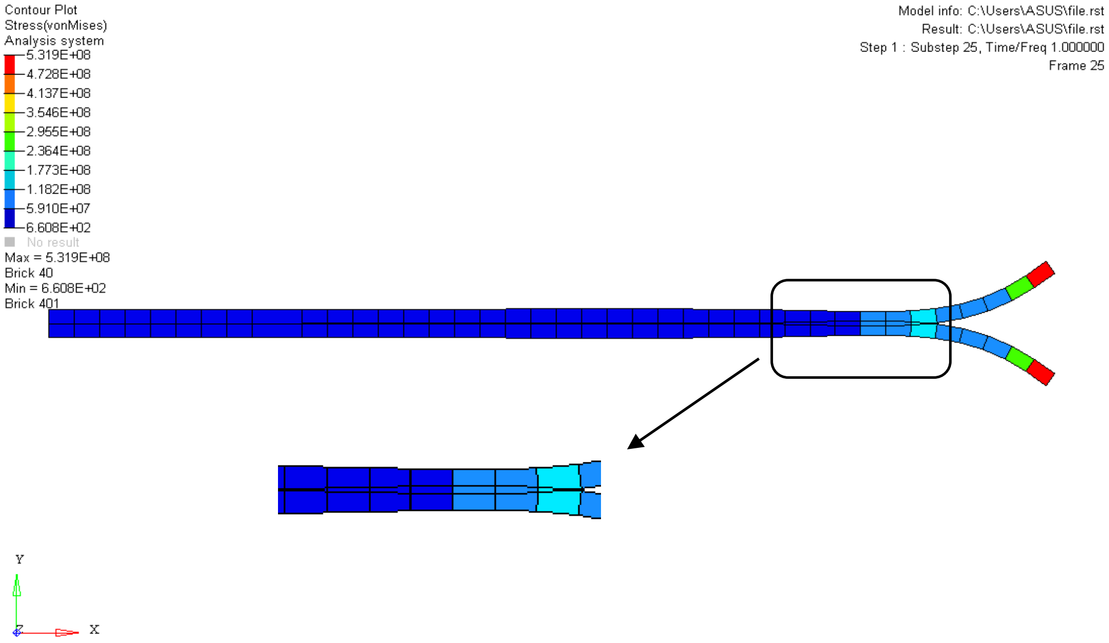
Contour Plot
Stress(vonMises)
Analysis system
5.319E+08
4.728E+08
4.137E+08
3.546E+08
2.955E+08
2.364E+08
1.773E+08
1.182E+08
5.910E+07
6.608E+02
No result
Max = 5.319E+08
Brick 40
Min = 6.608E+02
Brick 401
Model info: C:\Users\ASUS\file.rst
Result: C:\Users\ASUS\file.rst
Step 1 : Substep 25, Time/Freq 1.000000
Frame 25
Y
X

Figure 3.13 - Final results of the delamination test (with cohesive elements without contacts)

As it can be seen in the Figure 3.13, there is a volume interference between the different unidirectional plies. It was tested and concluded that this was not a graphical problem and it is necessary the use of contact elements to avoid this effect.

Contact problems [49] are highly non-linear and need significant computer resources to be solved. Contact elements are used to model surfaces that are in contact and transmit forces to each other, not allowing the interpenetration that was visible during the simulation of the delamination tests without contact elements, presented in the Figure 3.13.

To simulate the model with cohesive elements and contacts, it was used a surface-to-surface contact model, which is a contact defined between two different surfaces. Here, the contact will connect the nodes of one surface to the faces of the other surface (and vice-versa) [50].

Ansys software has an interface delamination model developed to simulate delamination using contact elements suporting a cohesive zone material model with bilinear behaviour. This model is defined by the use of the maximum stresses and critical fracture energies densities, presented in Table 3.6:

Table 3.6 - Cohesive material properties, with critical energies density, for IM7-8552 [38], [48], [49].

$\boldsymbol{\sigma^{n}_{Máx}}$ $[\boldsymbol{MPa}]$	$\boldsymbol{G_I}$ $[\boldsymbol{J/m^2}]$	$\boldsymbol{\tau_{Máx}}$ $[\boldsymbol{MPa}]$	$\boldsymbol{G_{II}}$ $[\boldsymbol{J/m^2}]$	$\boldsymbol{\eta}$
60	178.332	90	970.851	1.45

* $\sigma_{Máx}$ – Maximum normal contact stress;

G_I – Critical fracture energy density (energy/area) for normal separation;

$\tau_{Máx}$ – Maximum equivalent tangential contact stress;

G_{II} – Critical fracture energy density (energy/area) for tangential slip;

η – Artificial damping coefficient;

To simulate the delamination with contacts and cohesive elements it was used the same model with the same boundary conditions presented in Figure 3.12. The only difference between the two models is that the first one does not have contacts, therefore it is visible a volume interference, while the second one does not allow this interference to occur. The results of this simulation can be seen in the Figure 3.14.

In this simple model, the contacts and the cohesive elements were implemented in the intermediate interface between the two unidirectional plies. Although in the compressive specimen model the contact and cohesive elements are implemented not only between different plies but also between each spread tow.

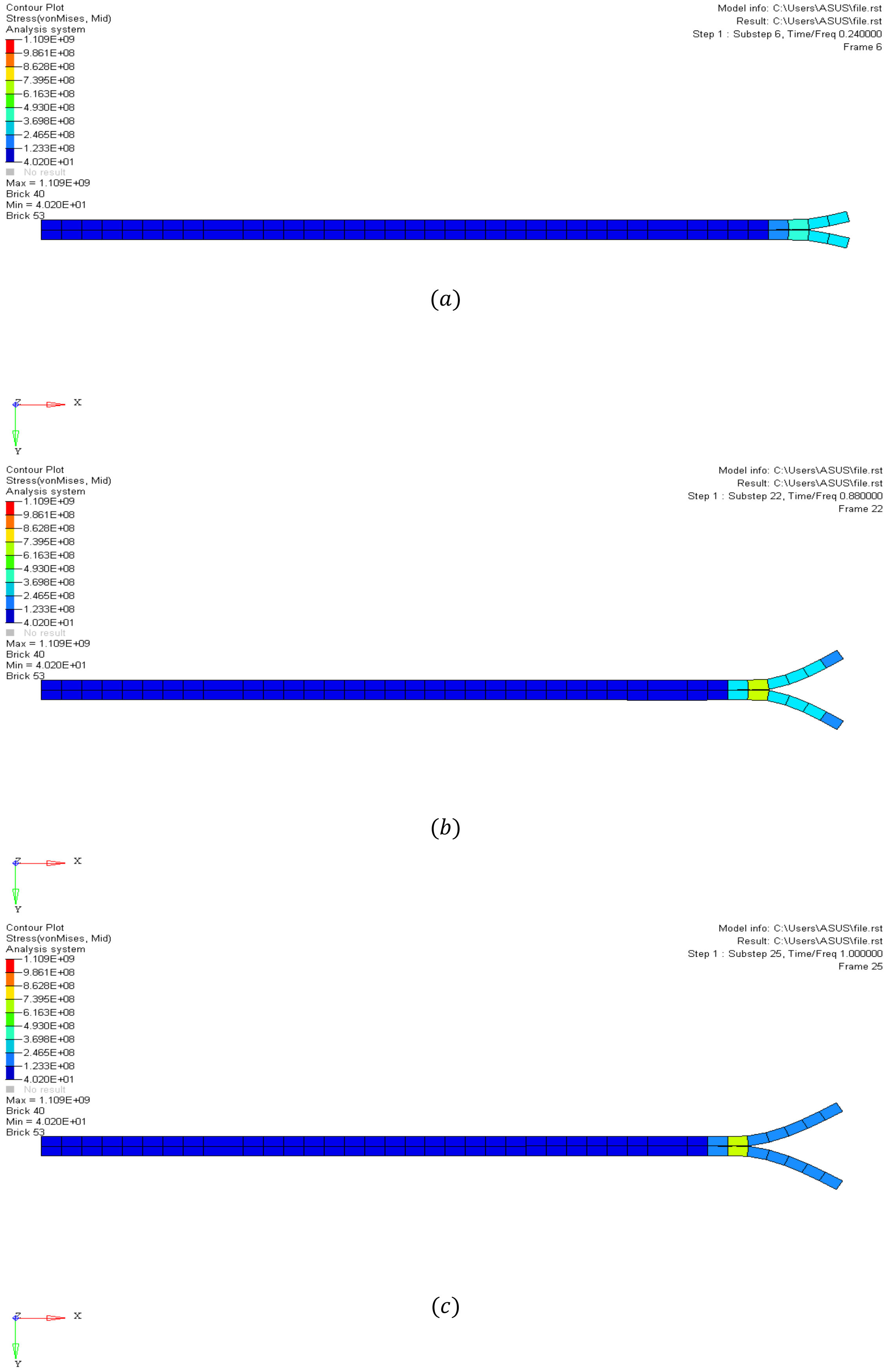

Figure 3.14 - Results of the delamination test with contact and cohesive elements for substep: (a) 6, (b) 22 and (c) 25

As it was expected, during the second delamination test (with contacts), interpenetrations are not presented between the different volumes due to the contacts defined in the intermediate surfaces. Once the contact is activated, the surfaces apply forces to each other, not allowing the interpenetration.

Comparing the results of both simulations of the delamination phenomena it can be concluded that they are quite similar. Both models, with and without contacts, present the same crack extension as seen in Figure 3.13 and Figure 3.14.

Looking at the stress results for the first simulation, with only cohesive elements, the stress (Von Mises) value of the first elements that do not delaminate is around $200\ MPa$, while for de second simulation the elements present a stress (Von Mises) value around $600\ MPa$. The results are in same order of magnitude and the difference presented can be explained by the use of the contacts, which avoid the interpenetration of the volumes, thus increasing the stress value in this area.

Another difference, is the stress distribution. Note that for the delamination test with contacts, the stress (Von Mises) value is uniform in the elements belonging to the delaminated area and it is around the $250\ MPa$. Whereas, in the first delamination test, the stress (Von Mises) values of the correspondent elements are not uniform and oscillate from $100\ MPa$ to $500\ MPa$.

3.4.Combined failure criterion

The failure criteria are used to predict the stress values for which the material fails under the action of external loads. These criteria use the failure stress values provided by the 5 uniaxial tests that are possible to perform in carbon fiber reinforced plastic, longitudinal tension and compression (X_T and X_C, respectively), transverse tension and compression (Y_T and Y_C, respectively), and pure shear (S_L).

The numerical models implemented in this dissertation have the carbon fibers oriented in a 0°/90° arrangement, so the maximum stress failure criterion could be enough to simulate the material's failure, once this criterion evaluates the stress values along the principal directions. This criterion is simple, it reports that the failure occurs when a principal stress exceeds a specific value. However, one of the main goals of this dissertation is the development of a methodology capable to predict the behavior of different specimens (with different layups) under various type of loads, so the Tsai-Wu failure criterion will be used in order to take into account other directions besides the principal directions. This criterion was chosen because it is one of the most used criterions, in aeronautical industry, to predict material failure.

Tsai-Wu failure criterion is extensively used in determining the damage initiation of a ply, but nevertheless has some drawbacks. One of them is the fact the failure stress of fiber in a lamina exceeds the strength of the material for the case of symmetric angle-ply laminates with small fiber angles subjected to off-axis tension (which is not the case, but it can be in other models) [51].

So, in order to eliminate the drawbacks of both models, it was decided use a combination of failure criteria with maximum stress and Tsai-Wu failure criteria.

This combined failure criterion, for the plane stress condition, can be written as [51]:

$$\begin{gathered} X_C < \sigma_{11} < X_T \\ Y_C < \sigma_{22} < Y_T \end{gathered} \tag{60}$$

and

$$f_1\sigma_{11} + f_2\sigma_{22} + F_{11}\sigma_{11}^2 + F_{22}\sigma_{22}^2 + F_{66}\sigma_{12}^2 < 1 \tag{61}$$

In Figure 3.15 is represented the stress state permissible area, of the material, with this mix between maximum stress failure (represented in black) and Tsai-Wu failure criteria (represented in blue).

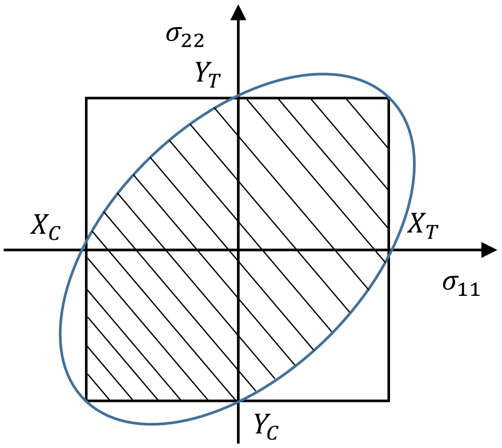

Figure 3.15 - Comparison between Tsai-Wu a maximum stress failure criteria

3.5. Incremental-iterative analysis

After the implementation of the first model and once chosen the element type and size, the full integration analysis, defined contacts, cohesive elements and failure criterion, it was necessary to test the damage propagation in composite material, using proposed combined failure criterion, described above.

For this, was develop an interface program between Ansys and MatLab softwares which gradually increases the displacement at the same time that stress tensor is evaluated in each element. It is then possible to evaluate if each one of the elements fails or not according to the failure criterion. If any element fails, its stiffness is reduced by multiplying the initial value by 10^{-6}, thus simulating the element's failure.

This program constitutes a methodology developed during the course of this dissertation and is capable of modeling specimens with different geometries, different lay-ups and under various types of loads. Once the necessary parameters to implement a meso-scale model, such as, geometries of the specimen, dimensions, ply number, initial displacement, increment value or maximum number of analysis are set, the non-linear analysis proceeds automatically.

In this methodology all the initial parameters, failure criterion, mechanical properties, mesh type and size, boundary conditions, solution option, etc… are defined in the MatLab software, while Ansys software is only used to run the analysis (used as a solver) and export the results, in this case the stress tensor values with respect to the global coordinate system. These results are used by MatLab, which finds the elements that failed according to the failure criterion.

Figure 3.16 describes the flow-chart of an incremental-iterative analysis using Ansys and MatLab, giving a better perception of the algorithm used to simulate the damage propagation.

In the beginning of the program the initial parameters are defined, such as the maximum displacement, Δx_{Max}, the initial displacement, D, the increment on the displacement in each analysis, Δx, and it is also initialized the analysis number, a. Before this, the model is already set with the right geometry, dimensions, number of plies, maximum number of analysis, material properties, mesh size, boundary conditions or solution options.

After this, Ansys software analyzes the model and if the solution converged, which means that the program could finish the analysis and the results of the stress in each element were written in a ".txt" file, the stress results can be evaluated with the proposed combined failure criterion (previously mentioned, a combined failure criterion between maximum stress and Tsai-Wu failure criteria). When an element fails according to the proposed failure criterion, the EKILL function, from Ansys software, is activated to reduce drastically the material's stiffness of that element, multiplying it by 10^{-6}. Whenever any element fails in an analysis, the displacement in the next analysis (the analysis where the element's stiffness will be reduced) is not incremented because of the stress redistribution, since after the first elements failure more elements will fail. In fact, it is verified that, when any element fails, the stresses that it supports need to be redistributed to other elements that did not fail yet, which will increase the stress values in these elements and can lead to more elements failure. If the displacement were simultaneously increased, the amount of failed elements could lead to non-convergence of the solution. So, the prescribed displacement only increases when no more element fails according to the failure criterion, in the previous analysis.

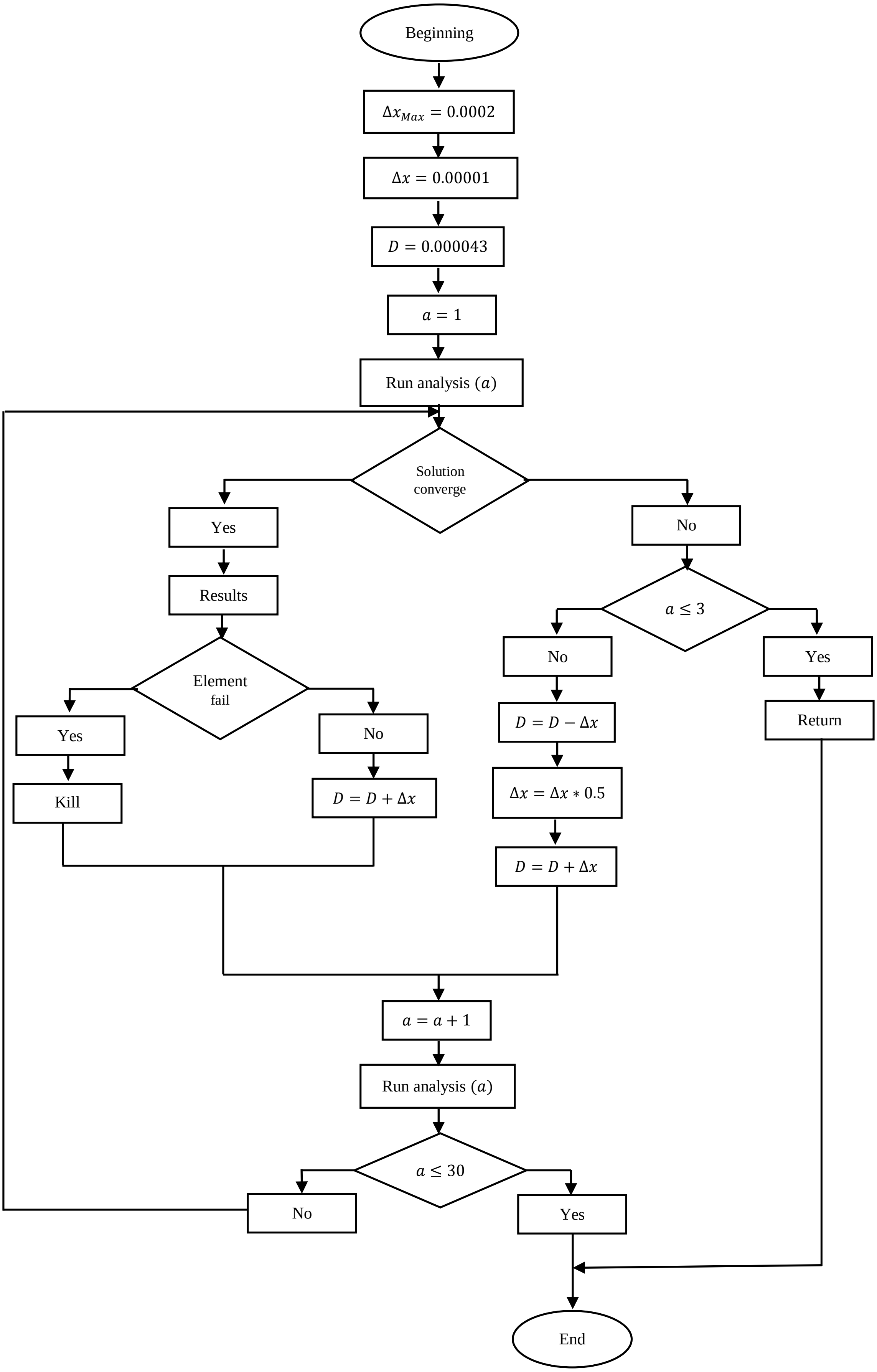
Beginning
$\Delta x_{Max} = 0.0002$
$\Delta x = 0.00001$
$D = 0.000043$
$a = 1$
Run analysis (a)
Solution converge
Yes
Results
Element fail
Yes
Kill
No
$D = D + \Delta x$
No
$a \leq 3$
No
$D = D - \Delta x$
$\Delta x = \Delta x * 0.5$
$D = D + \Delta x$
Yes
Return
$a = a + 1$
Run analysis (a)
$a \leq 30$
No
Yes
End

Figure 3.16 - Incremental-iterative analysis for one ply under tensile loads (units of the initial parameters in m).

After this, the previous analysis restarts with increased prescribed displacement or with more failed elements. This just happens if the analysis/iterations number were less than the number defined in the beginning (it was defined to be 30, in this case, as shown in Figure 3.16), if not the incremental-iterative program finish.

If the solution of any analysis does not converge it is necessary to know in which iteration this occurs. If it is at the beginning, one of the first three analysis, it means the initial parameters should be reviewed and the analysis stops. If more than 3 successfully iterations were already performed, and the last solution diverges, this iteration is ignored, returning to the displacement value used in the previous iteration and the value of increment is halved in order to get a shorter displacement and find less elements that fail. This can make the solution of the new analysis convergent.

The program's cycle only finishes by two ways: if the solution of any of the first three iterations does not converge or if the number of increments reaches the number defined in the program (maximum number of analysis).

The main reason why there is a great difficulty in the convergence of the solutions is the use of contacts, since there is always contacts being activated and deactivated during the course of the analysis.

3.6. Results

After the implementation of the first model of one ply with contacts and cohesive elements and defined the failure criterion, an incremental iterative analysis was performed, as described above, with the aim of simulating the damage propagation on the material.

This model was tested under tension loads, and no compression loads (as the real specimen tested experimentally), because in the case of only one ply, a compression load would introduce some instability and bending could occur. This would lead to inconclusive results.

For this model, the constants provided from the five uniaxial test (tension and compression in the fiber directions, tension and compression in the transversal direction and pure shear) are taken from [17] and shown in Table 3.7:

Table 3.7 - Unidirectional constants of the uniaxial tests used in the simulation of one ply under tension loads[17]

X_T $[MPa]$	X_C $[MPa]$	Y_T $[MPa]$	Y_C $[MPa]$	S_L $[MPa]$
2323.5 500*	1200.1 350*	62.3	199.8	92.3

*these values were modified in order to see the damage initiation, once the stress values taken from Maimi's PhD thesis were not reached for the imposed displacement.

The values in Table 3.7 had to be adapted because these values are unknown for the composite material used in this dissertation.

It should be noted that the results obtained for this ply model, presented in the Figure 3.18-Figure 3.22, cannot be compared with experimental results, and so they are merely qualitative. Its purpose is to know where the area of greatest stress concentration is, and how the failure propagates.

The boundary conditions applied in this first simulation are presented in the Figure 3.17 and consists of one fixed end, while in the other a displacement of 0.2 mm is imposed. To avoid the rotation of the ply, it was fixed the upper face in the yy direction.

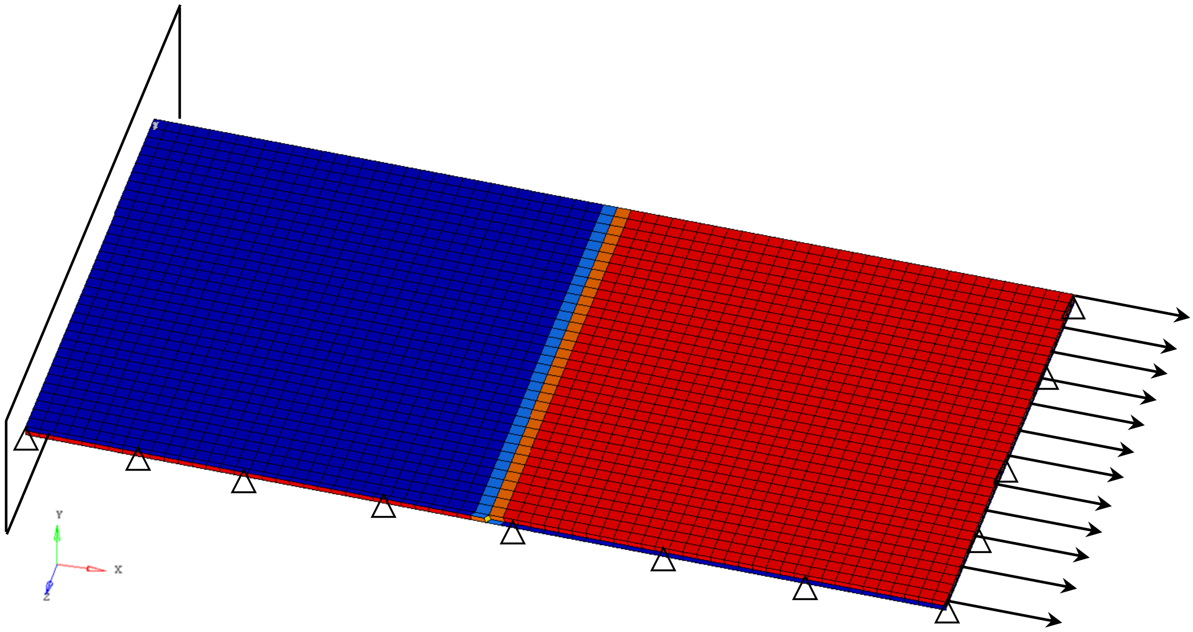

Figure 3.17 - Boundary conditions applied to the ply model

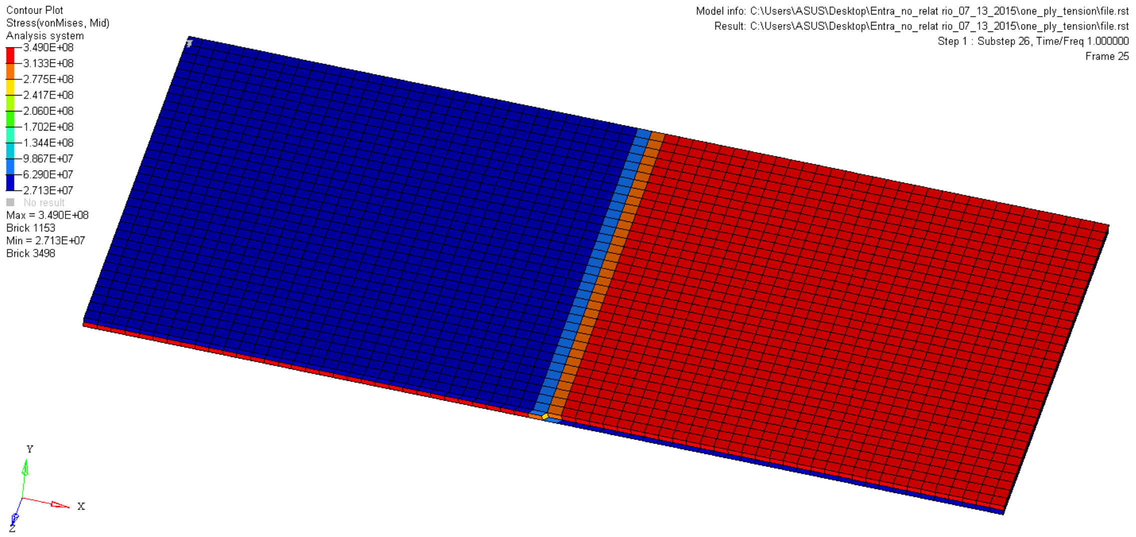

Figure 3.18 - Equivalent Von-Mises Stress Analysis at step 1

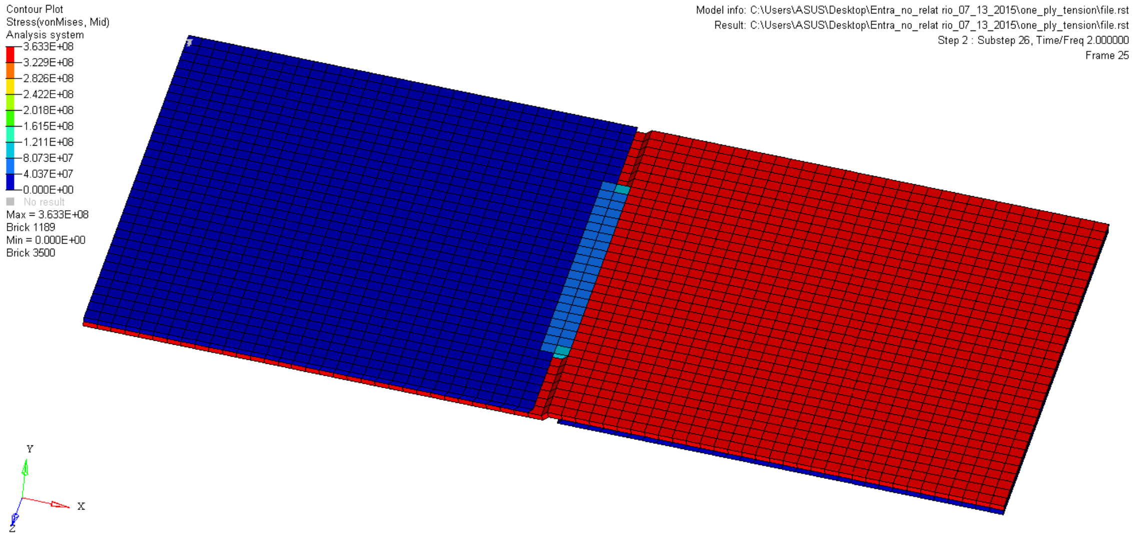
Contour Plot
Stress(vonMises, Mid)
Analysis system
3.633E+08
3.229E+08
2.826E+08
2.422E+08
2.018E+08
1.615E+08
1.211E+08
8.073E+07
4.037E+07
0.000E+00
No result
Max = 3.633E+08
Brick 1189
Min = 0.000E+00
Brick 3500
Model info: C:\Users\ASUS\Desktop\Entra_no_relat rio_07_13_2015\one_ply_tension\file.rst
Result: C:\Users\ASUS\Desktop\Entra_no_relat rio_07_13_2015\one_ply_tension\file.rst
Step 2 : Substep 26, Time/Freq 2.000000
Frame 25
Y
X
Z

Figure 3.19 - Equivalent Von-Mises Stress Analysis at step 2

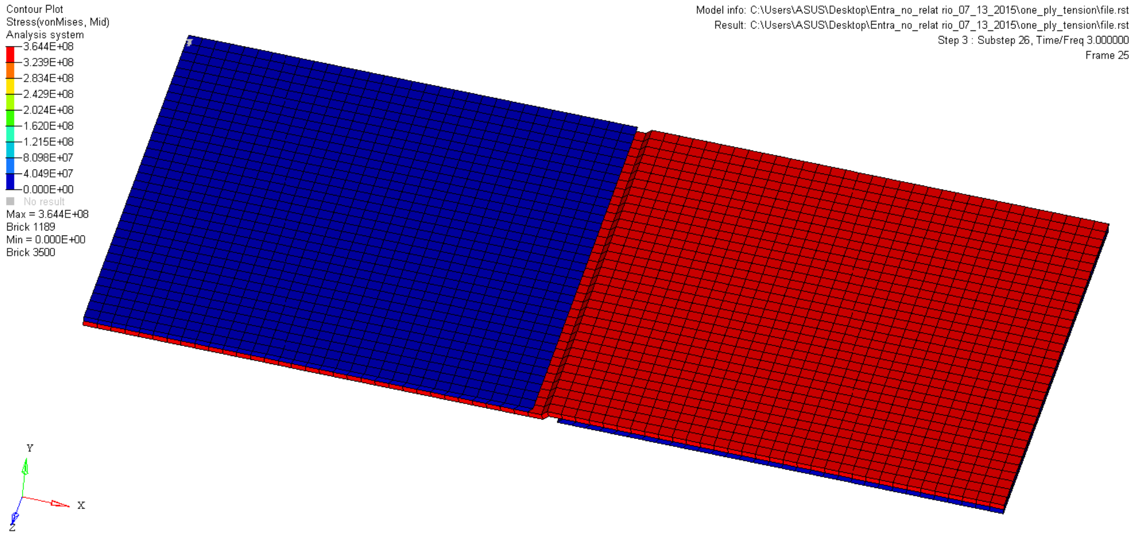
Contour Plot
Stress(vonMises, Mid)
Analysis system
3.644E+08
3.239E+08
2.834E+08
2.429E+08
2.024E+08
1.620E+08
1.215E+08
8.098E+07
4.049E+07
0.000E+00
No result
Max = 3.644E+08
Brick 1189
Min = 0.000E+00
Brick 3500
Model info: C:\Users\ASUS\Desktop\Entra_no_relat rio_07_13_2015\one_ply_tension\file.rst
Result: C:\Users\ASUS\Desktop\Entra_no_relat rio_07_13_2015\one_ply_tension\file.rst
Step 3 : Substep 26, Time/Freq 3.000000
Frame 25
Y
X
Z

Figure 3.20 - Equivalent Von-Mises Stress Analysis at step 3

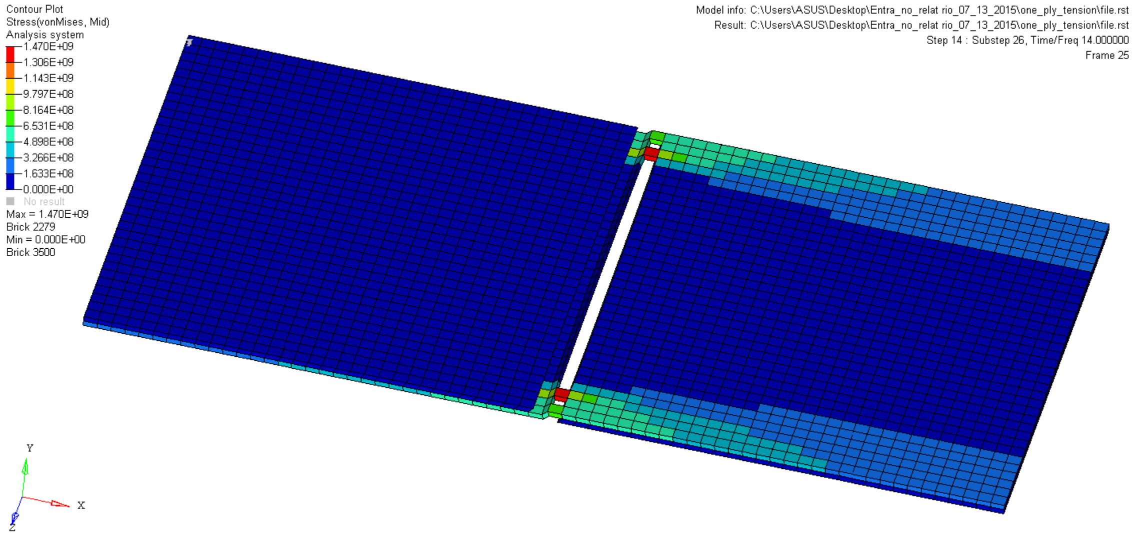
Contour Plot
Stress(vonMises, Mid)
Analysis system
1.470E+09
1.306E+09
1.143E+09
9.797E+08
8.164E+08
6.531E+08
4.898E+08
3.266E+08
1.633E+08
0.000E+00
No result
Max = 1.470E+09
Brick 2279
Min = 0.000E+00
Brick 3500
Model info: C:\Users\ASUS\Desktop\Entra_no_relat rio_07_13_2015\one_ply_tension\file.rst
Result: C:\Users\ASUS\Desktop\Entra_no_relat rio_07_13_2015\one_ply_tension\file.rst
Step 14 : Substep 26, Time/Freq 14.000000
Frame 25
Y
X
Z

Figure 3.21 - Equivalent Von-Mises Stress Analysis at step 14

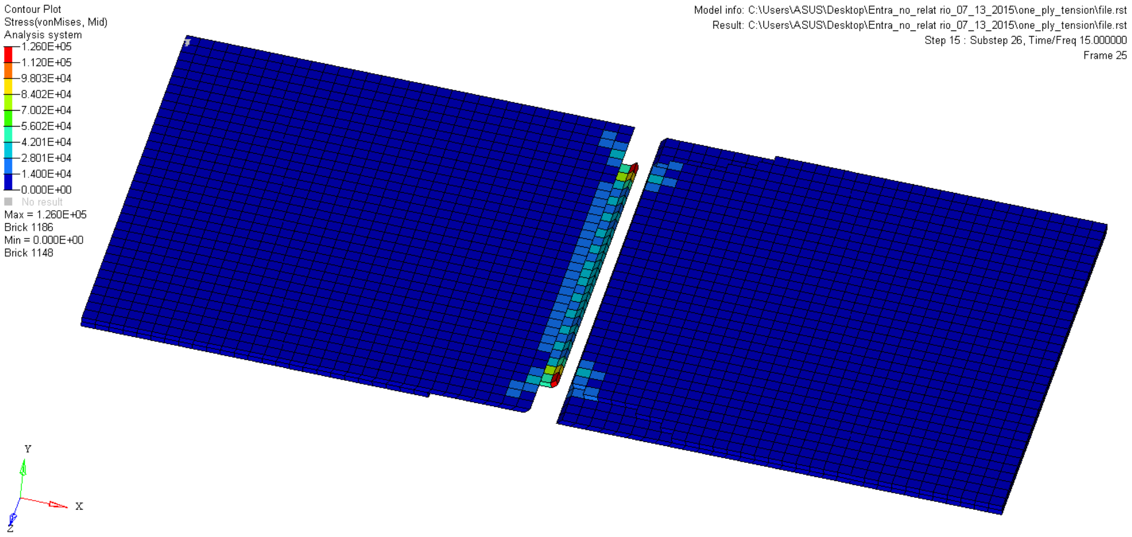
Contour Plot
Stress(vonMises, Mid)
Analysis system
1.260E+05
1.120E+05
9.803E+04
8.402E+04
7.002E+04
5.602E+04
4.201E+04
2.801E+04
1.400E+04
0.000E+00
No result
Max = 1.260E+05
Brick 1186
Min = 0.000E+00
Brick 1148
Model info: C:\Users\ASUS\Desktop\Entra_no_relat rio_07_13_2015\one_ply_tension\file.rst
Result: C:\Users\ASUS\Desktop\Entra_no_relat rio_07_13_2015\one_ply_tension\file.rst
Step 15 : Substep 26, Time/Freq 15.000000
Frame 25
Y
X
Z

Figure 3.22 - Equivalent Von-Mises Stress Analysis at step 15

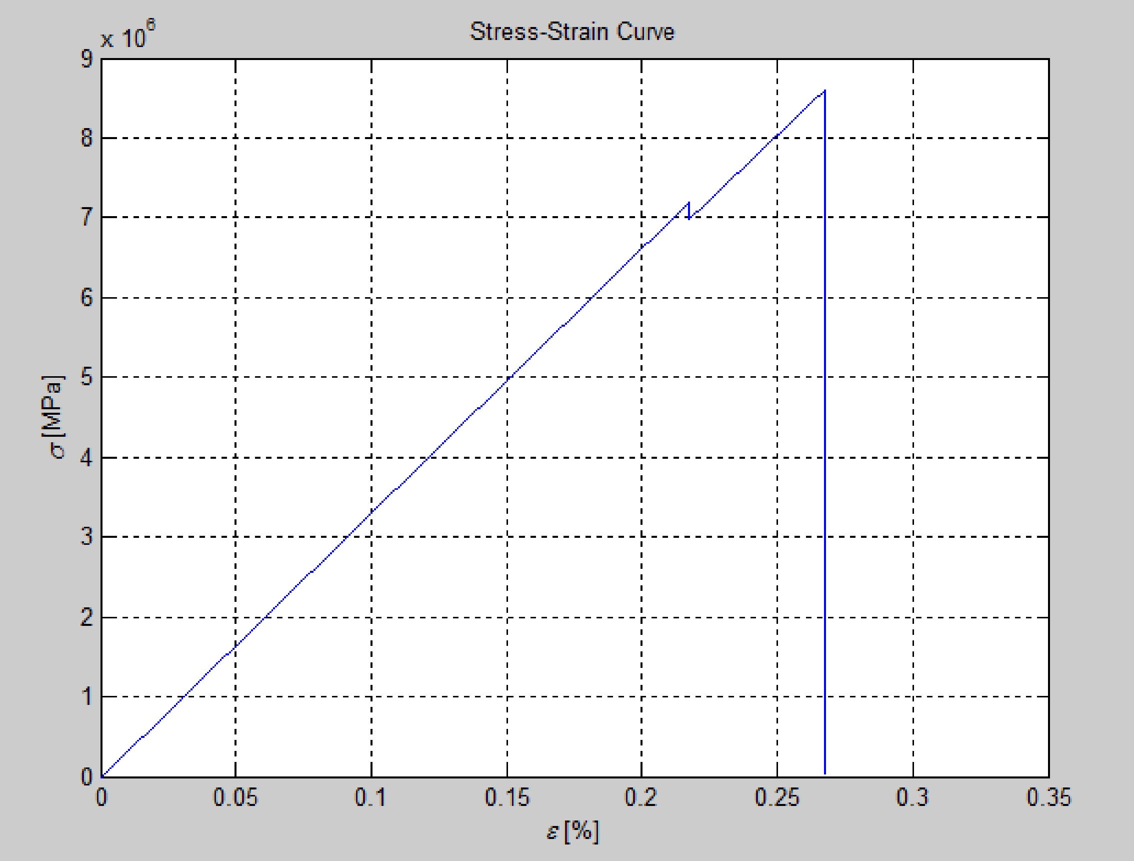

Figure 3.23 - Stress-Strain results of the simulation of the ply model under tension loads

The results revealed a uniformity in Von-Mises stresses along the *zz* axis as it was expect due to the symmetry of the geometry and the boundary conditions in this direction. So, when there are some elements failing in the same iteration, probably most of them have the same coordinate in the *zz* direction, but not all.

Another event that should be noted is that the first elements to fail are the elements with fibers aligned with the zz direction (90° with xx direction) close to change of cell, which is the zone where the spread tow with the fibers aligned at 90° crosses the spread tow with the fibers aligned at 0°. This was not expected (matrix failure before fiber failure) and has to do with the unidirectional constants taken from the uniaxial tests defined in the Table 3.7 and the cohesive properties presented in the Table 3.6.

The stress limit in the fibers' transversal direction under tension loads is $62.3\ MPa$, while the stress limit for the fibers' longitudinal direction is $500\ MPa$. This is a considerable difference and is the main reason for the elements whose fibers are aligned transversally to the applied loads failing first than the others. This is also due to the cohesive elements' properties, because if the material delaminates before the elements reach the ultimate stress value, these elements would not fail. So, this could be a sign that the cohesive properties need to be adjusted in this model, once in the experimented tests, delamination was observed, and in this ply model this is not observed.

Figure 3.23 presents the stress-strain diagram obtained from this simulation. This was the expected behavior of the material, given there is no plasticity implemented in this model. Observing this curve, it can be seen a drop in the stress value at a strain around the 0.22%, which happens due to the failure of the first elements (presented in the Figure 3.19 and Figure 3.20) close to the change of cell.

After the failure of the first elements, the model's failure does not happen and the stress continues to be incremented until the failure of the fibers aligned at 0°. With the failure of these elements (presented in Figure 3.21 and Figure 3.22), the simulation ends.

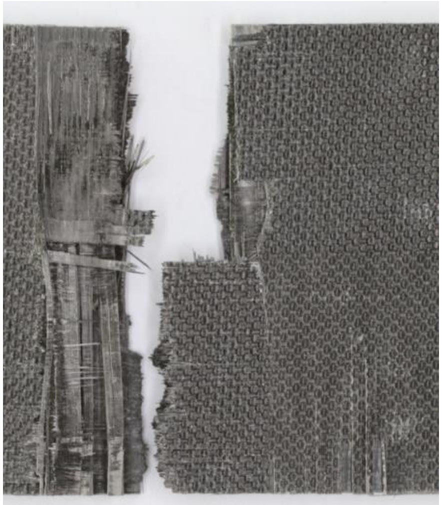

Figure 3.24 - Spread tow carbon fabric specimen after a tension test

It was expected the failure to occur in the area of the change of cell, since this is the area with the greatest stress concentration and because this was verified in some experimental tension tests (presented in the Figure 3.24), with the same material used in the models presented in this dissertation.

With these results, it can be concluded that the developed methodology is efficient for the ply model, showing consistent results as expected.

Chapter 4.

Numerical model of a specimen

After implementation and analysis of the first ply model, it was necessary to model the entire compression test specimen. For this, there were some keypoints to take into account. First, the plies are spread tow carbon fabric instead of unidirectional plies, which increases the degree of difficulty to implement the model. Then, the change of cell cannot match all the same orderly because the layup of the experimental specimens was not controlled except the fibers orientation, which were a 0º/90º arrangement for these specimens.

To generate the geometry, it was created an automatic program (described in the Chapter 3) using the interface between MatLab software and Ansys software that can generate the whole geometry with a random layup, as it can be seen in Figure 4.1, the changes of cell can appear anywhere along the length of the specimen.

As described in Chapter 3, in this program can be defined a high number of parameters of the model, such as the element size, number of plies or the displacement value applied to the model.

The compressive specimen has the dimensions presented in Table 4.1 and the geometry is represented in Figure 4.1 (this figure represents one of the possible geometries, once the layup is generated randomly for each model, however the overall dimensions does not change).

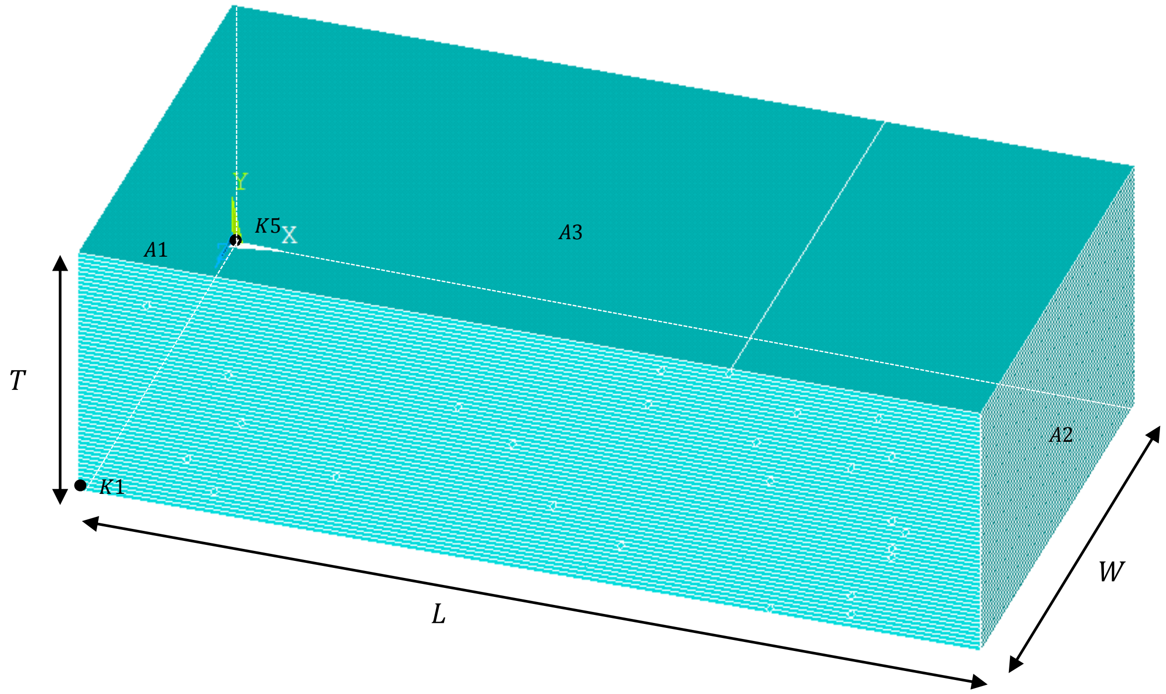

Figure 4.1 - Geometry of the compressive specimen

Table 4.1 - Dimensions of the compressive specimen

L [**mm**]	**T** [**mm**]	**W** [**mm**]	**Plies number**	**Fibers orientation** [°]
19.998	5.883	10.269	26	0º/90º

4.1.Boundary conditions

After the implementation of the model, many analysis were made with different boundary conditions in order to achieve a specimen’s final appearance similar to the specimens tested experimentally. In this analysis the kill element function was not used yet because the cohesive element properties need to be adjusted so that the failure modes can be identified.

The specimens were also tested with different boundary conditions in order to find the one that better corresponds to reality. In the Figure 4.2 to Figure 4.5 will be represented some of those analysis with different boundary conditions applied and its final result. Once again, the main goal was to find the boundary conditions, the material and interface properties that allow a final appearance of the specimens similar to those tested experimentally, not taking into account the stress results yet.

In the first compression test carried out, the material properties used are presented in the Table 4.2, the cohesive material properties are the same previously presented in Table 3.6 and the boundary conditions are described in Table 4.4. The results of this simulation are presented in Figure 4.2.

Table 4.2 - Elastic properties of IM7/8552 unidirectional laminates, for compression loads [38].

E_{11} $[GPa]$	E_{22} $[GPa]$	E_{33} $[GPa]$	v_{12}	v_{23}	v_{13}	G_{12} $[MPa]$	G_{23} $[MPa]$	G_{13} $[MPa]$
150	12	12	0.32	0.436	0.32	5170	3980	5170

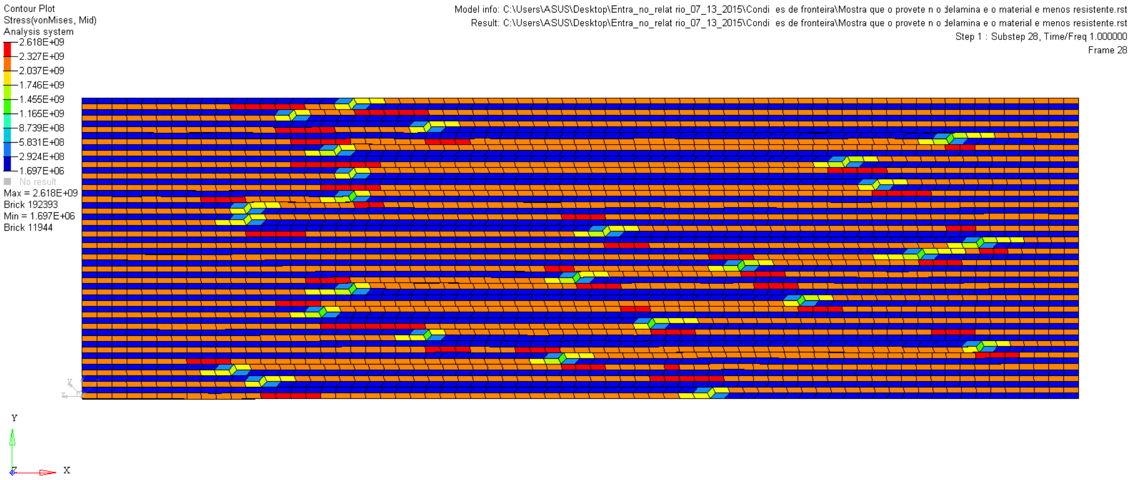

Figure 4.2 - Results of the first compression test

As it can be seen, after a displacement of $0.2\,mm$, the compression specimen does not present delamination, contrary to what was expected because the experimental specimens show delamination after the compression test, with the same displacement. This means the cohesive material properties need to be adjusted, so the delamination can be seen after a compression simulation with a displacement of $0.2\,mm$.

After some simulations (less than ten) it was conclude that cohesive material properties that can provide a better final appearance, which means delamination can be perfectly identified and the model after the compression test looks like the real specimens tested experimentally, are the following presented in Table 4.3. As it can be seen, only the maximum normal stress and the maximum tangential stress were changed, the normal stress was changed from $60\,MPa$ to $30\,MPa$ and the tangential stress was changed from $90\,MPa$ to $10\,MPa$ (comparing with Table 3.6).

Table 4.3 - Interlaminar cohesive properties changed

$\sigma^n_{Máx}$ $[MPa]$	G_I $[J/m^2]$	$\tau_{Máx}$ $[MPa]$	G_{II} $[J/m^2]$	η
30	178.332	10	970.851	1.45

After this adjustment, three simulations were performed with different boundary conditions.

For each simulation there are three common restrictions: lock the surface $A1$ in the xx direction, in surface $A2$ is imposed a displacement of $-0.2\ mm$, and to avoid the translation in the zz axis the keypoint 5 (Figure 4.1) is constrained in this direction too. More constrains were added to these three conditions, taking at the end three different boundary conditions to simulate the model and compare the results.

For the first case, the boundary conditions applied are completed adding a constrain in the yy direction in surface $A3$ (the top surface). Boundary conditions for this analysis are presented in the Table 4.4, and the final results are shown in the Figure 4.3.

Table 4.4 - Boundary conditions (1) applied to the numerical model

$\boldsymbol{K5}$	$\boldsymbol{A1}$	$\boldsymbol{A2}$	$\boldsymbol{A3}$
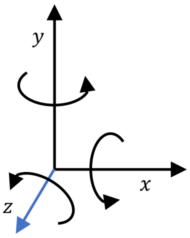	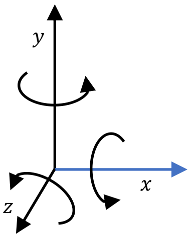	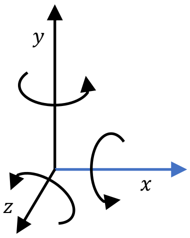	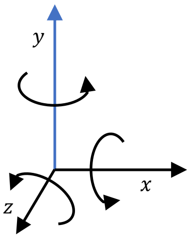
$U_z = 0$	$U_x = 0$	$U_x = -0.2\ mm$	$U_y = 0$

* The degrees of freedom painted in blue are the constrained ones

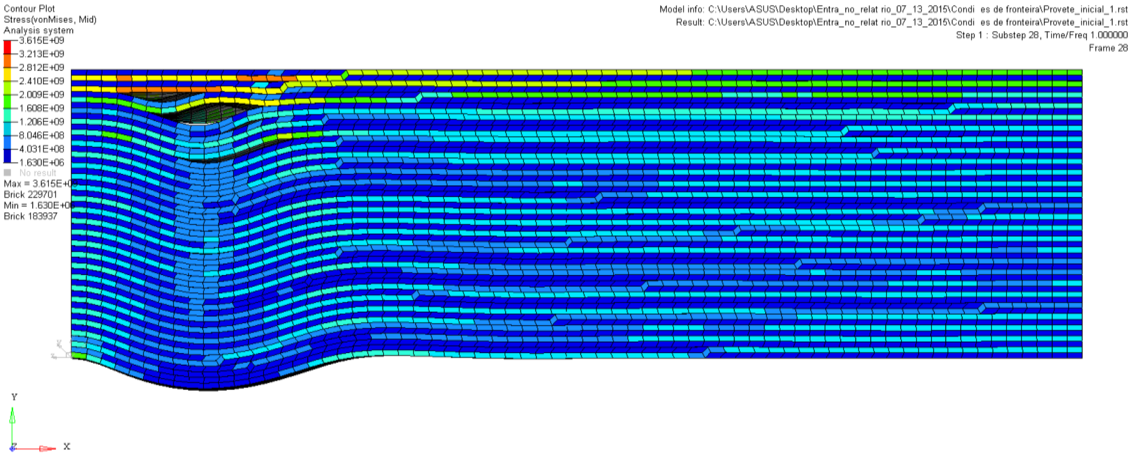

Figure 4.3 - Results of the compression test with the cohesive properties changed and the boundary conditions (1)

Now, is perfectly identified the delamination in the compressive specimen, which means the cohesive properties used here are closer to the real properties (that are unknown) than the properties used in the simulation of the Figure 4.2, that corresponds to the cohesive properties of a IM7/8552 unidirectional laminate. Although this results cannot be compared with the experimental results, because this simulation was only used to evaluate the delamination and final appearance of the specimen not considering the elements failure, results appear to be according to what was expected.

The experimental tests present an ultimate compression stress around the 330 MPa (which is shown in the Figure 4.26) and in this simulation this value is in the range of the elements results presented.

Boundary conditions for the second analysis are quite similar to those used in the first case, but in spite of applying constrains in yy direction of surface $A3$ that corresponds to the top surface of the specimen (as shown in Figure 4.1), the constrain is applied at surface ($A3$') in the middle of the specimen (parallel to $A3$ surface). These conditions are presented in the Table 4.5 and the corresponding results in Figure 4.4.

Table 4.5 - Boundary conditions (2) applied to the numerical model

$\boldsymbol{K5}$	$\boldsymbol{A1}$	$\boldsymbol{A2}$	$\boldsymbol{A3'}$
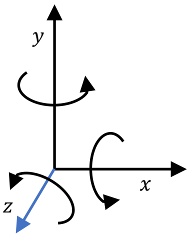	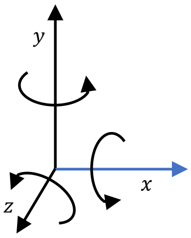	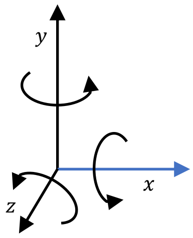	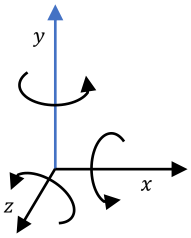
$U_z = 0$	$U_x = 0$	$U_x = -0.2\ mm$	$U_y = 0$

*$A3'$ is a parallel interface area to $A3$ in the middle of the specimen.

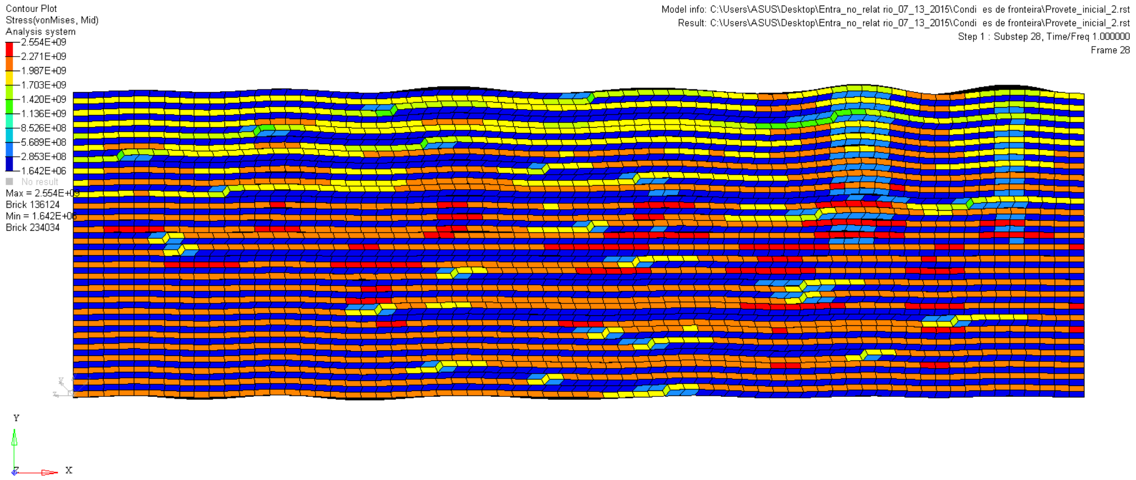

Figure 4.4 - Results of the compression test with the cohesive properties changed and the boundary conditions (2)

The final appearance of this simulation is also acceptable, showing some delamination areas and some buckling in the outer surfaces, which was visible in the compressive specimens experimentally tested.

The only drawback of these boundary conditions is the fact that the surface constrained in yy direction is a surface in the middle of the specimen, which may influence the damage propagation, in this area, during the simulation of the compression specimen. For this reason, these boundary conditions are not acceptable for this work.

Finally, in the third analysis it was implemented the boundary conditions that most closely resembles the experimental conditions. In this analysis the yy direction is just constrained in two keypoins, $K1$ and $K5$ (see Figure 4.1). Table 4.6 and Figure 4.5 presents the boundary conditions and the final results of this analysis, respectively.

Table 4.6 - Boundary conditions 3) applied to the numerical model

$\boldsymbol{K1}$	$\boldsymbol{K5}$	$\boldsymbol{A1}$	$\boldsymbol{A2}$
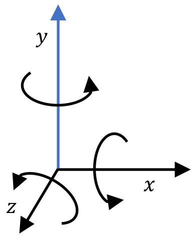	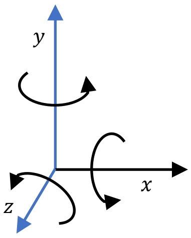	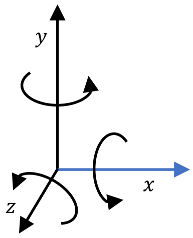	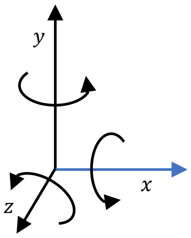
$U_y = 0$	$U_y = 0$ $U_z = 0$	$U_x = 0$	$U_x = -0.2\ mm$

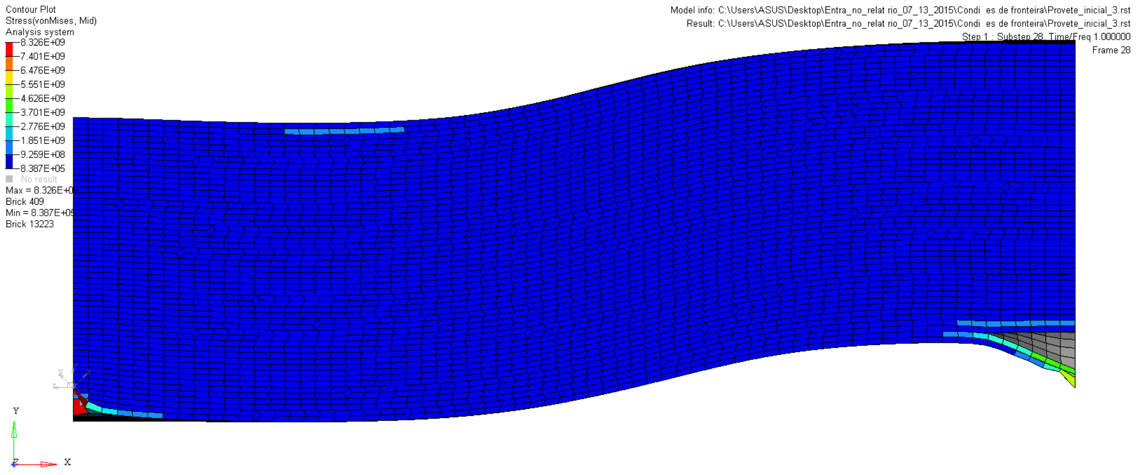

Figure 4.5 - Results of the compression test with the cohesive properties changed and the boundary conditions (3)

This third simulation, has the boundary conditions closer to the real ones, however the results are the most different. It presents a uniform stress distribution that is not real and the behavior of the material is too different from the experimented specimens.

These boundary conditions will not be used in this dissertation to simulate the damage propagation of the composite material.

Only the two first simulations used boundary conditions capable to provide acceptable stress results and a similar final appearance with the real specimens after the compression test. The only difference in the boundary conditions of these two simulations lies in the surfaces where constrains in the yy direction are applied. In the first simulation the constrained surface is located at one end of the specimen, while in the second simulation this surface is located in the middle of the specimen. Since the constraints in the yy direction can interfere directly in the damage propagation, it is more advantageous that this surface is located at the end of the compression specimen than in the middle.

Comparing the final results of the different simulations with different boundary conditions, it was concluded that the boundary conditions that give the most similar final appearance with the real specimens and less interfere with the damage propagation are those used in the first analysis.

As a reference, Figure 4.6 shows the numerical model presented in Figure 4.3 and one of the experimented specimens with a 0º/90º arrangement.

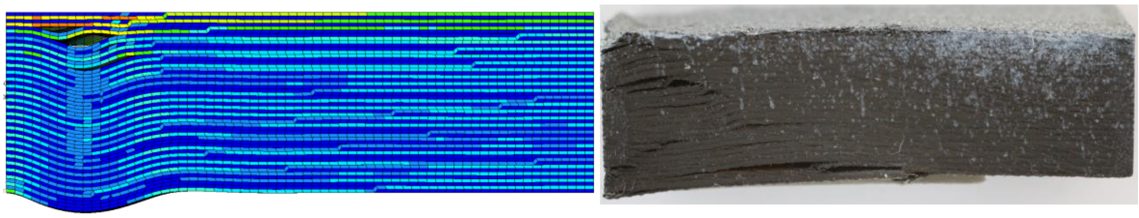

Figure 4.6 - Numerical model and real specimen

4.2. Incremental iterative analysis

The incremental iterative analysis, works, more or less, in the same way as described in Chapter 3 with some adjustments, different initial parameters and different composite material mechanical properties, in order to obtain final numerical results closer to the experimental results, with an error less than 5%.

The initial parameters used in this model are shown in Table 4.7 and the operation of the program used to simulate the damage propagation in the composite material's specimen is presented in the Figure 4.7.

With this analysis it shall be obtained the principal failure modes as observed in the experimental work, which are delamination simulated by the use of cohesive elements, and the fiber failure simulated with the "EKILL" function (from Ansys software), which reduces the stiffness of the element to almost zero.

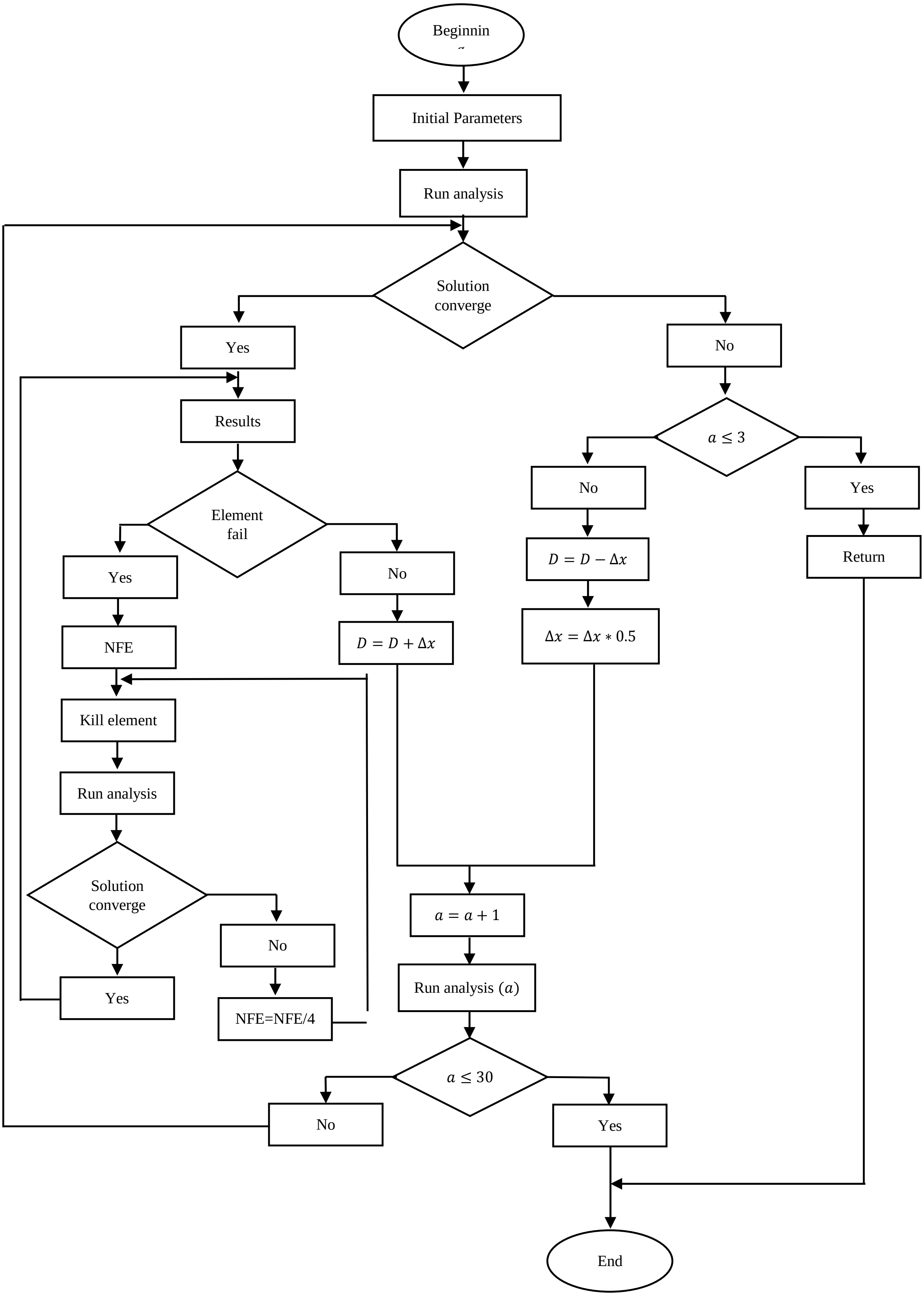
Beginnin
~
Initial Parameters
Run analysis
Solution converge
Yes
No
Results
$a \leq 3$
No
Yes
Element fail
Yes
No
$D = D - \Delta x$
Return
NFE
$D = D + \Delta x$
$\Delta x = \Delta x * 0.5$
Kill element
Run analysis
Solution converge
$a = a + 1$
No
Yes
NFE=NFE/4
Run analysis (a)
$a \leq 30$
No
Yes
End

Figure 4.7 - Incremental-iterative analysis for 26-plies compression specimen

As previously mentioned, the program was made by the use of an interface between Ansys and MatLab softwares and the analysis starts with an initial displacement which is gradually increased. In each analysis, stress results are analyzed and if any element fails, according to the Tsai-Wu or maximum stress failure criteria, its stiffness is reduced, which means fiber failure occurs (or matrix failure, depending on the direction of the fibers).

This type of simulation, requires a high CPU time (computational cost) and has great difficult of convergence. So, as referred in the Chapter 3, when there are identified elements that do not comply with the failure criterion (defined by the use of the unidirectional constants of the uniaxial tests presented on the Table 4.8 for this simulation), the displacement of the next iteration is not incremented and this is the point where the failure of the specimen occurs. Once the first elements fail, it leads to the failure of more elements and the displacement will not be incremented anymore during the simulation, just more elements will fail and be deactivated.

Every time an iteration does not converge, the displacement goes back to the value it had in the last converged iteration, and the value of the increment is reduced in 50%, so the stress values increase less and there are less elements to deactivate (in the case of being the first elements to fail) which helps the results of the iteration to converge. It is not usual, but it could happen the solution does not converge without the fail of any element, which means the increment should be reduced. The main difference of the program presented in this chapter and the program used to test one ply in tension (in Chapter 3) is due to the difficulty of the solution convergence after the failure of the first elements. To solve this, when the solution of the analysis does not converge (after the failure of the first elements), due to the high number of failed elements, the program reselect just 25% of these elements to deactivate.

Some initial parameters were chosen based on the experimental tests results. For example, the maximum displacement observed in the experimental tests was around $0.2\ mm$, which can be seen in the Figure 4.26, so for security it was used a maximum displacement of $0.22\ mm$ in the numerical model.

The values of the initial parameters as well as the material properties or the unidirectional constants of the uniaxial tests need to be values that provide final results close to the results obtained in the experimental test. For example, the value of the increment needs to be as low as possible taking into account the number of analyses is limited due to the high computational cost that these models requires. Other parameters that need to be adjusted for this analysis are the material mechanical properties and the unidirectional constants of the uniaxial tests, used in failure criterion, focusing on the failure stress, that was about $330\ MPa$ in the experimental tests and taking into account that the maximum extension was around 1%. So, the modulus of elasticity of the material in the longitudinal and transverse directions must be changed as well as the failure stress under longitudinal compression, X_C, and the failure stress under transverse compression, Y_C.

Table 4.7 - Initial parameters of the 0º/90º spread tow carbon fabric compressive specimen

Δx_{Max} $[mm]$	D $[mm]$	Δx $[mm]$	a_{Max} $[mm]$	E_S $[mm]$	$ESTIF$ $[mm]$
-0.22	-0.02	-0.01	30	0.3	10^{-6}

*Values taken from Kawashita's article [38]

The unidirectional constants of the uniaxial tests, presented in Table 4.8, are very important in the final results. Since the values for the material used in this dissertation are unknown and it was seen that these values for a Hexcel Ply IM7/8552 were too high, it had to be changed in order to achieve good results.

In this compression test (compression specimen with a 0º/90º arrangement) the main applied loads on the specimen are longitudinal and transversal compression. So, the most important unidirectional constants are the failure stress under longitudinal compression, X_C, for the material whose fibers are oriented at 0° and the failure stress under transverse compression, Y_C, for the material whose fibers are oriented at 90°

These values were not based in any reference, since the material is unknown, and are the initial values to evaluate the behavior of the material as well as the final results. Probably, they will need to be adjusted after the first simulation.

Table 4.8 - Unidirectional constants of the uniaxial tests used in the simulation of 26-plies specimen under compression loads.

X_T $[MPa]$	X_C $[MPa]$	Y_T $[MPa]$	Y_C $[MPa]$	S_L $[MPa]$
900	600	62.3	250	92.3

However, experimental results have to be taken into account because one of the main goals of this dissertation is the development of numerical model that lead to similar results as the experimental.

It was seen the experimental specimens collapse with a strain of 1%, which correspond to a displacement of $0.2\ mm$. For that, the modulus of elasticity in transverse and longitudinal directions are given by:

$$E_{11} = \frac{\sigma_{11}}{\varepsilon_{11}} \tag{62}$$

$$E_{22} = \frac{\sigma_{22}}{\varepsilon_{11}} \tag{63}$$

Considering $\sigma_{11} = X_C$ and $\sigma_{22} = Y_C$, with a strain of 1%, the modulus of elasticity were changed to the values presented on the Table 4.9. The rest of the values were kept.

These values predicted for the modulus of elasticity are acceptable and make sense. In Figure 4.26, results of the experimental compression test, for the specimen with a 0º/90º arrangement, present a failure stress about $330\,MPa$ with a strain of 1%, which provide a modulus of elasticity of $33\,GPa,$ approximately. This is much lower from the initial values used, corresponding to the mechanical properties of a Hexcel ply IM7/8552.

Table 4.9 - Composite material mechanical properties used

E_{11} $[GPa]$	E_{22} $[GPa]$	E_{33} $[GPa]$	ν_{12}	ν_{23}	ν_{13}	G_{12} $[MPa]$	G_{23} $[MPa]$	G_{13} $[MPa]$
60	2.5	2.5	0.32^*	0.436^*	0.32^*	5170^*	3980^*	5170^*

*Values taken from Kawashita’s article [38]

4.3. Results

The simulation of a compression test of 26-plies specimen was performed, with the parameters and the boundary conditions described above in Chapter 4 and the final results are presented in Figure 4.8-Figure 4.14.

Figure 4.15 presents the global stress-strain curve diagram, obtained considering the resultant force applied along x at the specimen boundary divided by the initial cross-section area, for the stress, and the applied x displacement divided by the specimen initial length, for the strain.

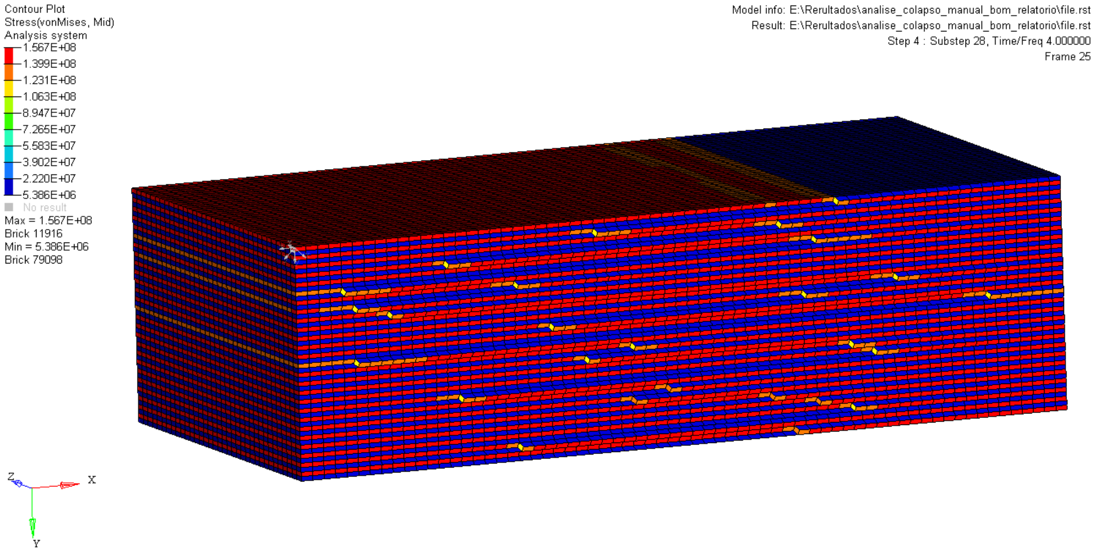
Contour Plot
Stress(vonMises, Mid)
Analysis system
1.567E+08
1.399E+08
1.231E+08
1.063E+08
8.947E+07
7.265E+07
5.583E+07
3.902E+07
2.220E+07
5.386E+06
No result
Max = 1.567E+08
Brick 11916
Min = 5.386E+06
Brick 79098
Model info: E:\Rerultados\analise_colapso_manual_bom_relatorio\file.rst
Result: E:\Rerultados\analise_colapso_manual_bom_relatorio\file.rst
Step 4 : Substep 28, Time/Freq 4.000000
Frame 25
Z
X
Y

Figure 4.8 - Equivalent Von-Mises Stress Analysis of a 26-plies compression specimen at step 4

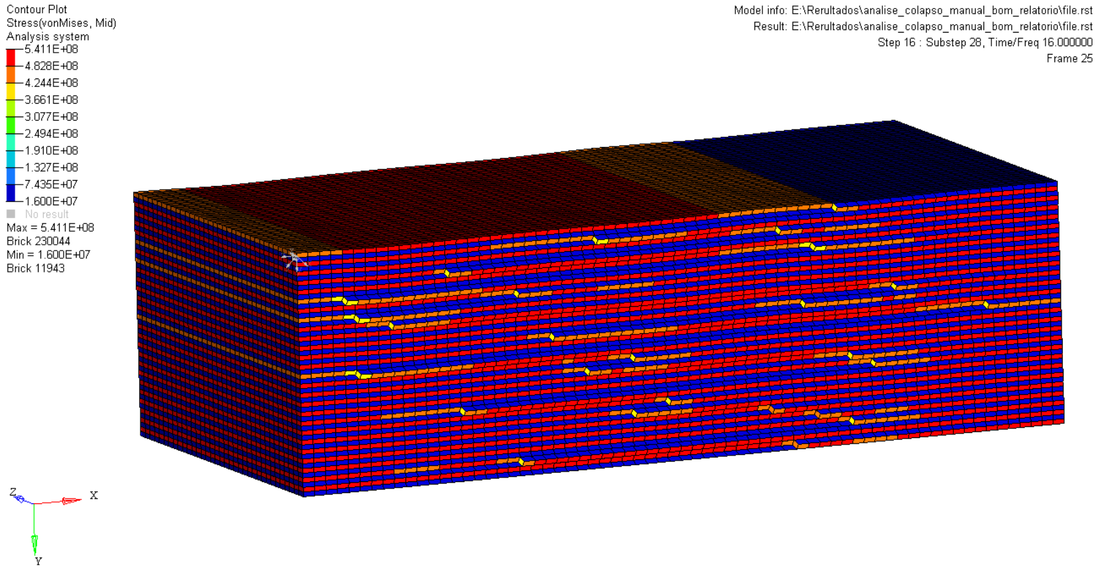
Contour Plot
Stress(vonMises, Mid)
Analysis system
5.411E+08
4.828E+08
4.244E+08
3.661E+08
3.077E+08
2.494E+08
1.910E+08
1.327E+08
7.435E+07
1.600E+07
No result
Max = 5.411E+08
Brick 230044
Min = 1.600E+07
Brick 11943
Model info: E:\Rerultados\analise_colapso_manual_bom_relatorio\file.rst
Result: E:\Rerultados\analise_colapso_manual_bom_relatorio\file.rst
Step 16 : Substep 28, Time/Freq 16.000000
Frame 25
Z
X
Y

Figure 4.9 - Equivalent Von-Mises Stress Analysis of a 26-plies compression specimen at step 16

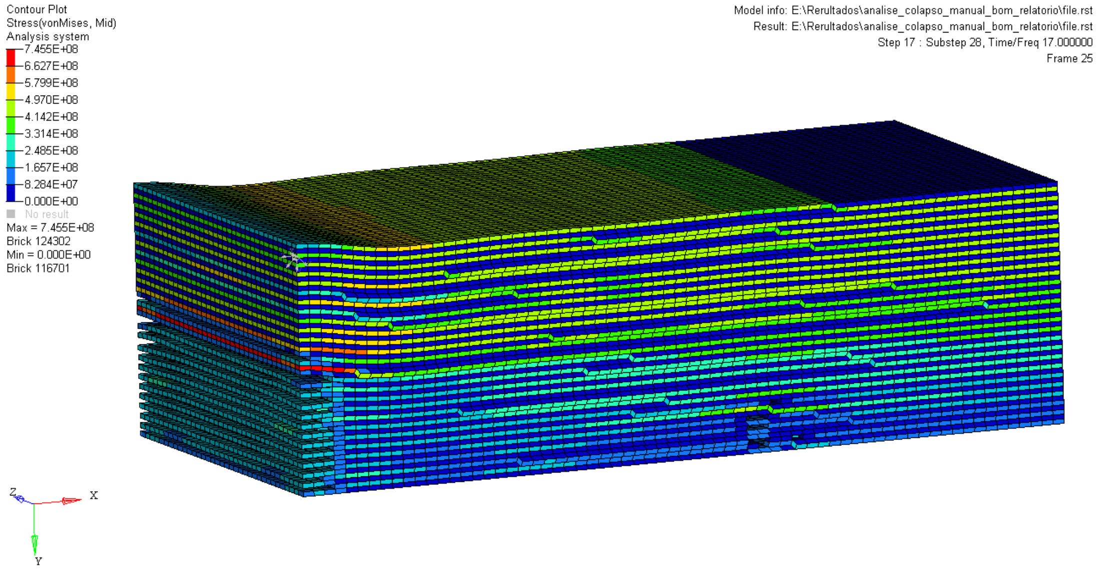
Contour Plot
Stress(vonMises, Mid)
Analysis system
7.455E+08
6.627E+08
5.799E+08
4.970E+08
4.142E+08
3.314E+08
2.485E+08
1.657E+08
8.284E+07
0.000E+00
No result
Max = 7.455E+08
Brick 124302
Min = 0.000E+00
Brick 116701
Model info: E:\Rerultados\analise_colapso_manual_bom_relatorio\file.rst
Result: E:\Rerultados\analise_colapso_manual_bom_relatorio\file.rst
Step 17 : Substep 28, Time/Freq 17.000000
Frame 25
Z
X
Y

Figure 4.10 - Equivalent Von-Mises Stress Analysis of a 26-plies compression specimen at step 17

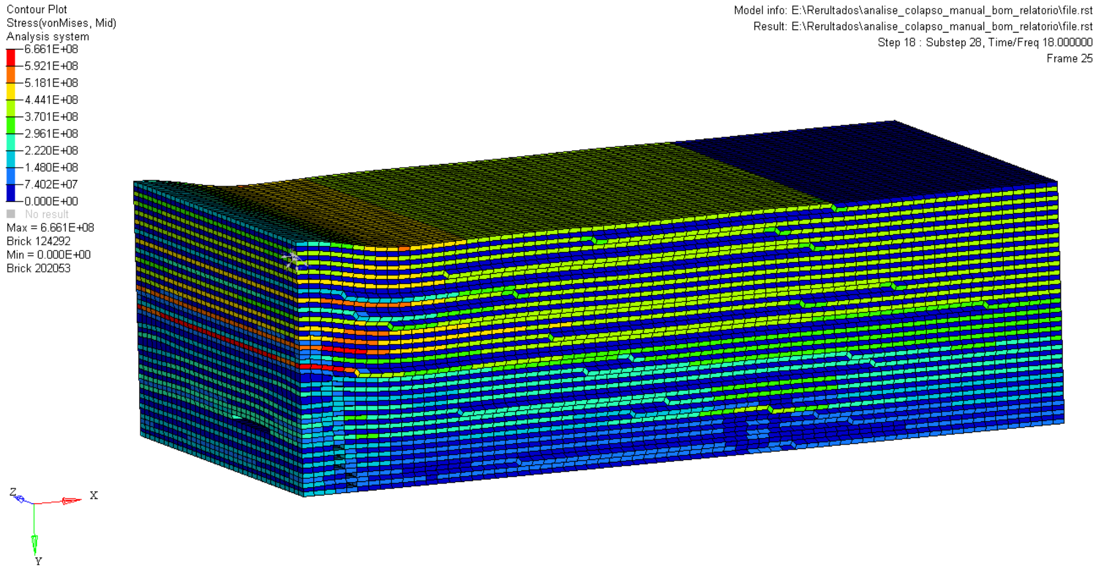
Contour Plot
Stress(vonMises, Mid)
Analysis system
6.661E+08
5.921E+08
5.181E+08
4.441E+08
3.701E+08
2.961E+08
2.220E+08
1.480E+08
7.402E+07
0.000E+00
No result
Max = 6.661E+08
Brick 124292
Min = 0.000E+00
Brick 202053
Model info: E:\Rerultados\analise_colapso_manual_bom_relatorio\file.rst
Result: E:\Rerultados\analise_colapso_manual_bom_relatorio\file.rst
Step 18 : Substep 28, Time/Freq 18.000000
Frame 25
Z
X
Y

Figure 4.11 - Equivalent Von-Mises Stress Analysis of a 26-plies compression specimen at step 18

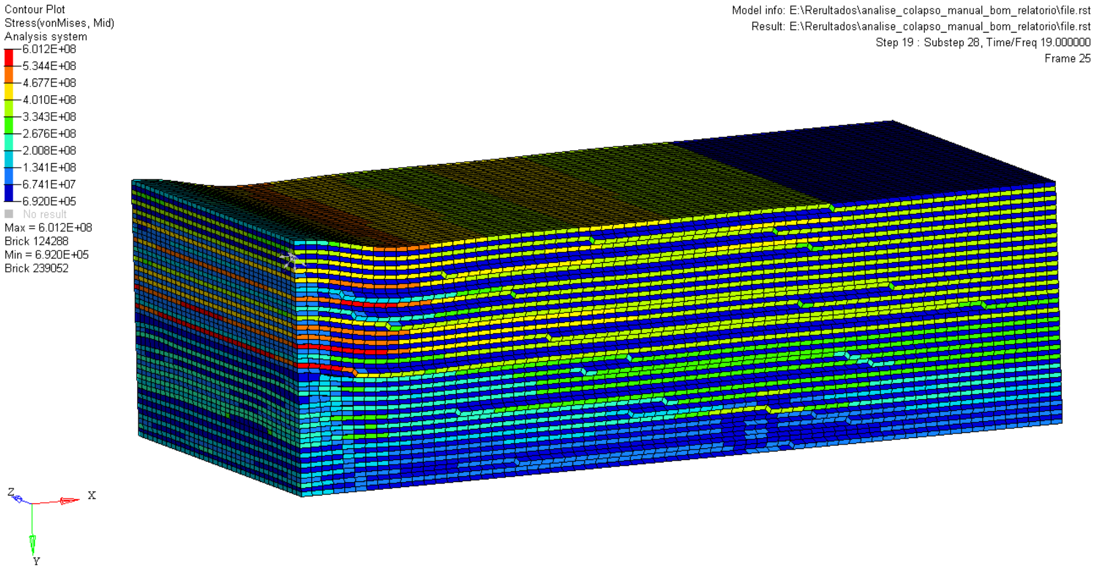
Contour Plot
Stress(vonMises, Mid)
Analysis system
6.012E+08
5.344E+08
4.677E+08
4.010E+08
3.343E+08
2.676E+08
2.008E+08
1.341E+08
6.741E+07
6.920E+05
No result
Max = 6.012E+08
Brick 124288
Min = 6.920E+05
Brick 239052
Model info: E:\Rerultados\analise_colapso_manual_bom_relatorio\file.rst
Result: E:\Rerultados\analise_colapso_manual_bom_relatorio\file.rst
Step 19 : Substep 28, Time/Freq 19.000000
Frame 25
Z
X
Y

Figure 4.12 - Equivalent Von-Mises Stress Analysis of a 26-plies compression specimen at step 19

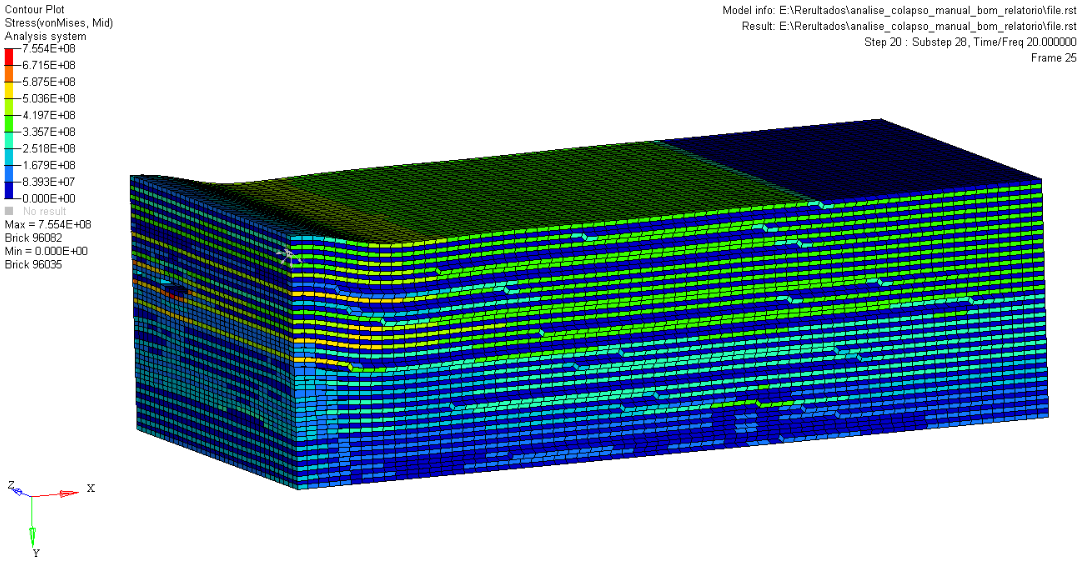
Contour Plot
Stress(vonMises, Mid)
Analysis system
7.554E+08
6.715E+08
5.875E+08
5.036E+08
4.197E+08
3.357E+08
2.518E+08
1.679E+08
8.393E+07
0.000E+00
No result
Max = 7.554E+08
Brick 96082
Min = 0.000E+00
Brick 96035
Model info: E:\Rerultados\analise_colapso_manual_bom_relatorio\file.rst
Result: E:\Rerultados\analise_colapso_manual_bom_relatorio\file.rst
Step 20 : Substep 28, Time/Freq 20.000000
Frame 25
Z
X
Y

Figure 4.13 - Equivalent Von-Mises Stress Analysis of a 26-plies compression specimen at step 20

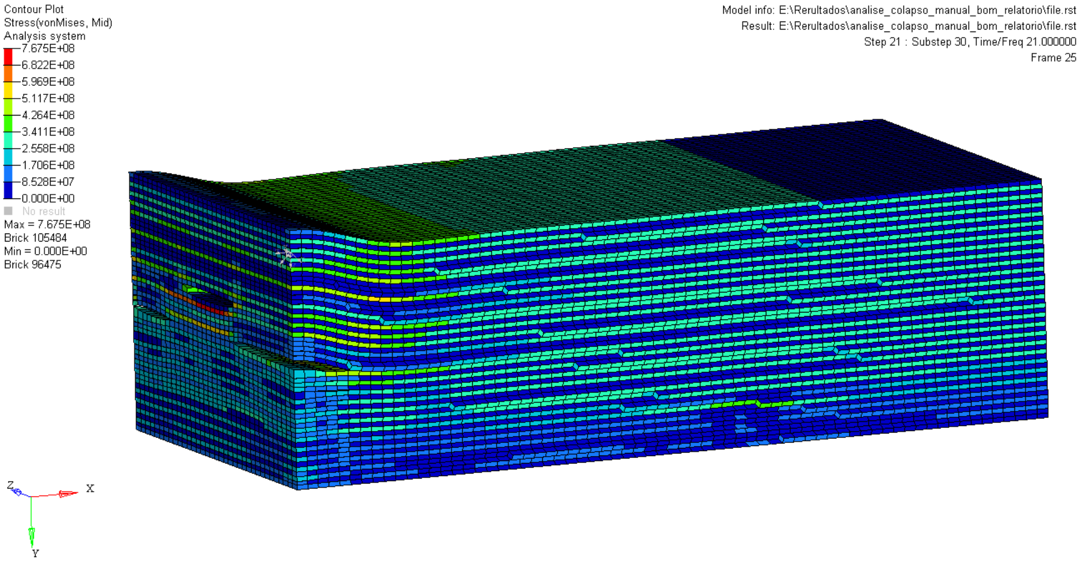
Contour Plot
Stress(vonMises, Mid)
Analysis system
7.675E+08
6.822E+08
5.969E+08
5.117E+08
4.264E+08
3.411E+08
2.558E+08
1.706E+08
8.528E+07
0.000E+00
No result
Max = 7.675E+08
Brick 105484
Min = 0.000E+00
Brick 96475
Model info: E:\Rerultados\analise_colapso_manual_bom_relatorio\file.rst
Result: E:\Rerultados\analise_colapso_manual_bom_relatorio\file.rst
Step 21 : Substep 30, Time/Freq 21.000000
Frame 25
Z
X
Y

Figure 4.14 - Equivalent Von-Mises Stress Analysis of a 26-plies compression specimen at step 21

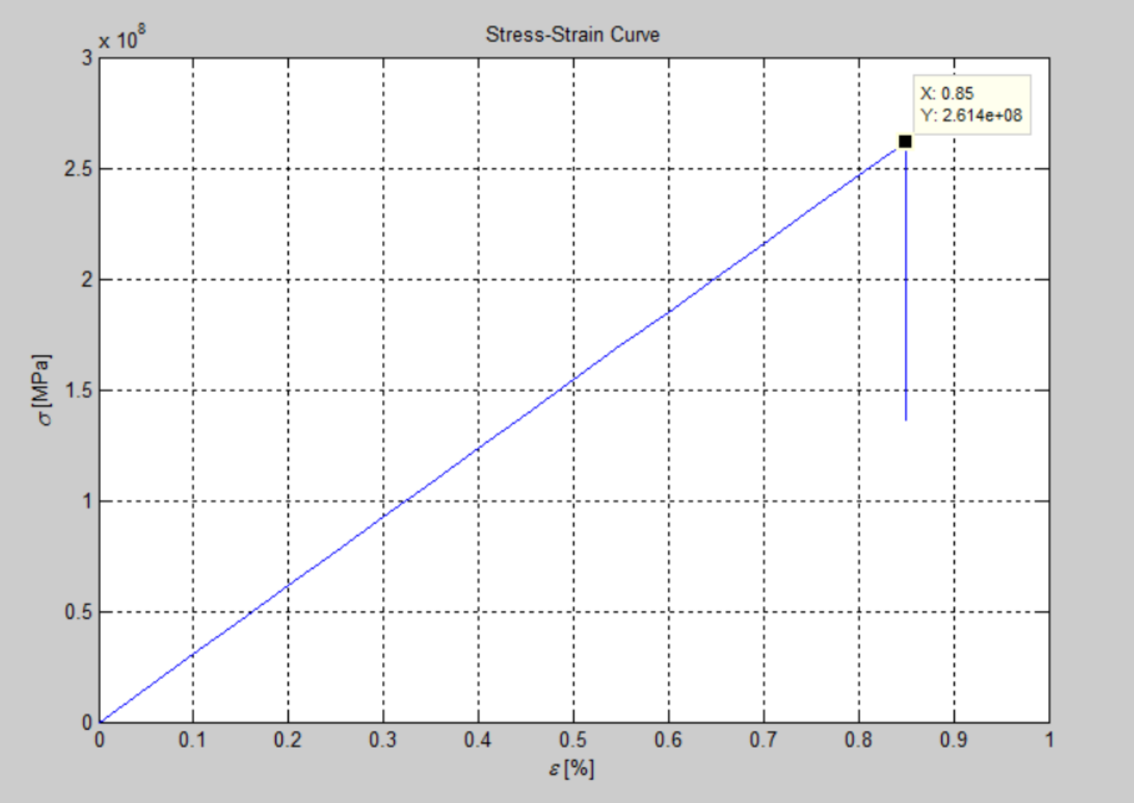

Figure 4.15 - Stress-Strain results of the simulation of a 26-plies compression specimen

The results of this analysis are similar to the results obtained in the experimental tests. The final appearance is very similar to the appearance of the compression specimens tested experimentally. Throughout Figure 4.8 to Figure 4.14 it can be seen stresses increasing gradually until the failure of the first elements, in Figure 4.10. The previous figure shows the first failed elements that correspond to the pick value in Figure 4.15. After that, the specimen lose its integrity, which means that the material failed in service, as it was expected.

In Figure 4.14 the delamination in one of the ends of the compression specimen model can be perfectly identified. This can also be observed in the experimental specimens.

Figure 4.15 provides a good stress-strain curve diagram (that is one of the objectives of this dissertation). This diagram does not show any non-linearity, such as the experimental diagram of the specimen with a 0°/90° arrangement.

Another aspect that should be noted is the moment corresponding to the failure of the specimen. It was expected that the numerical model could not increase the applied load after the deactivation of the first elements and this can be observed in this diagram. The first elements fail at a strain of 0.85% and after this iteration (17th iteration) the strain was no longer incremented, and the rest of the iterations (from the iteration 18 to iteration 21) just deactivated more elements. In the experimental results, this can also be observed, in Figure 4.26. So, it can be concluded that the specimen's numerical model presents a similar behavior to the experimental specimen.

However, the failure stress and its correspondent strain, in Figure 4.15, could be closer to the experimental results. In Figure 4.26, the values for the failure stress of the four specimens with a 0°/90° arrangement are $314.6\ MPa$, $298.9\ MPa$, $338.2\ MPa$ and $338.7\ MPa$. Discarding the value obtained in the second test (because the stress failure value of this specimen is lower than the rest of the results), these results give an average value of $330.5\ MPa$. The failure stress of the numerical model is equal to $261.4\ MPa$, representing an error of 20.9% in respect the experimental specimens.

One of the objectives of this dissertation is the development of a numerical model that provides results with an error lower than 5% relative to the experimental values. To achieve this, some numerical model parameters will be adjusted in order to obtain a closer correspondence. The next section provides the results of a simulation with adjusted parameters and later, in this chapter, a comparison between numerical and experimental results can be found.

4.3.1. Parameters adjustment

Looking at the stress-strain diagram obtained previously, it can be concluded that failure stress as well as the correspondent strain are lower than the results obtained experimentally. In order to achieve a higher failure stress and a higher failure strain in the numerical model some parameters for this model will be modified.

To accomplish this objective, it is enough to change four parameters: the failure stress under longitudinal compression, X_C, the failure stress under transverse compression, Y_C and the modulus of elasticity in both longitudinal and transversal directions. With higher values of these four parameters, the failure stress and failure strain will certainly increase, because the collapse of the specimen will happen later.

After several analysis performed for several different values of these parameters, the final update values were found. Table 4.10 and Table 4.11 presents the values of updated parameters.

Table 4.10 - Unidirectional constants of the uniaxial tests used in the simulation of 26-plies specimen under compression loads updated (X_C and Y_C)

$\boldsymbol{X_T}$ $[\boldsymbol{MPa}]$	$\boldsymbol{X_C}$ $[\boldsymbol{MPa}]$	$\boldsymbol{Y_T}$ $[\boldsymbol{MPa}]$	$\boldsymbol{Y_C}$ $[\boldsymbol{MPa}]$	$\boldsymbol{S_L}$ $[\boldsymbol{MPa}]$
900	852	62.3	320	92.3

Table 4.11 - Composite material mechanical properties adjusted (E_{11} and $E_{22} = E_{33}$)

E_{11} $[GPa]$	E_{22} $[GPa]$	E_{33} $[GPa]$	v_{12}	v_{23}	v_{13}	G_{12} $[MPa]$	G_{23} $[MPa]$	G_{13} $[MPa]$
62	4	4	0.32^*	0.436^*	0.32^*	5170^*	3980^*	5170^*

*Values taken from Kawashita's article [38]

4.3.1.1. Results

Another simulation was performed, with the same parameters and boundary conditions used in the first simulation of a 26-plies compression specimen, with the exception of the four parameters modified and presented above in Table 4.10 and Table 4.11.

The results of this simulation are present in Figure 4.16-Figure 4.22.

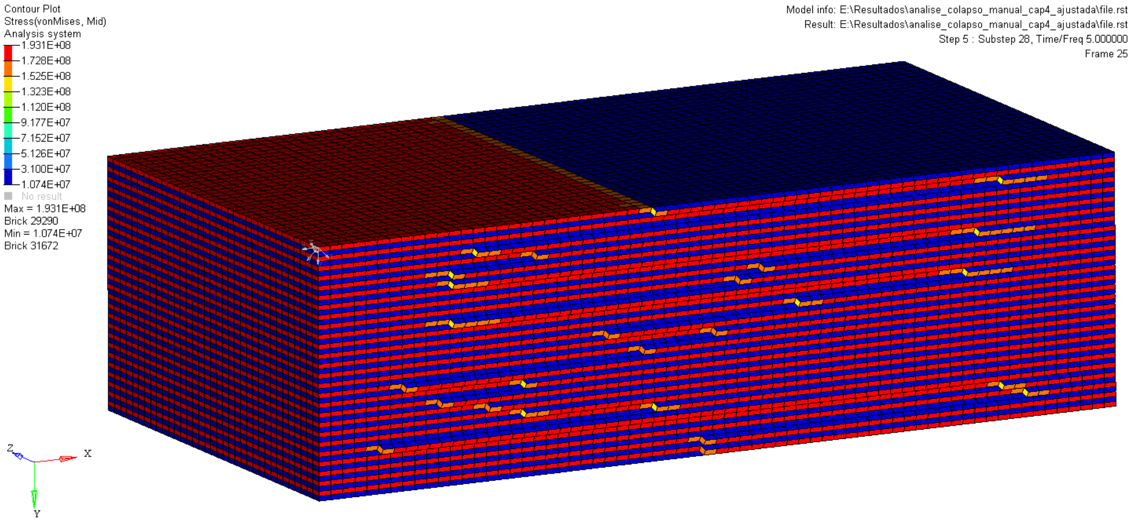
Contour Plot
Stress(vonMises, Mid)
Analysis system
1.931E+08
1.728E+08
1.525E+08
1.323E+08
1.120E+08
9.177E+07
7.152E+07
5.126E+07
3.100E+07
1.074E+07
No result
Max = 1.931E+08
Brick 29290
Min = 1.074E+07
Brick 31672
Model info: E:\Resultados\analise_colapso_manual_cap4_ajustada\file.rst
Result: E:\Resultados\analise_colapso_manual_cap4_ajustada\file.rst
Step 5 : Substep 28, Time/Freq 5.000000
Frame 25
Z
X
Y

Figure 4.16 - Equivalent Von-Mises Stress Analysis of a 26-plies compression specimen at step 5 (with adjusted parameters)

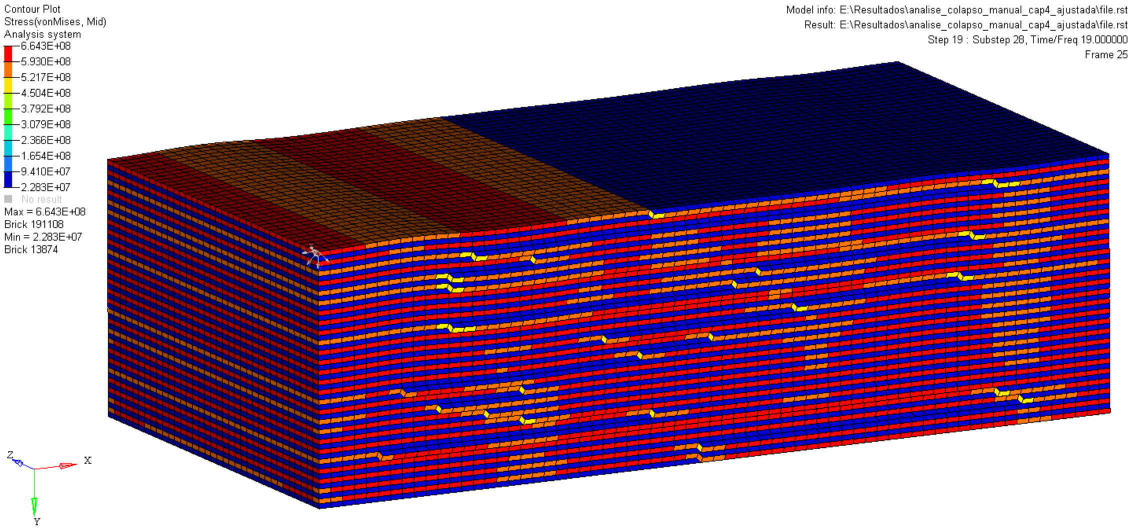
Contour Plot
Stress(vonMises, Mid)
Analysis system
6.643E+08
5.930E+08
5.217E+08
4.504E+08
3.792E+08
3.079E+08
2.366E+08
1.654E+08
9.410E+07
2.283E+07
No result
Max = 6.643E+08
Brick 191108
Min = 2.283E+07
Brick 13874
Model info: E:\Resultados\analise_colapso_manual_cap4_ajustada\file.rst
Result: E:\Resultados\analise_colapso_manual_cap4_ajustada\file.rst
Step 19 : Substep 28, Time/Freq 19.000000
Frame 25
Z
X
Y

Figure 4.17 - Equivalent Von-Mises Stress Analysis of a 26-plies compression specimen at step 19 (with adjusted parameters)

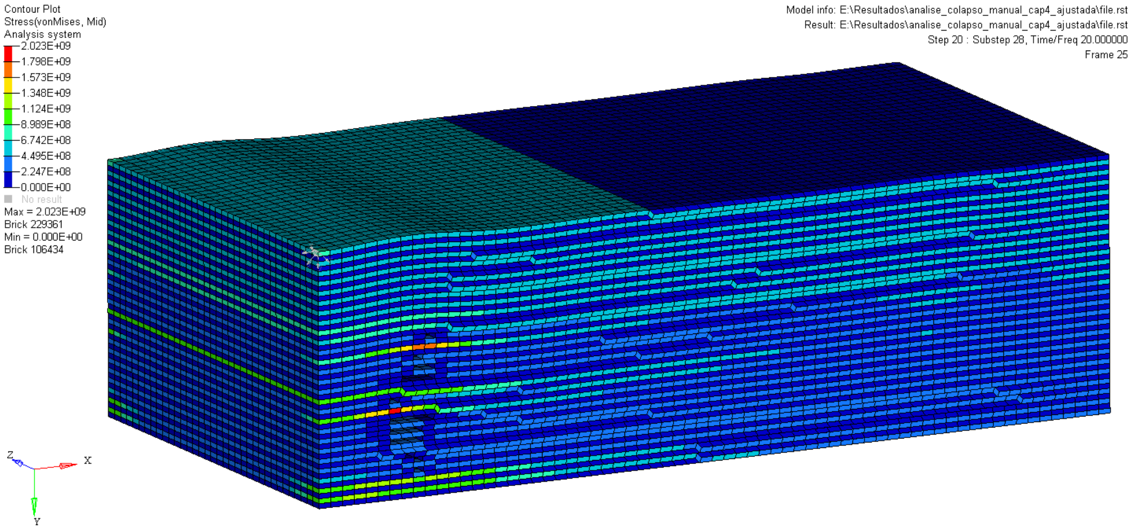
Contour Plot
Stress(vonMises, Mid)
Analysis system
2.023E+09
1.798E+09
1.573E+09
1.348E+09
1.124E+09
8.989E+08
6.742E+08
4.495E+08
2.247E+08
0.000E+00
No result
Max = 2.023E+09
Brick 229361
Min = 0.000E+00
Brick 106434
Model info: E:\Resultados\analise_colapso_manual_cap4_ajustada\file.rst
Result: E:\Resultados\analise_colapso_manual_cap4_ajustada\file.rst
Step 20 : Substep 28, Time/Freq 20.000000
Frame 25
Z
X
Y

Figure 4.18 - Equivalent Von-Mises Stress Analysis of a 26-plies compression specimen at step 20 (with adjusted parameters)

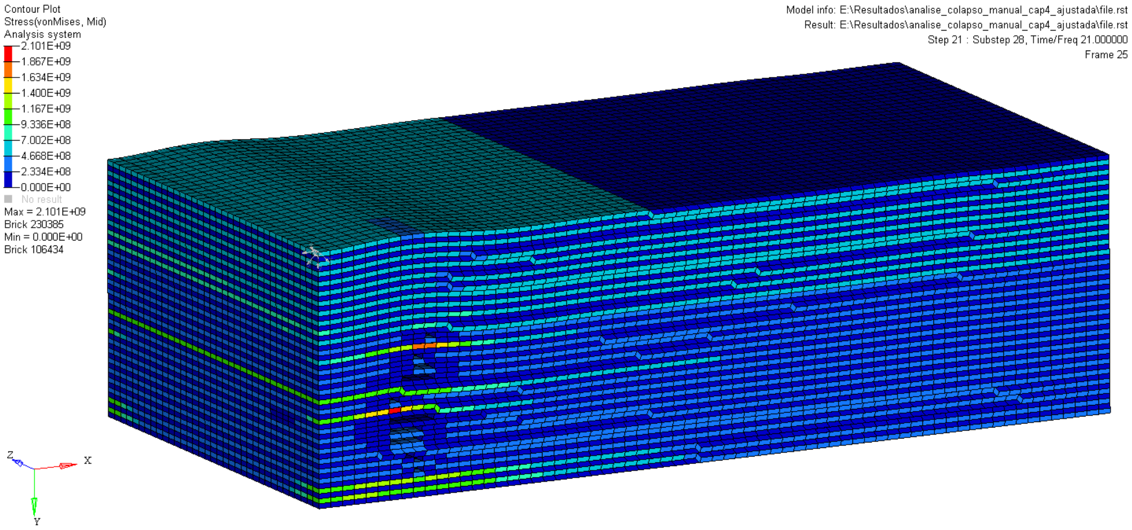
Contour Plot
Stress(vonMises, Mid)
Analysis system
2.101E+09
1.867E+09
1.634E+09
1.400E+09
1.167E+09
9.336E+08
7.002E+08
4.668E+08
2.334E+08
0.000E+00
No result
Max = 2.101E+09
Brick 230385
Min = 0.000E+00
Brick 106434
Model info: E:\Resultados\analise_colapso_manual_cap4_ajustada\file.rst
Result: E:\Resultados\analise_colapso_manual_cap4_ajustada\file.rst
Step 21 : Substep 28, Time/Freq 21.000000
Frame 25
Z
X
Y

Figure 4.19 - Equivalent Von-Mises Stress Analysis of a 26-plies compression specimen at step 21 (with adjusted parameters)

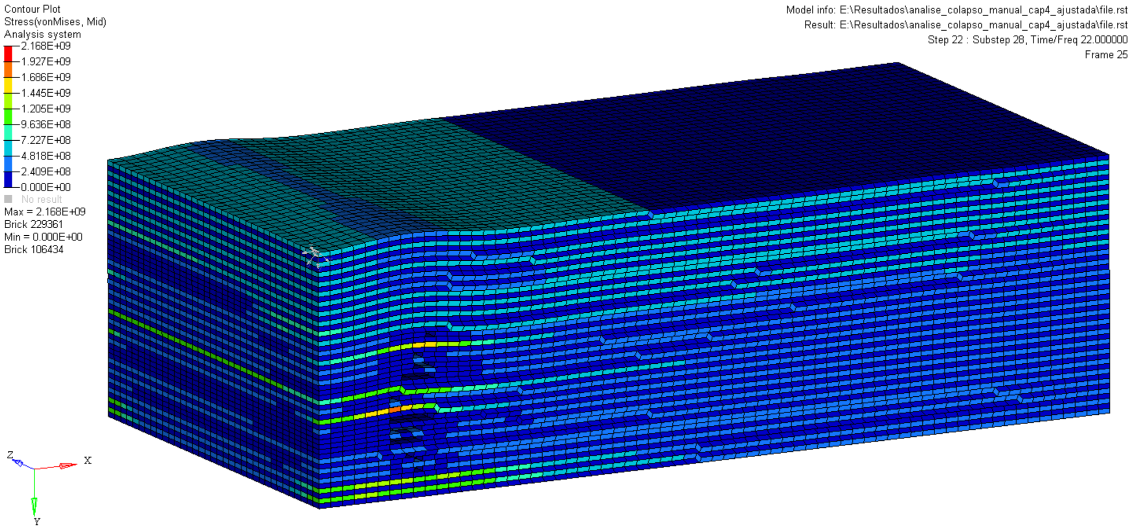
Contour Plot
Stress(vonMises, Mid)
Analysis system
2.168E+09
1.927E+09
1.686E+09
1.445E+09
1.205E+09
9.636E+08
7.227E+08
4.818E+08
2.409E+08
0.000E+00
No result
Max = 2.168E+09
Brick 229361
Min = 0.000E+00
Brick 106434
Model info: E:\Resultados\analise_colapso_manual_cap4_ajustada\file.rst
Result: E:\Resultados\analise_colapso_manual_cap4_ajustada\file.rst
Step 22 : Substep 28, Time/Freq 22.000000
Frame 25
Z
X
Y

Figure 4.20 - Equivalent Von-Mises Stress Analysis of a 26-plies compression specimen at step 22 (with adjusted parameters)

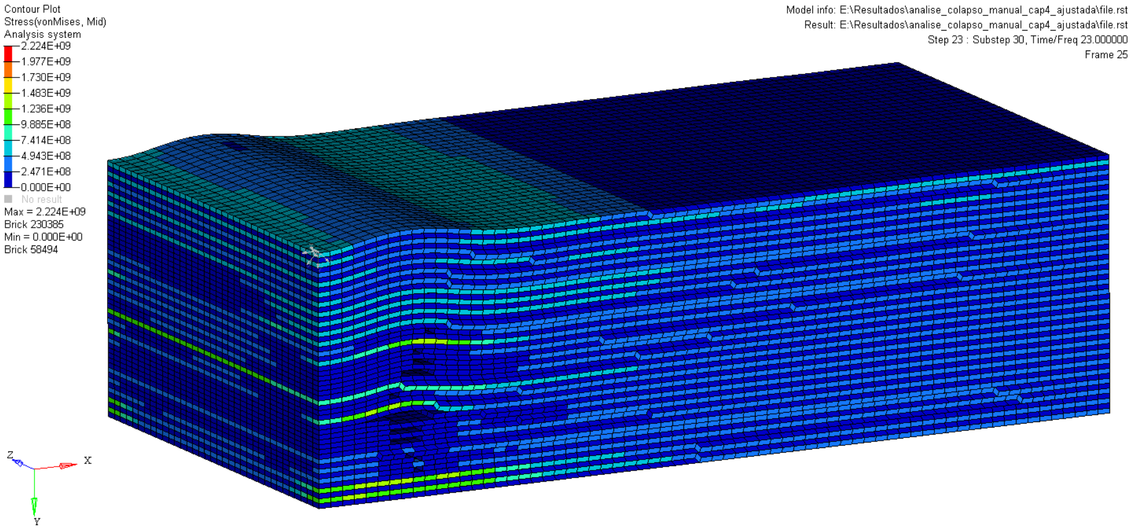
Contour Plot
Stress(vonMises, Mid)
Analysis system
2.224E+09
1.977E+09
1.730E+09
1.483E+09
1.236E+09
9.885E+08
7.414E+08
4.943E+08
2.471E+08
0.000E+00
No result
Max = 2.224E+09
Brick 230385
Min = 0.000E+00
Brick 58494
Model info: E:\Resultados\analise_colapso_manual_cap4_ajustada\file.rst
Result: E:\Resultados\analise_colapso_manual_cap4_ajustada\file.rst
Step 23 : Substep 30, Time/Freq 23.000000
Frame 25
Z
X
Y

Figure 4.21 - Equivalent Von-Mises Stress Analysis of a 26-plies compression specimen at step 23 (with adjusted parameters)

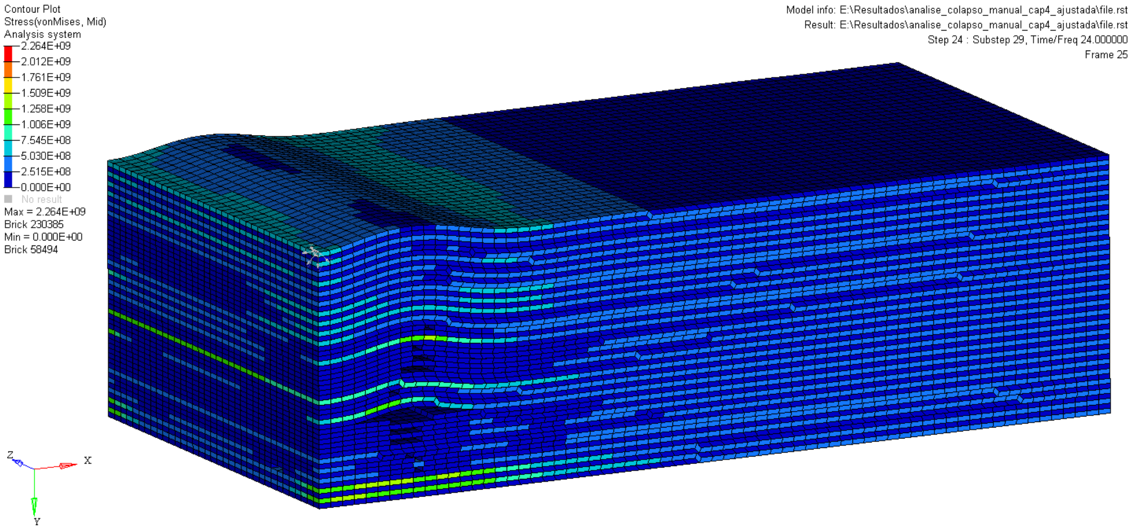
Contour Plot
Stress(vonMises, Mid)
Analysis system
2.264E+09
2.012E+09
1.761E+09
1.509E+09
1.258E+09
1.006E+09
7.545E+08
5.030E+08
2.515E+08
0.000E+00
No result
Max = 2.264E+09
Brick 230385
Min = 0.000E+00
Brick 58494
Model info: E:\Resultados\analise_colapso_manual_cap4_ajustada\file.rst
Result: E:\Resultados\analise_colapso_manual_cap4_ajustada\file.rst
Step 24 : Substep 29, Time/Freq 24.000000
Frame 25
Z
X
Y

Figure 4.22 - Equivalent Von-Mises Stress Analysis of a 26-plies compression specimen at step 24 (with adjusted parameters)

The simulation of the 26-plies compression specimen, after the parameters adjustment, presents a final appearance close to the experimental specimens (and close to the numerical model previously simulated), as was expected. The results show a small buckling in the specimen that starts in the 19th increment and grows as the elements fail.

Delamination can be observed once again, in the area where the elements failed. If the simulation had not stopped, the specimen would be divided in two parts, due to the propagation of the delaminated area. This propagation can be seen in these results, starting at the 23rd iteration (Figure 4.21) and grows to the 24th iteration (Figure 4.22).

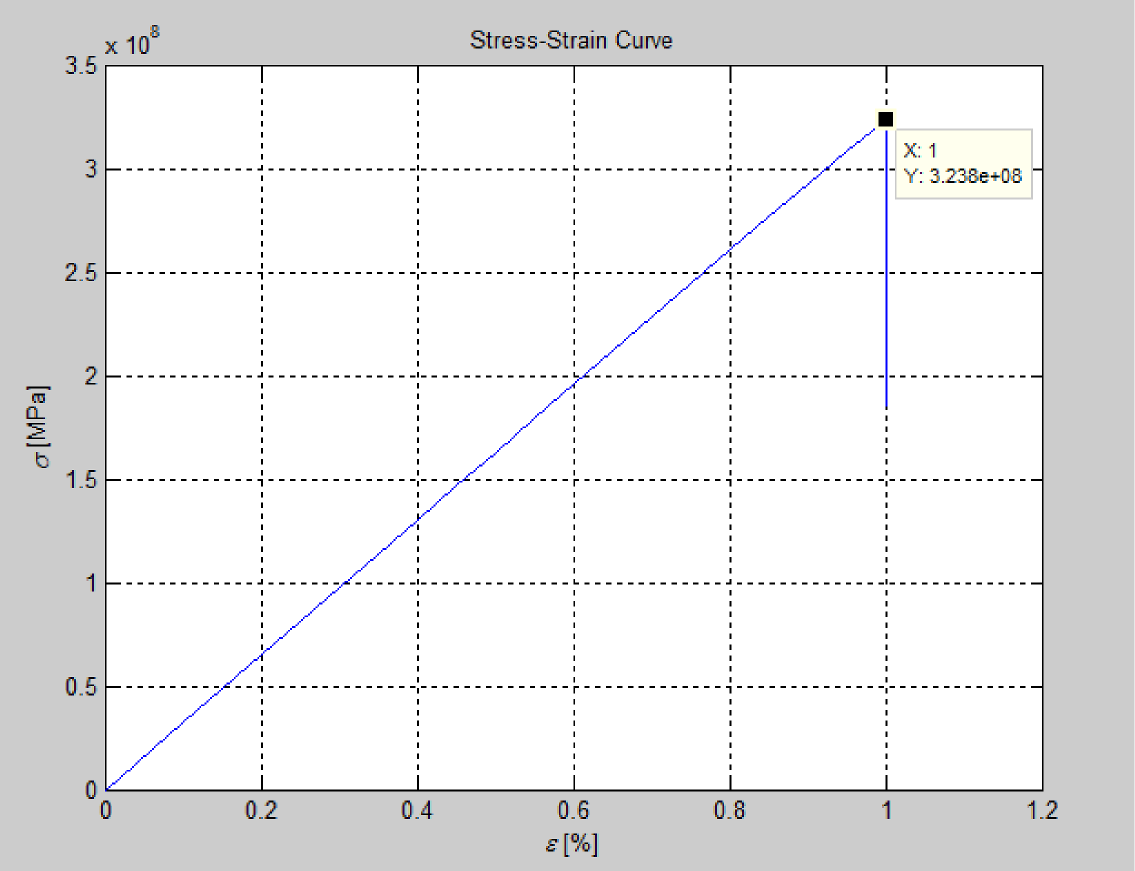

Figure 4.23 - Stress-Strain results of the simulation of a 26-plies compression specimen (with adjusted parameters)

Figure 4.23 shows the stress-strain curve for this simulation, and the behavior is quite similar to the previous 26-plies specimen numerical model, where the stress values increase until the failure of the first elements. When the first elements fail, the specimen also is unable to sustain higher loads, and the simulation ends.

This new simulation provides a failure stress value of 323.8 MPa corresponding to a strain value of 1%, which are very close to the experimental values. The average failure stresses of the compression specimens tested experimentally is 330.5 MPa with a strain around 1%. The failure strain value is in the average of the results obtained in the experimental tests (this error is not quantified because the strains of the experimental specimens were measured by five different extensometers, which provided different values around 1%, as it can be seen in the Figure 4.26). Regarding the failure stress, the result obtained in this simulation has an error of 2%, which is an exceptional result and compliant with the objectives set for this dissertation. With these last results, it can be concluded that no further parameter adjustment is need for the 26-plies specimen numerical model.

4.4. Experimental results

The procedure used in the experimental tests is explained in this chapter, and some results of the tested specimens are presented.

The different specimens are composed by spread tow carbon fabric material with different arrangements. The 0°/90° arrangement (arrangement simulated in the numerical model of this dissertation), and also the 15°/-75°, 30°/-60° and 45°/-45° arrangements.

As it was referred in Chapter 1, the work developed in this dissertation follows from these experimental tests driven by the need of better understanding the behavior of composite material during the experimental tests. Experimental tests do not provide the instant or the location of the failure initiation and damage propagation, that is intended to be studied in this dissertation, is difficult to analyze. In contrast, the numerical models provide a useful amount of data for various sub-steps during the simulation tests.

The experimental tests consists in compression tests of specimens with 26 plies of spread tow carbon fabric with the dimensions of $5 \times 10 \times 20\ mm$, approximately.

To extract the data from the experimental tests and draw the resistance curve of the specimens' two different methods were used: the digital image correlation (DIC) and the sensors installed on the machine that performed the experimental test. These sensors installed in the machine that perform the experimental test provide the stress values during the compression test and the displacement measured during the test while the digital image correlation provides directly the strain on the specimen by the use of five virtual extensometers implemented along the length of the specimen (see Figure 4.25).

To use digital image correlation method, test specimens were sprayed with a white ink to generate a random and contrasted distribution of granular spots against the grey color of the material of the specimen. This method uses the granular spots size and the distance between different spots to measure the displacement of the specimen in the 5 virtual extensometers.

The test set-up is shown in Figure 4.24. This test consists of an axial compression of the specimen between two flat plates.

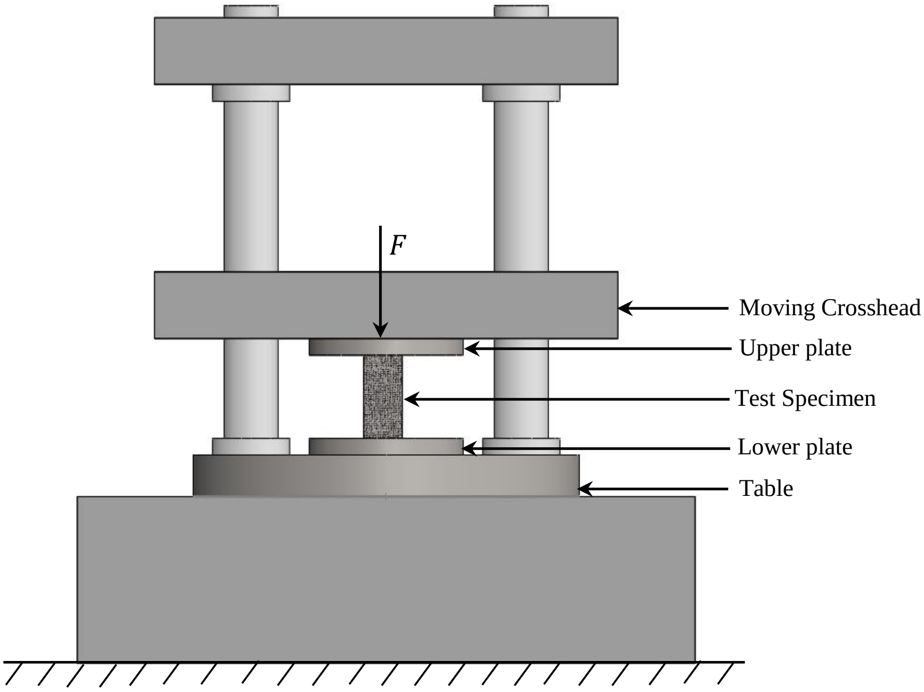
F
Moving Crosshead
Upper plate
Test Specimen
Lower plate
Table

Figure 4.24 - Schematic test set up of the experimental compression tests

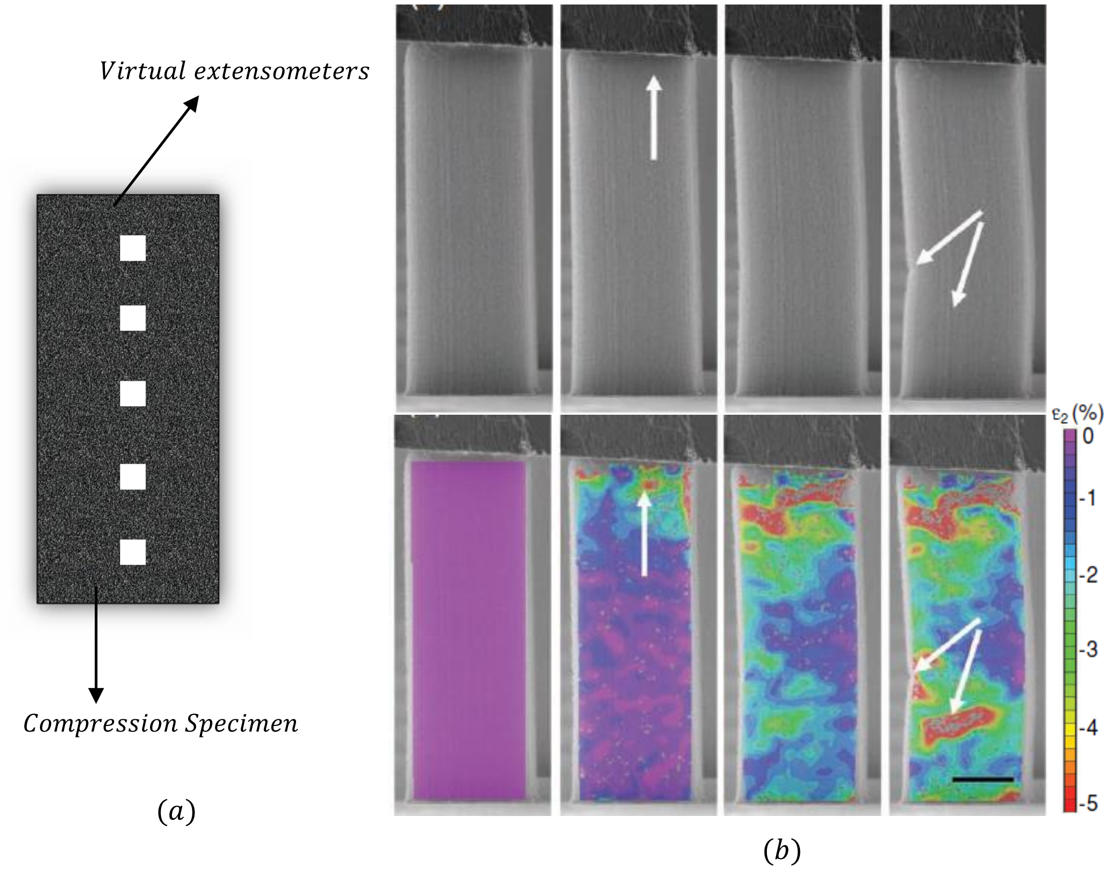
Virtual extensometers
Compression Specimen
(a)
ε2 (%)
0
-1
-2
-3
-4
-5
(b)

Figure 4.25 - (a) Schematic position of the virtual extensometers; (b) Digital image correlation: strain measurements [52]

The experimental tests were performed at a controlled velocity of 1 mm/min and the results of the experimental tests of the specimens with a 0°/90° arrangement are presented in Figure 4.26. The blue curves represent the data extracted from the digital image correlation method, while the curve in black represents the data extracted from the sensors installed on the machine that perform the tests. The strains measured by the machine are not considered since these values do not correspond only to the strain of the specimen but also include the adjustment of the machine to the specimen and deformations that can occur in the machine.

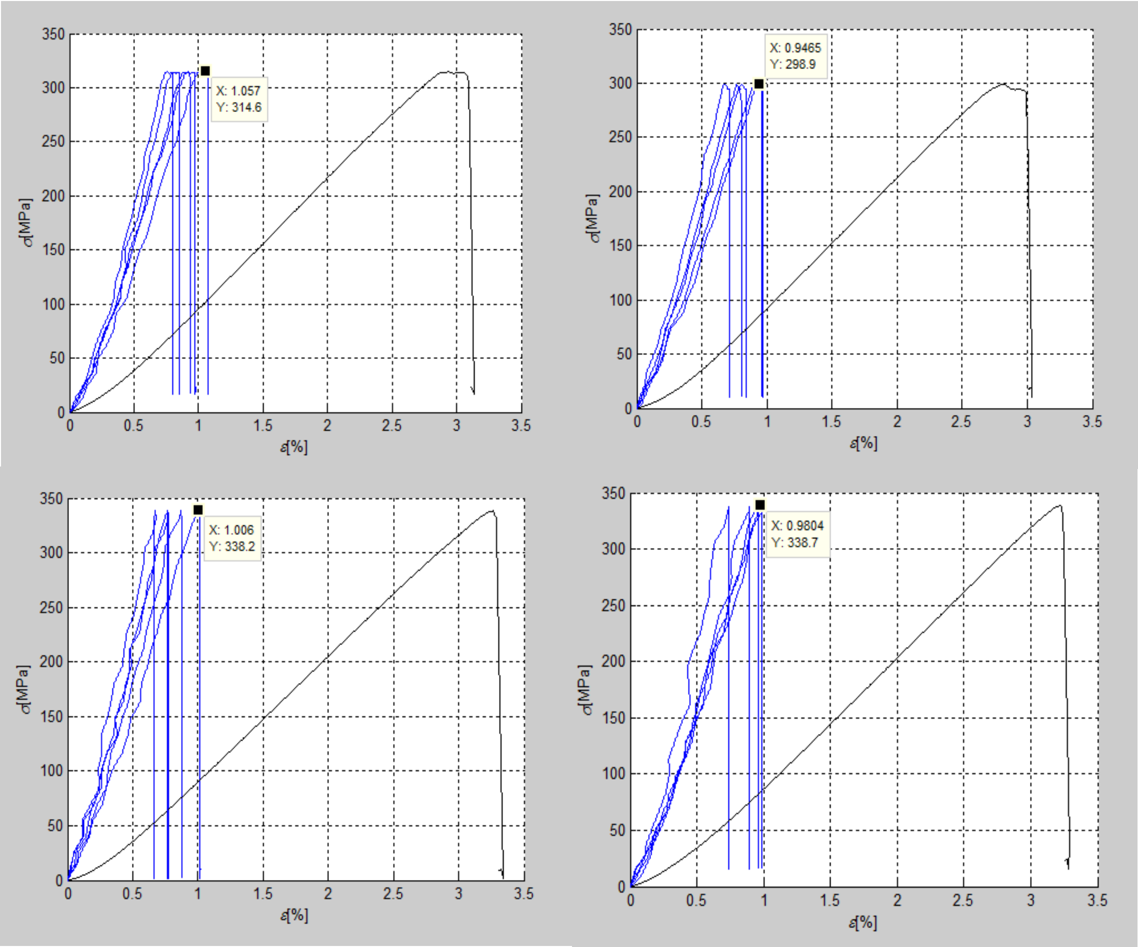

Figure 4.26 - Stress-strain curves of 4 different specimens with 26 plies and a 0°/90° arrangement, tested in compression

The stress-strain diagram presented in Figure 4.23 is very similar to the diagrams presented in Figure 4.26, all the four different experimental specimens present a failure stress between 300 MPa and 340 MPa with strains of 1%, which correspond to a displacement of 0.2 mm. These values were the basis of some parameters used in the numerical models, such as the maximum displacement or the unidirectional constants of the uniaxial tests (that are unknown in this dissertation and need to be adjusted).

4.4.1. Shear Plasticity

As previously discussed in Chapter 3, the composite material used in this dissertation presents plasticity only when subjected to shear loads. The work developed by Koerber [21], where it can be seen that the material used in that work (Hexel ply IM7/8552) presents a non-linear behavior when subjected to shear loads was also referred in this chapter. It was observed that non-linearity of the material increased drastically as the angle of the fibers' orientation decreased (from the 75° off-axis compression to the 45° off-axis compression).

Similar results were obtained in the experimental tests developed in this dissertation, before the numerical work began, with spread tow carbon fabric composite material. During these experimental tests, specimens with four different arrangements were tested: the 0°/90° arrangement, 15°/-75° arrangement, 30°/-60° arrangement and 45°/-45° arrangement.

Figure 4.27 shows the results of the compression test of these different arrangements. These stress-strain diagrams were obtained from the sensors installed in the machine that executed the compression test.

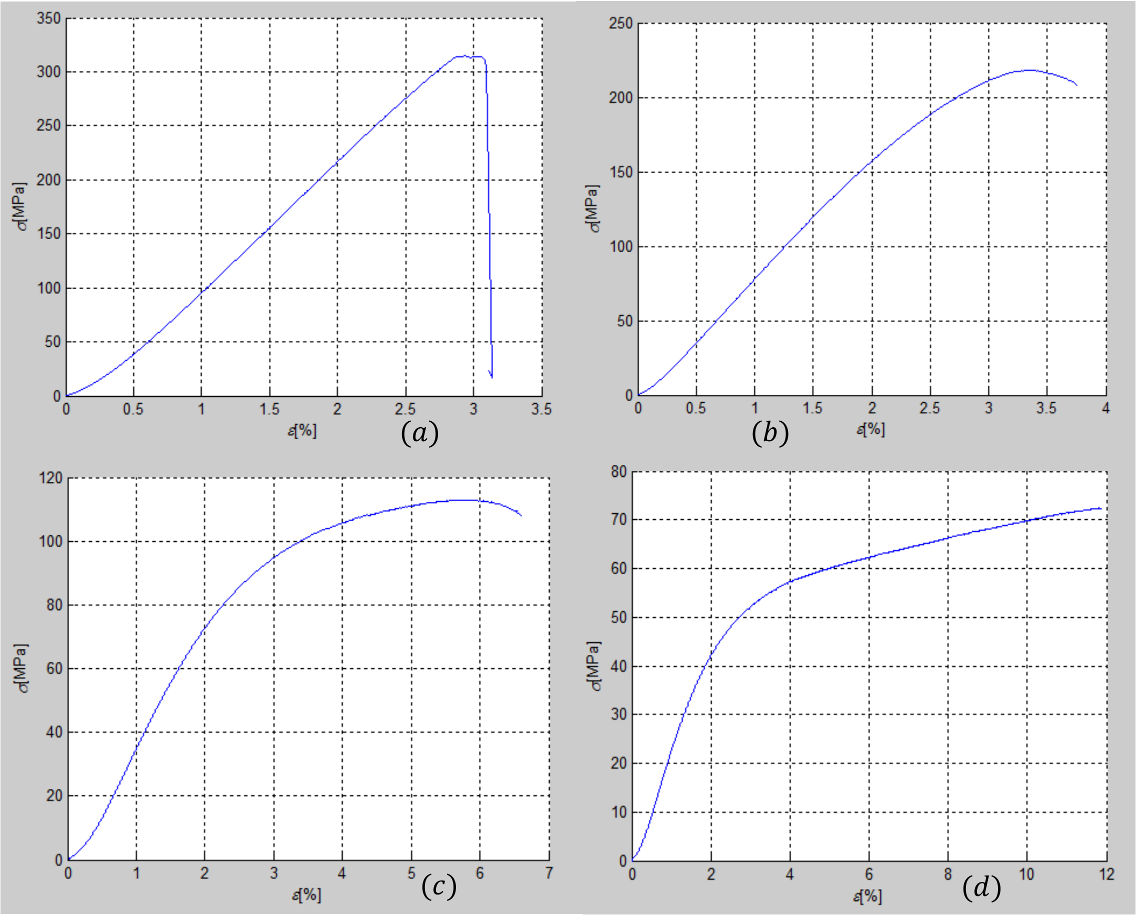

Figure 4.27 - Stress-strain curves resulting from the compression test of the specimens with (a) a 0°/90° arrangement, (b) 15°/-75° arrangement, (c) 30°/-60° arrangement and (d) 45°/-45° arrangement

These results are quite similar to those obtained by Koerber [21] on his work. For all the arrangements it can be observed that the non-linearity of the stress-strain curves increases. This is due to the plasticity of the material when subjected to shear loads. It is also observed that the failure stress decrease from the specimens with a 0°/90° arrangement (that are only subjected to longitudinal and transverse compression) to the specimens with a 45°/-45° arrangement, in contrast to the strains that increase from a 0°/90° to a 45°/-45° arrangement.

In Chapter 3, it was decided that plasticity under transverse compression was insignificant when compared to the plasticity under shear loads, therefore it would not be considered in the numerical model. By looking at the experimental results of the specimen with a 0º/90º arrangement (in Figure 4.27-(a), which is just under transverse compression and longitudinal compression loads), this was proven the right choice, since the stress-strain curve does not present any non-linearity before the failure of the specimen.

4.5.Comparison of Results

The aim of this section is to compare the stress-strain diagram provided by the 26-plies specimen numerical model with the stress-strain diagram obtained from the experimental work, presented above in this chapter.

Figure 4.28 presents, simultaneously the numerical results (in red) and the experimental results (in black).

Above in this chapter, it was mentioned that the error between the numerical and the experimental stress at failure was around 2%, which indicates values are very similar and this is shown in the diagrams of Figure 4.28. The behavior of the different experimented specimens is quite similar to the behavior of the numerical model. Hence complying the most important objective of this dissertation.

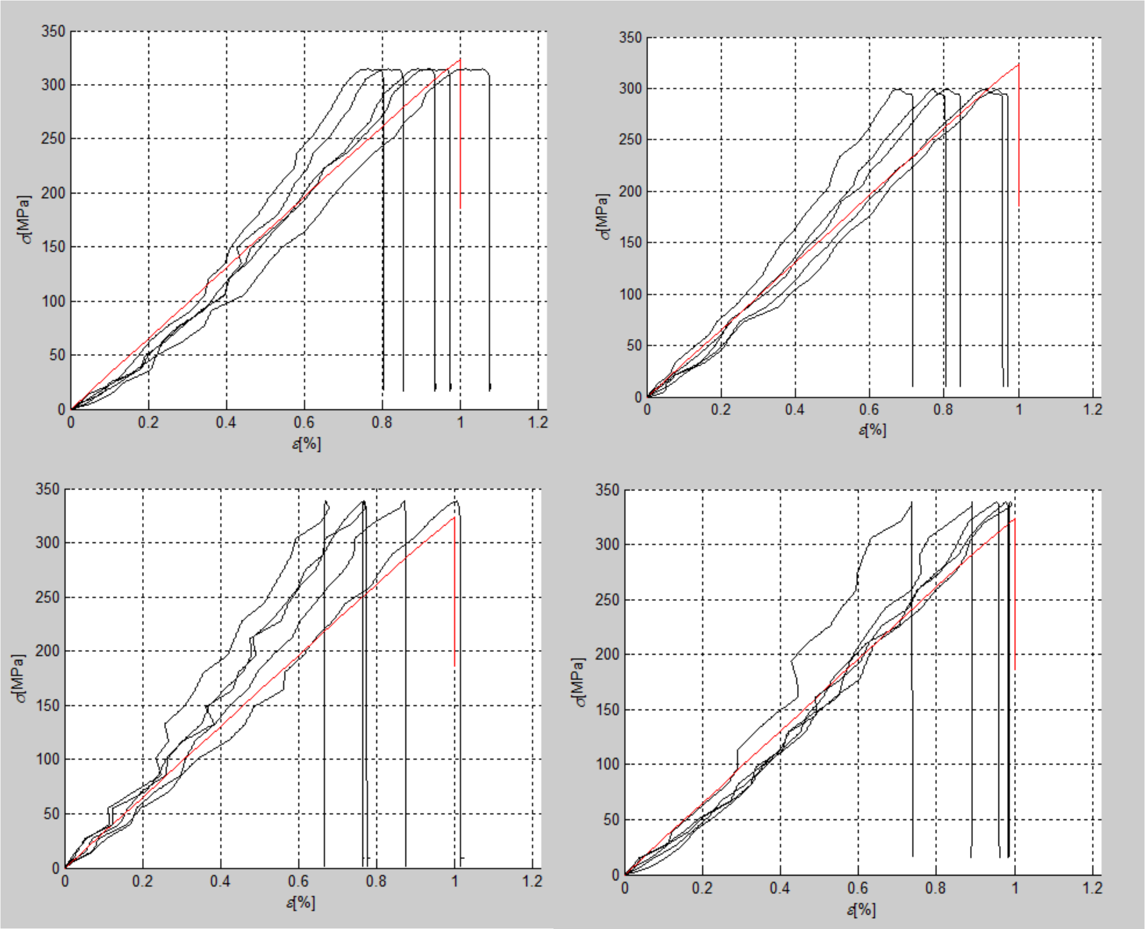

Figure 4.28 - Comparison between the stress-strain results of the experimental specimens (in black) and the numerical specimen with the adjusted parameters (in red)

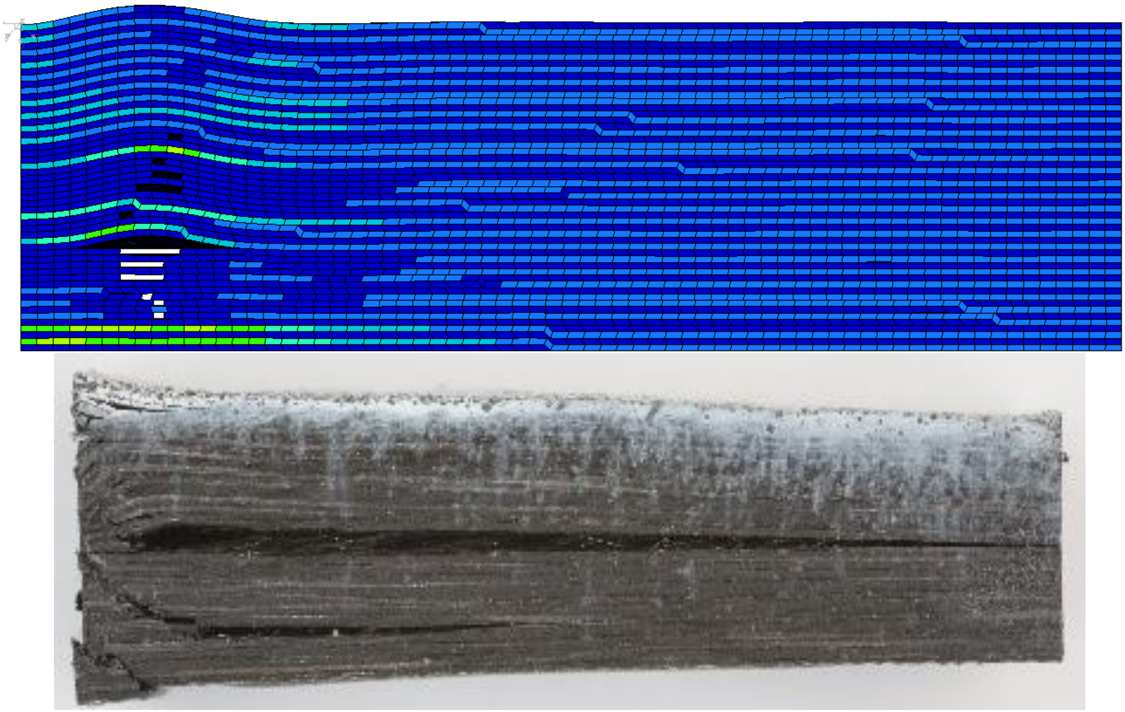

Figure 4.29 - Final appearance of the numerical model and an experimental specimen with a 0/90 arrangement

In Figure 4.29, the numerical model at collapse and a photo of the tested specimen after collapse are shown, allowing them to be compared qualitatively. Both present a very similar appearance, indicating that the boundary conditions are well implemented and provide good results.

The experimental specimen shown in Figure 4.29 is almost divided in two parts, once the experimental test proceeded beyond the failure point of the compression specimen. This event could also happen with the numerical model if the simulation continues after the failure of the specimen modelled numerically.

Chapter 5.

Conclusion

In this dissertation, a methodology was developed to create a numerical model and perform a numerical simulation of tension/compression tests in composite specimens. This methodology was developed using MatLab and Ansys softwares, with the aim to predict the behavior of the numerical model's specimens under certain loads, failure initiation and damage propagation (such as delamination and fiber failure).

A mesh convergence test was performed in order to find the best element type and size to be used in the numerical models developed in the following chapters of this dissertation. The results indicate that 8 nodes brick element, using full integration, with a size of $0.3\ mm$ was the adequate element to use, leading to a mesh with 4128 elements per ply. This is an element size capable of providing accurate results and allows its deactivation. First, it is the biggest element size that still provides accurate results (there are smaller element sizes, which provide the same results with a higher computational cost) in less time and, second, it is a small enough element, allowing the deactivation of the elements. Once a strategy using elements deactivation, in order to simulate the fiber and/or matrix failure, its size needs to be as small as possible in order to observe conveniently the damage propagation.

Delamination was simulated using cohesive and contact elements. Two different simulations of delamination using two unidirectional plies were performed, the first one with only cohesive elements and the second with delamination and contacts. This later model, delamination with contacts, was used because it was identified an interpenetration between different elements when only cohesive elements were used. The results obtained with these two simulations were very close indicating the contacts were well implemented and could be used together with cohesive elements.

The ply numerical model was implemented with cohesive and contact elements and a simulation of this ply under tension loads was performed. Results of this simulation show that the areas with the higher stress concentrations are the changes of cell, which is the zone where the spread tow with the fibers aligned at 90° crosses the spread tow with the fibers aligned at 0°. These results were as expected, since in the experimental tests the specimens with a 0°/90° arrangement tested in tension failed in the same area.

The experimental results are presented, not only for the specimens with a 0º/90º arrangement but also for the specimens with 15º/-75º, 30º/-60º and a 45º/-45º arrangements. Analyzing experimental test results it was demonstrated that plasticity under transverse compression is residual for the 0º/90º, and it is acceptable not to consider it in the numerical model, thus avoiding complexity in the convergence of the solution. It was also possible to see that the plasticity under shear loads, increase from the specimens with a 15º/-75º arrangement to the specimens with a 45º/-45º arrangement, being the specimens with a 45º/-45º arrangement the ones presenting the higher non-linearity.

With the implementation of the 26-plies compression specimen model, the program that performs the incremental-iterative analysis was improved, providing better results and a more similar behavior to the compression specimen tested experimentally.

The first numerical simulation of the 26-plies compression specimen provided a failure stress value with an error of 20.9% and the correspondent strain with an error of 15%, approximately. These errors were too high regarding the objective of this dissertation, therefore some parameters (unidirectional constants and modulus of elasticity) needed to be adjusted in order to improve the results (see section 4.3.1). It was decided to increase four parameters: the failure stress under longitudinal compression, X_C, the failure stress under transverse compression Y_C and the modulus of elasticity in both longitudinal and transversal directions.

The numerical simulation performed with the adjusted parameters provided better results than the previous one. A failure stress value of $323.8\ MPa$ and a failure strain value of 1% were obtained, which implies a displacement of $0.2\ mm$, that was the maximum displacement observed during the experimental test of the compression specimens with a 0°/90° arrangement.

Comparing the failure stress value of the 26-plies compression specimen simulation (with the adjusted parameters) with the experimental value, the error is around 2%, which is an exceptional result and compliant with the objectives set for this dissertation.

Evaluating the results, it is concluded that the proposed failure criterion is well implemented in these models. Although the maximum stress failure criterion is good enough to analyze the 0°/90° arrangement specimen, with proposed combined failure criterion the incremental-iterative analysis program is prepared to perform simulations for specimens with directions besides the principal directions.

After all this work, it can also be concluded that the simplified geometry used to create the numerical models fulfills the necessary requirements to provide accurate results, comparing to the experimental ones, and a similar final appearance.

Finally, it should be noted that the main objective of this dissertation is to replicate the specimens, with a 0º/90º arrangement, tested experimentally into a numerical model able to provide stress and strain values with an error less than 5% and presenting a similar behavior. All this dissertation was developed without knowing the mechanical properties of the material used in the experimental work, the only data used to develop the numerical models were data extracted from the experimental work. That is the reason why in this dissertation, the mechanical properties of the material needed to be adjusted in order to obtain the final results pretended.

The construction of a numerical methodology capable of, trough numerical simulations and comparison of numerical and experimental results, calculate the unknown mechanical properties of composite materials is another very important complied objective of the dissertation.

5.1.Complied objectives

In this chapter it is shown compliance with the objectives defined in section 1.2 (Chapter 1).

- Implement cohesive and contact elements, in order to simulate delamination accurately;
  - ✓ Chapter 3, from page 41 to page 47
- Develop a methodology able to model the specimens tested and simulate the experimental tests;
  - ✓ Chapter 4, from page 63 to page 67
- Perform at least one analysis of a 26-plies compression specimen and provide the stress-strain curve results of this analysis;
  - ✓ Chapter 4, from page 67 to page 71
- Validate numerical models, with an error less than 5% between numerical and experimental results;
  - ✓ Chapter 4, from page 71 to 75

5.2. Future Works

There are several aspects that can be improved to continue the work develop in this dissertation. Here are presented some important improvements that can be made in order to continue this dissertation and improve the methodology developed.

1. Improve the incremental-iterative analysis program, based on an experimental work with a fully characterized composite material;
2. Incorporation of a plasticity model, in order to describe accurately the shear plasticity;
3. Development of a simplified numerical model, in order to obtain acceptable results, with a lower computational cost.

References

[1] E. Music and A. Widroth, “Modelling of Spread Tow Carbon Fabric Composites for Advanced Lightweight Products”, Master's thesis, Chalmers University of Technology, Goteborg, Sweden, 2013.

[2] R. Jones, “Mechanics of Composite Materials”, Blacksburg, 2nd Edition, Taylor and Francis, Virginia, 1999.

[3] “2015-8-15. URL: http://composite.about.com/od/aboutcompositesplastics/l/aa060297.htm”.

[4] D. Miracle and S. Donaldson, “ASM Handbook”, 10th Edition. ASM International, The Materials Information Company, volume 21, 2001.

[5] R. A. Angélico, “Avaliação de modelos de falhas progressivas para estruturas em material compósito”, Dissertação de Mestrado, Universidade de São Paulo, 2009.

[6] R. F. Gibson, “Principles of Composite Material Mechanics”, Department of Mechnical Engineering, Way State University, McGraw-Hill, Inc, Detroit, Michigan, 1994.

[7] “2015-8-15. URL: http://materials-engineeringscience.blogspot.pt/2011/06/classes-and-characteristics-of.html”.

[8] P. Tan, L. Tong, and G. . Steven, “Modelling for predicting the mechanical properties of textile composites—A review”, Composites Part A, volume 28, no. 1997, Sidney, Australia, 1997, pp. 903–922.

[9] A. D. Kelkar, J. S. Tate and R. Bolick, “Structural integrity of aerospace textile composites under fatigue loading”, Materials Sience and Engineering B , volume 132, 2006, pp. 79–84.

[10] H. M. El-Dessouky and C. A. Lawrence, “Ultra-lightweight carbon fibre/thermoplastic composite material using spread tow technology”, Composites: Part B, volume 50, 2013, pp. 91–97.

[11] S. Sihn, R. Y. Kim, K. Kawabe, and S. W. Tsai, “Experimental studies of thin-ply laminated composites”, Composites Science and Technology, volume. 67, no. 6, 2007, pp. 996–1008.

[12] P. K. Mallick, “Fiber-reinforced composites: materials, manufacturing, and design”, Taylor and Francis, 3rd edition, 2008.

[13] A. Katunin, K. Dragan, and M. Dziendzikowski, “Damage identification in aircraft composite structures : A case study using various non-destructive testing techniques”, Composite Structures, volume 127, 2015, pp. 1–9.

[14] E. Greenhalgh and M. Hiley, “Fractography of Polymer Composites: Current Status and Future Issues”, European Conference on Composite Materials, London, 2008.

[15] “2015-8-15. URL: http://www.researchgate.net/post/What_is_the_difference_between_damage_failure_and_fracture”.

[16] R. M. Christensen, “The Thoery of Materials failure”, Oxford University Press, Oxford, 2013.

[17] P. M. Vert, “Modelización Contitutiva y Computacional Del Danõ y La Fractura de Materiales Compuestos”, Thesis Doctoral, Universitat de Girona, 2006.

[18] M. Bessa, “Meso-mechanical model of the structural integrity of advanced composite laminates”, Master's Thesis, Faculty of Engineering, University of Porto, Porto, 2010.

[19] Sun, C. T., and J. L. Tsai. "Comparison of microbuckling model and kink band model in predicting compressive strength of composites." Proceedings of the 13th International Conference on Composite Materials, Beijing, China. 2001.

[20] W. S. Slaughter. and N. A. Fleck, “Viscoelastic Microbuckling of Fiber Composites”, Journal of Applied Mechanics, volume 60, 1993, pp. 802–806.

[21] H. Koerber, J. Xavier, and P. P. Camanho, “High strain rate characterisation of unidirectional carbon-epoxy IM7-8552 in transverse compression and in-plane shear using digital image correlation”, Mechanics of Material, volume 42, no. 11, 2010, pp. 1004–1019.

[22] A. M. Moncada, A. Chattopadhyay, B. a. Bednarcyk, and S. M. Arnold, “Micromechanics-Based Progressive Failure Analysis of Composite Laminates Using Different Constituent Failure Theories”, Journal of Reinforced Plastics and Composites, volume 31, no. 21, 2012, pp. 1467–1487.

[23] I. M. Daniel, “Failure of composite materials”, Strain, volume 43, no. 1, 2007, pp. 4–12.

[24] “2015-8-15. URL: http://help.solidworks.com/2015/English/SolidWorks/cworks/r_TsaiWu_Failure_Criterion.htm”.

[25] Camanho, Pedro Ponces. "Failure criteria for fiber-reinforced polymer composites." Secção de Mecânica Aplicada, Departamento de Engenharia Mecânica e Gestão Industrial, Faculdade de Engenharia da Universidade do Porto, 2002.

[26] “2015-8-15. URL: http://www.doitpoms.ac.uk/tlplib/fibre_composites/laminate_failure.php”.

[27] C. G. Davila, N. Jaunky, and S. Goswami, “Failure Criteria for FRP Laminates in Plane Stress”, Jounal of Coposite Materials, volume 39, 2003, pp. 323-345.

[28] Z. Hashin and A. Rotem, “A cumulative damage theory of fatigue failure,” Materials Science and Engineering, volume 34, no. 2, 1978, pp. 147–160.

[29] Z. Hashin and A. Rotem, “Fatigue Failure Criterion for Fiber Reinforced Materials”, Journal of Applied Mechanics, volume 48, 1981, pp. 846–852.

[30] “2015-8-15. URL: file:///C:/Users/ASUS/Documents/Dissesta%E7%E3o/Artigos/Puck%20Criterion%20_%20Helius%20Composite%20_%20Autodesk%20Knowledge%20Network.html”.

[31] S. T. Pinho, C. G. Davilla, P. P. Camanho, L. Iannucci, and P. Robinson, “Failure Models and Criteria for FRP Under In-Plane or Three-Dimensional Stress States Including Shear Non-Linearity”, National Aeronautics and Space Administration, 2005.

[32] E. Oñate and R. Owen, “Computational Plasticity”, Computational Methods in Applied Sciences, Springer, Barcelona, 2007.

[33] Y. W. Kwon, D. H. Allen, and R. Taleja, “Multiscale Modeling and Simulation of Composite Materials and Structures”, Springer, 2008.

[34] J. Fish and Q. Yu, “Multiscale Damage Modeling for Composite Materials : Theory and Computational Framework”, International Journal for Numerical Methods in Engineering, 2001, pp. 1-38.

[35] M. Lidgett, R. Brooks, N. Warrior, K. Brown, N. Martindale, A. Wright, M. French, and A. T. Centre, “Multi-scale modeling of polymer composite materials under blast and ballistic loading”, 18th International Conference of Composite Materials, Korea, 2011, pp. 1-6.

[36] C. Zhang, “Multi-Scale Characterization and Failure Modeling of Carbon/Epoxy Triaxially Braided Composite”, PhD Thesis, Faculty of the University of Akron, 2013.

[37] Z. Xia and W. A. Curtin, “Multiscale Modeling of Tensile Failure in Fiber-Reinforced Composites”, Multiscale Modeling and Simulation of Composite Materials and Structures, 2008, pp. 37-82.

[38] L. F. Kawashita, M. I. Jones, R. S. Trask, S. R. Hallett, and M. R. Wisnom, “Static and Fatigue Delamination From Discontunuous Plies - Experimental and Numerical Investigations”, CCM International Conferences on Composite Materials, 2009.

[39] Hexcel, “HexPly 8552: Epoxy Matrix”, Hexcel Composites Publication, 2013.

[40] ANSYS Element Reference Manual, Release 13.0, 2010.

[41] “2015-8-15: URL: http://www.twi-global.com/technical-knowledge/faqs/structural-integrity-faqs/faq-what-is-reduced-integration-in-the-context-of-finite-element-analysis/”.

[42] J. B. Cardoso and P. G. Coelho, “Métodos Computacionais em Engenharia Mecânica”, Departamento de Engenharia Mecânica e Industrial, Faculdade de Ciências e Tecnologias, Universidade Nova de Lisbos, Lisboa, 2012.

[43] L. C. Bank and M. P. Bieniek, “Stress-Resultant Plasticity Theories for Composite Laminated Plates”, International Journal of Plasticity, volume 4, 1988, pp. 317 – 333.

[44] “2015-8-15. URL: http://www.matweb.com/search/datasheet.aspx?matguid=ed803744f45e42d4be2a761e41c6c17a”.

[45] Ansys, “Theory Reference for the Mechanical APDL and Mechanical Applications”, Knowledge Creation Diffusion Utilization, volume 3304, 2009, pp. 724–746.

[46] A. T. Travesa, “Simulation of delamination in composites under quasi-static and fatigue loading using cohesive zone models”, PhD thesis, Universitat de Girona, 2006.

[47] P. P. Camanho, C. G. Davila, M. F. de Moura, and M. F. De Moura, “Numerical simulation of mixed-mode progressive delamination in composite materials”, Journal of Composite Materials, volume 37, no. 16, 2003, pp. 1415–1438.

[48] M. a. Jimenez, “Application of the Finite-Element Method to Predict the Onset of Delamination Growth”, Journal of Composite Materials, volume 38, no. 15, 2004, pp. 1309–1335.

[49] Ansys, “Contact Technology Guide”, Knowledge Creation Diffusion Utilization, volume 15317, 2009, pp. 724–746.

[50] “2015-8-15. URL: http://download.autodesk.com/us/algor/userguides/mergedProjects/setting_up_the_analysis/Nonlinear/Loads_and_Constraints/Surface-to-Surface_Contact.htm”.

[51] H. Lin., “Nonlinear Analysis of Fiber-Reinforced Composite Laminates Subjected to Uniaxial Tensile Load”, Journal of Composite Materials, volume 36, no. 12, 2001, pp. 1429–1450.

[52] M. R. Maschmann, G. J. Ehlert, S. J. Park, D. Mollenhauer, B. Maruyama, a. J. Hart, and J. W. Baur, “Visualizing strain evolution and coordinated buckling within CNT arrays by in situ digital image correlation”, Advanced Functional Materials, vol. 22, no. 22, 2012, pp. 4686–4695.